MSc. Thesis

Stability of randomly placed log bed protections

Mario van den Berg

Delft University of Technology

TU Delft

Rijkswaterstaat
Ministry of Infrastructure and Water Management

Deltares
Enabling Delta Life

MSc. Thesis

Stability of randomly placed log bed protections

by

Mario van den Berg

to obtain the degree of Master of Science
at the Delft University of Technology,
to be defended publicly on Wednesday August 28, 2013 at 13:00.

Student number:	4297466	
Project duration:	September 1, 2018 – August 28, 2019	
Thesis committee:	Prof. dr. ir. W.S.J. Uijttewaal,	TU Delft, Chairman
	Dr. ir. J.D. Bricker,	TU Delft, Daily supervisor
	Dr. ir. B. Hofland,	TU Delft, Supervisor
	Dr. ir. A. Sieben,	Rijkswaterstaat
	Dr. ir. F.A. Buschman,	Deltares

This thesis is confidential and cannot be made public until August 28, 2019.

TU Delft

Rijkswaterstaat
Ministry of Infrastructure and Water Management

Deltares
Enabling Delta Life

Preface

This report is the last assignment in order to obtain the Degree of Master of Science in Hydraulic Engineering at the Delft University of Technology. This study was commissioned by Rijkswaterstaat in collaboration with Deltares under supervision of Arjan Sieben. The committee was comprised of of Wim Uijttewaal, Jeremy Bricker and Bas Hofland from Delft University of Technology Department of Hydraulic Engineering, Arjan Sieben from Rijkswaterstaat WVL and Frans Buschman from Deltares.

Research is done on the stability of log bed protections. The critical Shields parameter for rocks is derived for logs. A log filter was constructed in a flow flume and the critical shear velocities were determined. The results are compared with the theory about rock bed protections. Secondly research is done on the saturation process of logs, the settling behaviour and distribution of logs and log filter roughness.

I would like to thank the supervisors from Delft University of Technology, Wim Uijttewaal and Bas Hofland for their expertise and advice that helped me straighten my course. In addition I would like to thank Jeremy Bricker for his support and guidance at times of setbacks and obstacles. My gratitude goes out to Arjan Sieben and Frans Buschman for providing different perspectives regarding the research. This enhanced the connection between research and practice.

Also, I would like to thank the staff from the Fluid Mechanics Laboratory, Sander de Vree, Pieter van der Gaag Arno Doorn, Jaap van Duin and Frank Kalkman. Sander de Vree for his knowledge about the flumes and equipment, Pieter van der Gaag and Arno Doorn for helping setting up the experiments, Jaap van Duin for providing all the equipment and Frank Kalkman for installing and explaining software and measurements.

At last but not least I want to thank my friends and family for their continuous support. Without their support I would not have been able to finish this thesis. Thank you for cheering me up during hard times, providing new insights and laughter all year round.
I can close this chapter of my life and open another. Thank you all.

Mario van den Berg
The Hague, August 2019

Abstract

Design criteria for the stability of rock bed protections (rock filters) are extensively researched and successfully applied in practice. The most common stability criteria are the Izbash and Shields criteria. These methods define a critical flow (Izbash) or parameter (Shields). Rijkswaterstaat (RWS) wants to explore a more sustainable bed protection by using logs instead of rock. A pilot project is started where logs will be used as bed protection. It is yet unclear if the design and construction approaches for rock bed protections can be used for log bed protections. The most dominant aspect is that logs are cylindrical objects, while rocks are spherical. This means that the design criteria for rock filters are not directly applicable to log filters. This research aims to verify if the Shields criteria for rock can be used for logs to create functional and safe designs.

To achieve this, two experiments are performed at the TU Delft faculty of Civil Engineering & Geosciences. The first experiment explores the settling behaviour of logs for multiple drop methods. Insight is gained in the settling velocities, distribution and the Magnus effect (force exerted on a rotating object, e.g. the curve of a football spinning through the air) of logs settling in a water column. Results from these experiments are used in the second experiment. This experiment is done in a 14.3 m long flow flume where a log filter is constructed using the drop method that was preferred from the first experiment. The roughness, stability and porous flow of a log filter are investigated. The results are compared with what is known for rock filters.

Willow twigs were used as model logs. This was done to be able to correctly scale the results to full scale. Primary reason for using twigs was the effect of bark on the roughness of a cylinder. This is difficult to replicate on model scale. Saturating the model logs however was more time consuming than initially expected. Attempts were made to accelerate the process but these were futile. One method, using a diaphragm vacuum pump, could not be applied due to lack of resources.

From the first experiment it was concluded that large quantities of logs can be used to create functional log filters. This is a positive result as this will reduce construction time in practice. The method used was a funnel. This method was applied in the flume to construct the log filters. By measuring the velocity profile for multiple discharges the roughness of a log filter was measured. This also resulted in an equation of the shear velocity as a function of the discharge. By increasing the discharge step by step and determining the corresponding shear velocities, several mobility phases of a log filter were found. Higher critical Shields parameters were observed than for rock of the same dimensionless diameter. This means that the Shields design criteria for rock can be applied in practice for log filters with similar properties as the log filters in this research.

Contents

List of Figures

List of Tables

Nomenclature

Dimensionless symbols

Symbol	Description	Dimensions	Units
Δ	Specific gravity	$\frac{\rho_s - \rho_w}{\rho_w}$	-
γ	Dimensionless shape factor	-	-
κ	Von Kárman constant	-	0.41
ξ	Shape factor	-	-
C	Dimensionless coefficient	-	-
C_D, C_S, C_L	Coefficient of proportionality	-	-
f	Friction coefficient	-	-
Fr	Froude number	$\frac{\overline{u}}{\sqrt{gd}}$	-
I	River bed gradient	L/L	-
K	Volumetric form factor		-
k_1-k_5	Dimensionless parameters	-	-
m'	Discharge coefficient	-	-
n_i	Scale ratio	-	-
r_{pcc}	Pearson Coefficient of Correlation	-	-
Re	Reynolds number	$\frac{\overline{u}h}{\nu}$	-
Re_*	Particle Reynolds number	$\frac{u_* d}{\nu}$	-
Re_s	Settling Reynolds number	$\frac{w_s d}{\nu}$	-

Greek symbols

Symbol	Description	Dimensions	Units
α	Angle of attack	Radian	Rad
δ_v	Height viscous sublayer	L	m
μ	Kinematic viscosity	L^2/T	10^{-6} m^2/s
ν	Dynamic viscosity	L^2/T	10^{-6} m^2/s
ω	Angular velocity	1/s	rad/s
ρ_{log}	Log density	M/L^3	kg/m^3
ρ_s	Solid density	M/L^3	kg/m^3
ρ_w	Water density	M/L^3	1000 kg/m^3
σ	Standard deviation	-	%

σ_{filter}	Standard deviation of the log filter height	L or -	m or %
τ_b	Bottom shear stress	$M/(LT)^2$	Pa
τ_c	Critical shear stress	$M/(LT)^2$	Pa
τ_z	Shear stress in the water column	$M/(LT)^2$	Pa
θ	Angle	Radian	Rad

Roman symbols

Symbol	Description	Dimensions	Units
$\overline{U}$	Depth averaged flow velocity	L/T	m/s
c_1, c_2	Fitted intersection	L	m
c_1, c_2	Fitted slope	L/L	-
A_D, A_S, A_L	Drag, Shear and Lift (exposed) surface area	M^2	m^2
A_p	Presented area	L^2	m^2
b	Disc thickness	L	m
$B_{Rehbock}$	Rehbock weir width	L	m
D	Container diameter	L	m
d	(Log) Diameter	L	m
d_{50}, d_{n50}	Mean and nominal mean diameter	L	m
d_a	Area-equivalent diameter	L^3	m^3
F_D, F_S, F_L, F_F	Drag, Shear, Lift and Friction force	$(ML)/T^2$	N
F_M	Magnus force	$(ML)/T^2$	N
G	Vortex strength	L^2Radian/T	m^2rad/s
g	Gravitational acceleration	L/T	9.81 m/s
h	Water depth	L	m
h_{drop}	Drop height	L	m
h_e	Effective height	L	m
h_{filter}	Filter height	L	m
h_k	Water level at two times the weir height, upstream	L	m
h_{laser}	Laser height	L	m
h_w	Weir height	L	m
k	Turbulent kinetic energy	L^2/T^2	m^2/s^2
k_r	Nikuradse roughness coefficient	L	m
L	Log length	L	m
m	Mass	M	kg
m_{nail}	Mass nail	M	kg

Q	Discharge	L^3/T	m^3/s
$q_{Rehbock}$	Specific Rehbock weir discharge	L^2/T	m^2/s
r	Radius of elementary ring	L	m
r_0	Radius	L	m
r_u, r_v, r_w	Relative turbulent kinetic energy in x-, y- and z-direction, respectively		
s	Revolution speed	1/T	revolutions/s
U	Velocity	L/T	m/s
$u_{*,c}$	Critical shear velocity	L/T	m/s
u_*	Shear velocity	L/T	m/s
u, v, w	Flow velocity in x-, y- and z-direction, respectively	L/T	m/s
V	Voltage	-	V
V	Volume	L^3	m^3
W	Weight	$(ML)/T^2$	N
w_{ns}	Settling velocity of non spherical particle	L/T	m/s
$w_{s,\infty}$	Settling velocity in unconfined fluid	L/T	m/s
w_s	Settling velocity	L/T	m/s
z_0	Zero velocity level	L	m
z_{laser}	Laser distance	L	m

1

Introduction

1.1. Background information

In 2000 an EU directive (legal act), known as *Water Framework Directive 2000* (Dutch: Kaderrichtlijn Water, KRW), was enacted. This act requires all EU members to increase the water quality (chemically and ecologically) of all water bodies. The means to achieve this are not specified in the directive. In The Netherlands, Rijkswaterstaat (RWS) is responsible for the execution of KRW related measures. Three tranches are defined. The first tranche is executed from 2010-2015, the second tranche from 2016-2021 and the third tranche from 2022-2027 (Rijkswaterstaat, 2016). Each tranche contains measures that can be of three types: arrangement, management and research. Arrangement measures are for example digging secondary channels and creating fish passages (Dutch: vis ladders). Management focuses on service and maintenance of water bodies and measures. Research is sometimes required to find effective and feasible solutions. This thesis is part of the second tranche. One of the measures of the second tranche is increasing the ecological water quality of water bodies *Haringvliet* and *Hollands Diep*. Pilots with submerged logs performed in the *Nederrijn-Lek* show an increase in biodiversity (Sieben, 2016). Outside of The Netherlands this effect of wood has also been researched and confirmed. In the United States, Australia and Europe the importance and effects of wood in rivers is extensively researched (van den Berg, 2018). Moreover structures known as Engineered Log Jams and Deflector Jams are used to train river beds and embankments.

Over the past decades, inland ships have grown in capacity. These larger ships require deeper and wider navigation channels. To accommodate for this Dutch rivers have been dredged. At some locations a peat layer was penetrated causing the erosion of the underlying sand layer. The erosion process creates scour holes. These scour holes are clearly visible in the *Oude Maas*. Figure 1.1 shows a section of the Oude Maas with bed levels up to -18m NAP, indicating the presence of scour holes. All sections are shown in appendix A. These scour holes can become a threat to the stability of river embankments if they continue to grow.

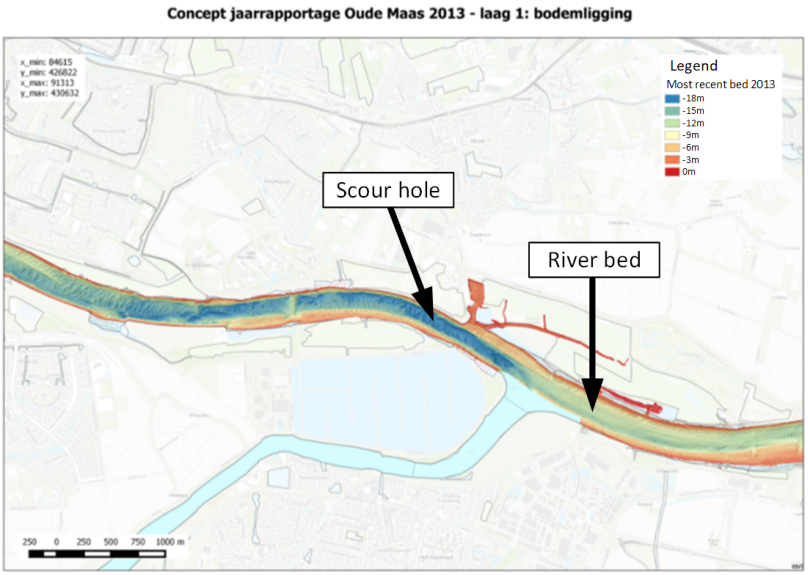

Figure 1.1: Section of the Oude Maas 2013, courtesy of Arjan Sieben RWS-WVL

The increase of residences living in flood risk areas over the past decades requires stricter safety standards for the Dutch river systems. This has lead to an increase in the normative river discharges (Ruimte voor de Rivier, 2018). The increased discharges relate to higher maximum water levels in rivers. Therefor flood protection structures, like dikes, have to be re-evaluated. In the past this is generally done by increasing the height or width of dike or dike section. However a more sustainable approach is in development. In 2007 the *Room for the River* (Dutch: Ruimte voor de Rivier) project was started in The Netherlands. This project aims to increase the space (room) for rivers while generating recreation opportunities for the local communities and increasing biodiversity of the river. Multiple measurements can be taken to create space for rivers, shown in appendix B. This project generates a lot of cut down trees. These trees can be used for the KRW goals to increase the ecological quality of Dutch water bodies, like *Haringvliet* and *Hollands Diep*. RWS also wants to explore a secondary goal for these logs: a log bed protection as an alternative for rock bed protections. A log bed protection would be ecologically friendly and sustainable.

1.2. Rijkswaterstaat pilot

RWS wants to start a pilot to investigate if log bed protections are feasible. A schematisation of how a scour hole would be protected using logs is shown in figure 1.2. The location of this pilot is the Oude Maas.

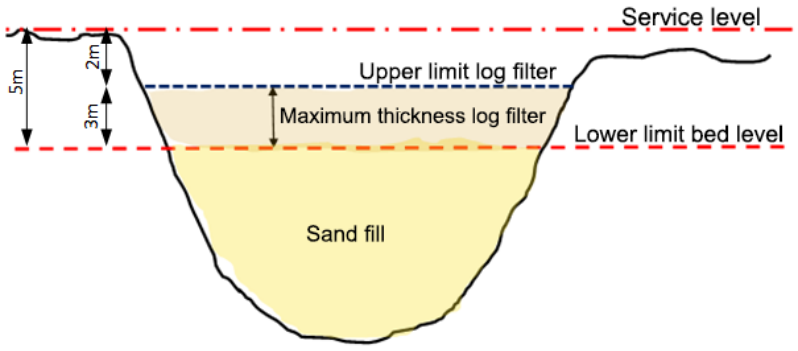

Figure 1.2: Schematisation of filled scour hole with log bed protection

There are steps to take in order to obtain the knowledge required to design a log bed protection. Important aspects regarding a design are listed below. Some of these aspects have already been researched. These are the thickness of the bed protection (Bouman, 2018) and the orientation of the logs (Beulink, 2018). This thesis

will focus on the stability of a log filter. Mainly qualitative research is done on the construction method and the effect of backfilling. The porosity, permeability and effect of bundling is not researched.

- The thickness of the bed protection
- The orientation of the logs with respect to the flow
- The construction method for placing the logs
- The porosity/permeability of a log filter
- The stability of a log filter
- The effect of bundling logs
- The effect of backfilling a log filter with sand

Ideally a cycle *From tree to bed* is created, where logs from cut down trees are first transported to a saturation zone, usually an embankment. At this location the logs are left to saturate and increase local biodiversity. When they are fully saturated they are replaced with fresh logs and transported to a different location where they are used as bed protection. Embankments are periodically inspected and if needed vegetation is removed (embankment management). This can be a source of fresh logs for the long term. On short term the *Room for the River* project can supply a large quantity of the required logs for the pilot.

1.3. Problem description

The stability of a rock bed protection is determined using the Izbash and Shields stability criteria (see section 2.3). It is not yet known how well the Izbash and Shields stability criteria are applicable to log bed protections. It is safe to assume that they are not directly applicable because rock and logs do not have similar dimensions (spherical versus cylindrical). More research on this application is therefor desired.

Secondly research done on the erosion process showed that a log bed protection can be used to stabilise scour holes and reduce the erosion volume (Beulink, 2018). However this research relied on precise placement of the logs in order to obtain consistent measurements. In practice, construction of a log bed protection relies on dumping of the logs. This introduces randomness to how the logs are oriented on the river bed. The magnitude and impact of these random orientations has not yet been researched. Research is therefor necessary on the settling behaviour of logs as well.

Thirdly, the stability of logs submerged in water depends on the density of the log. For stones the density is constant in time. For logs a constant density is not guaranteed due to organic processes of wood (e.g. decay). It is unknown what densities are achievable and how long logs have to be saturated. Research regarding the saturation process is crucial to the feasibility of a log bed protection.

1.4. Research objective

This thesis aims to quantify the stability of log bed protections as well as find a suitable construction method. Two scaled experiments are done at TU Delft, Faculty of Civil Engineering and Geosciences. The first experiment makes a qualitative analysis of the settling behaviour of logs. Results of these experiments are used in the second experiment. The second experiment analysis the stability of log bed protections constructed using the method preferred from the first experiment. The results of the second experiment are analysed and compared with the Izbash and Shields stability criteria for rock bed protections. The main research question to be answered is:

How well are stability criteria for rock bed protections applicable to log bed protections?

To answer this question the following subquestions are asked.

1. How do logs settle on a flat bed?
2. What is the roughness of a log bed protection?
3. How do log bed protections behave?

The first question is answered in the first experiment. The second question is related to the stability of the log bed protection. The roughness of a log bed protection can have a significant influence on the stability. The last question is answered by observing how a log protection behaves during the second experiment. The density of the logs is monitored throughout the course of this thesis to gain insight in the saturation process.

2

Theoretical background

A lot of knowledge on river flows and rock bed protections already exists. In this chapter the theory associated with the research objective is explained. First previous research by students from Delft University of Technology is briefly discussed in section 2.1. Section 2.2 discusses the hydraulic loads of a turbulent open channel flow on a river bed. The stability of a rock bed protection is discussed in section 2.3. The theory on the stability of a rock bed protection is modified for logs in section 2.4. Before dumped logs reach the river bed they settle through the water column. Important aspects are the settling velocity and Magnus effect, discussed in sections 2.5 and 2.6, respectively.

2.1. Previous research

Some aspects for the RWS pilot project are already investigated by students of Delft University of Technology. Two groups of graduate Bachelor students at the faculty of Civil Engineering and Geosciences (CEG) performed flume experiments to analyse the hydro-mechanical material properties of logs. A summary of their research can be found in appendix C. Two graduate Master students, also from the CEG faculty, investigated the effect of a log or log filter on the erosion of a sand bed. Their research is summarised in appendix D.

The studies concluded that a log bed protection is effective against erosion of the bed but no conclusive stability criteria were developed. Stability criteria for rock can be used for logs when adjusted for log dimensions. However the research by the Bachelor students only tested small structures of logs that did not represent a log bed protection. Their results are therefor not applicable to the pilot project. Research by the Master graduates concluded that the filter function of a log bed protection can already be achieved with a thickness of just three log diameters. The hydraulic load on the bed underneath the filter is reduced to only a gradient flow. This gradient flow is a porous flow in the river bed as a results of the bed gradient. This porous flow does not cause erosion of the bed.

2.2. Flow characteristics

The flow condition of a river is best described by two parameters, the Froude and Reynolds number. The Froude number (Fr) is the ratio of kinetic energy to gravitational energy and defined as:

$$Fr = \frac{\overline{U}}{\sqrt{gh}} \tag{2.1}$$

- $\overline{U}$ [m/s] Depth averaged flow velocity
- g [9.81 m/s^2] Gravitational acceleration
- h [m] Water depth

Froude numbers smaller than 1.0 indicate that the gravitational energy is larger than the kinetic energy. This is known as sub critical flow and is the case for Dutch rivers (Fr«1.0).

The Reynolds number (Re) is the ratio of flow inertia to viscosity and defined as:

$$Re = \frac{\overline{U}h}{\nu} \tag{2.2}$$

Where ν is the kinematic viscosity of the fluid. Flows with a Reynolds number smaller than 10^2 are considered laminar, larger than 10^3 are considered turbulent and in between are transitional. With a kinematic viscosity of 10^{-6} m^2/s for water Reynolds numbers in Dutch rivers are of the order 10^5. Dutch rivers are thus best described as turbulent sub critical (open channel) flows.

2.2.1. Turbulence

Turbulence can be defined as the chaotic motion of a fluid. Although chaotic, turbulent flows have distinct probabilistic properties. When averaged over time, turbulence is the fluctuation from the mean. A typical time series of, for example a flow velocity component, is shown in 2.1a. The corresponding probability density function is shown in figure 2.1b. The probability density function follows a guassian (normal) distribution.

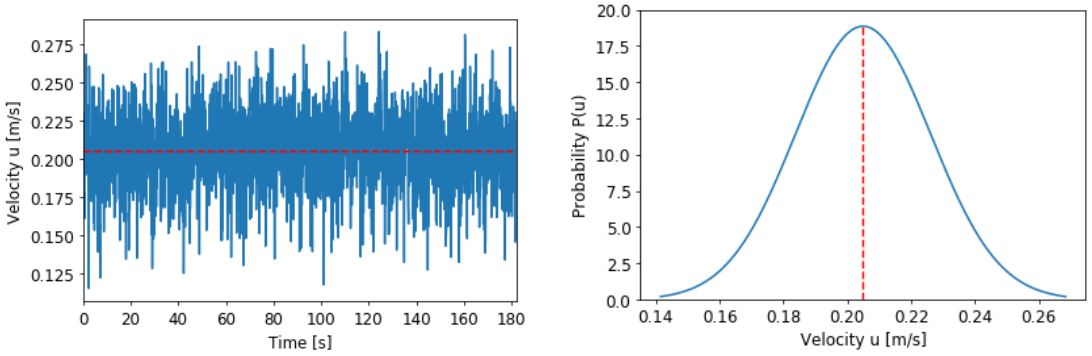

(a) Time series

(b) Probability density function

Figure 2.1: Example of a turbulent flow (a) Time series of flow velocity component u (b) Probability density function of velocity u. The mean is shown as the red striped line.

The turbulence properties of a flow can be analysed by splitting the time series in a mean and turbulent part. This can be done through Reynolds decomposition. The velocity components can be rewritten as:

$$u = \overline{u} + u' \qquad v = \overline{u} + v' \qquad w = \overline{w} + w' \tag{2.3}$$

- u, v, w Flow velocity in respectively x-, y- and z-direction
- $\overline{u}$, $\overline{v}$, $\overline{w}$ Time averaged (mean) flow velocity
- u', v', w' Flow velocity fluctuation (turbulence)

The turbulent kinetic energy (k) of the flow can be described as Schiereck (2016):

$$k = \frac{1}{2}\left(\overline{u'^2} + \overline{v'^2} + \overline{w'^2}\right), \quad r_u = \frac{\sqrt{\overline{u'^2}}}{\overline{u}}, r_v = \frac{\sqrt{\overline{v'^2}}}{\overline{v}}, r_w = \frac{\sqrt{\overline{w'^2}}}{\overline{w}} \tag{2.4}$$

Where r_u, r_v and r_w is the relative fluctuation intensity of u, v and w, respectively.

2.2.2. Shear stress

Generally rivers are simplified as open channels of constant width and depth. The flow in an open channel can be described as a steady uniform turbulent flow. The shear stress over the height (τ_z) for this type of flow is defined by van Rijn (1993) as:

$$\tau_z = \underbrace{\rho_w \nu \frac{du}{dz}}_{\text{viscous}} - \underbrace{\rho_w \overline{u'w'}}_{\text{turbulent}} \tag{2.5}$$

- ρ_w [1000 kg/m^3] Density of water
- du/dz [1/s] Time averaged velocity gradient
- $\overline{u'w'}$ [m^2/s^2] Time averaged velocity fluctuation

The turbulent part is dominant over most of the height, see figure 2.2a. When the bed is considered smooth the viscous part is dominant near the bed, this layer is called the viscous sublayer (δ_v). Above the viscous sublayer the flow is turbulent, see figure 2.2b. When the bed is considered rough the viscous part is equal to zero.

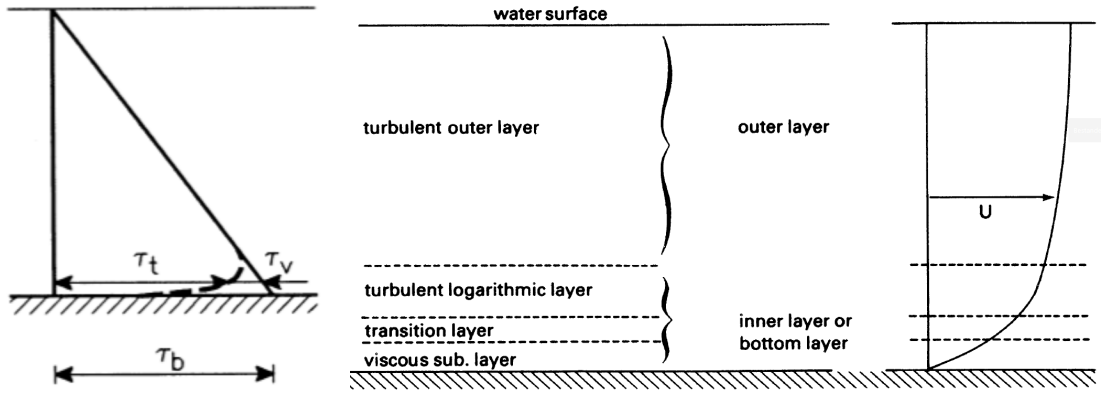

(a) Shear stress distribution over the height

(b) Sublayers of a turbulent flow

Figure 2.2: (a) Shear stress distribution over the height (b) Sublayers of a turbulent flow (van Rijn, 1993)

2.2.3. Wall flow

The type of flow described above is also known as wall flow. Wall flow is a term used to describe the flow of a fluid along a solid boundary. In the case of rivers this wall is the river bed. Depending on the roughness of the bed the velocity profile can be determined. To determine if the bed is smooth, rough or transitional the Nikuradse roughness coefficient (k_r) and shear velocity (u_*) are introduced. The shear velocity is defined as:

$$u_* = \sqrt{\tau_b/\rho_w} = \sqrt{ghI} \tag{2.6}$$

- τ_b [Pa] Bottom shear stress
- I [-] Bed/surface level gradient (for a steady uniform flow)

Note that this parameter is not actually a velocity but only has similar dimensions [m/s]. The shear velocity actually expresses a shear stress. The Nikuradse roughness coefficient (k_r) for rock bed protections is typically one or two rock nominal diameters (d_{n50}). Three regimes are classified (van Rijn, 1993):

- Smooth $(u_* k_r)/\nu \leq 5$
- Rough $(u_* k_r)/\nu \geq 70$
- Transitional $5 \leq (u_* k_r)/\nu \leq 70$

Where ν/u_* is a length scale for the viscous sublayer (δ_ν). These equations thus describe the ratio of the roughness elements to the thickness of the viscous sublayer. For a rough bed the velocity profile is described by *The law of the wall*, equation 2.7 (van Rijn, 1993).

$$u = \frac{u_*}{\kappa} \ln\left(\frac{z}{z_0}\right) \tag{2.7}$$

- z_0 [m] Zero velocity level
- κ [0.41] Von Kárman constant

The zero velocity level (z_0) parameter has no physical meaning, because this equation is not valid very close to the bed (van Rijn, 1993). The parameter is solely used as a computation parameter. Studies showed that for rock z_0=k_r/30 is a good estimate. For a bed consisting of logs k_r is unknown, and so is z_0. The hydraulic plane (z=0) is usually set to the (river) bed.

2.3. Stability criteria for rock

The most frequently used stability criteria for stone bed protections are developed by Izbash and Shields. The fundamental difference between the two methods is that Izbash focuses on the forces acting on a single grain, while Shields looks at the friction of a fluid acting on the bed (over an area much larger than one grain). The following paragraphs briefly discuss the two methods.

2.3.1. Izbash

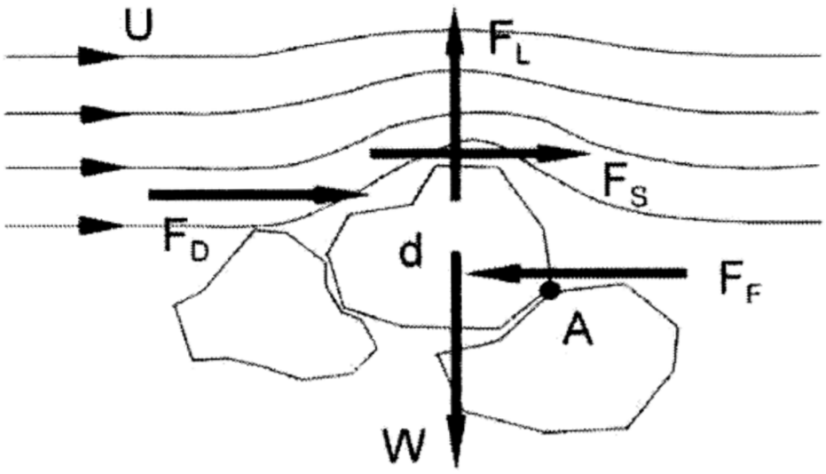

Figure 2.3: Forces on a single grain described by Izbash (Schiereck, 2016)

The stability of a single grain can be seen as a balance of forces, see figure 2.3. When the forces are in equilibrium the grain is stable. When the equilibrium is disturbed the grain starts to move. For a single grain the balance force is relatively easy to determine. Assuming the grains are spherical the forces can be expressed as follows (Schiereck, 2016):

$$\left.\begin{aligned} \text{Drag force: } F_D &= \frac{1}{2} C_D \rho_w u^2 A_D \\ \text{Shear force: } F_S &= \frac{1}{2} C_S \rho_w u^2 A_S \\ \text{Lift force: } F_L &= \frac{1}{2} C_L \rho_w u^2 A_L \end{aligned}\right\} \qquad F \propto \rho_w u^2 d^2 \tag{2.8}$$

- C_D, C_S, C_L [-] Coefficients of proportionality
- A_D, A_S, A_L [m^2] Exposed surface area

The surface area of a grain when schematised as a sphere is a circle and is proportional to the square of a representative diameter (d). The 2-dimensional force balance requires that the sum of forces in horizontal (ΣH), vertical (ΣV) and moment (ΣM) equals zero.

$$\left.\begin{array}{ll} \Sigma H = 0: & F_D + F_S = f \cdot W = F_F \\ \Sigma V = 0: & F_L = W \\ \Sigma M = 0: & (F_D + F_S) \cdot \mathcal{O}(d) = W \cdot \mathcal{O}(d) \end{array}\right\} \qquad \rho_w u_c^2 d^2 \propto (\rho_s - \rho_w) g d^3 \tag{2.9}$$

- F_F [N] Friction force
- W [N] Submerged weight
- f [-] Friction coefficient

The velocity (u) is now the critical velocity (u_c) because this is a stability parameter. The stability parameter is the relation between load and strength:

$$u_c^2 \propto \left(\frac{\rho_s - \rho_s}{\rho_s}\right) g d = \Delta g d \qquad \rightarrow \qquad u_c^2 = C \Delta g d \tag{2.10}$$

- ρ_s [kg/m^3] Density of the solid (rock)
- Δ [-] Relative density

Parameter C is a dimensionless parameter determined from experiments. The experiments by Izbash resulted in equation 2.10:

$$u_c = 1.2\sqrt{2 \Delta g d} \tag{2.11}$$

Izbash did not specify the location of the velocity to be used in the equations, neither did he specify which diameter. Following his experiment it is accepted that the nominal diameter (d_n) can be used. For the velocity it is accepted to calculate/measure the velocity that is present close to the bed.

2.3.2. Shields

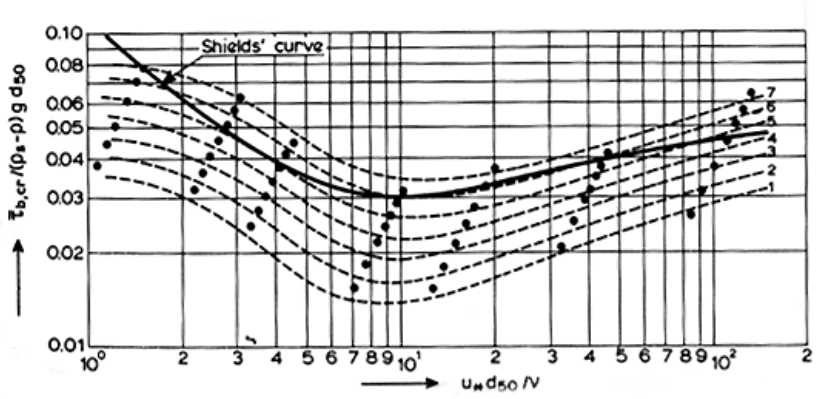

Figure 2.4: Mobility levels including the critical Shields parameter curve (van Rijn, 1993)

Another stability criteria is developed by Shields. Again a stability parameter is defined as the relation between load and strength. However Shields used the critical shear stress (τ_c) as active force, resulting in a similar equation as Izbash (equation 2.12), but using the shear velocity instead of velocity. This parameter is known as the critical Shields parameter (ψ_c).

$$\psi_c = \frac{\text{load}}{\text{strength}} = \frac{\tau_c d^2}{(\rho_s - \rho_w) g d^3} = \frac{\tau_c}{(\rho_s - \rho_w) g d} = \frac{u_{*,c}^2}{\Delta g d} = f(Re_*) \tag{2.12}$$

$$Re_* = \left(\frac{u_{*,c}d}{\nu}\right) \tag{2.13}$$

When the shear velocity is used instead of the critical shear velocity the equation becomes a mobility parameter (ψ). The particle Reynolds number (Re_*) describes if the grain remains in the viscous sublayer or protrudes into the turbulent layer. Multiple transport levels can be distinguished, see figure 2.4, based on research done by Kramer and Delft Hydraulics. The multiple levels indicate the magnitude of sediment transport and are given below.

1. Occasional particle movement at some locations
2. Frequent particle movement at some locations
3. Frequent particle movement at many locations
4. Frequent particle movement at nearly all locations
5. Frequent particle movement at all locations
6. Permanent particle movement at all locations
7. General transport (initiation of ripples)

From the figure it is clear that the Shield's curve corresponds with levels 5 and 6, frequent and permanent particle movement at all locations. Note that both sides of equation 2.12 use the critical shear velocity ($u_{*,c}$). Because of this every diameter corresponds with a certain $u_{*,c}$. To show this, Van Rijn replaced the particle Reynolds numbers with the dimensionless particle diameter (d_*, equation 2.14). The dimensionless particle diameter can be seen as the ratio of submerged weight (Δg) to viscous forces (ν). When a rock bed protection is designed for rivers ψ_c=0.03 is used.

$$d_* = d_{50}\left(\frac{\Delta g}{\nu^2}\right)^{1/3} \tag{2.14}$$

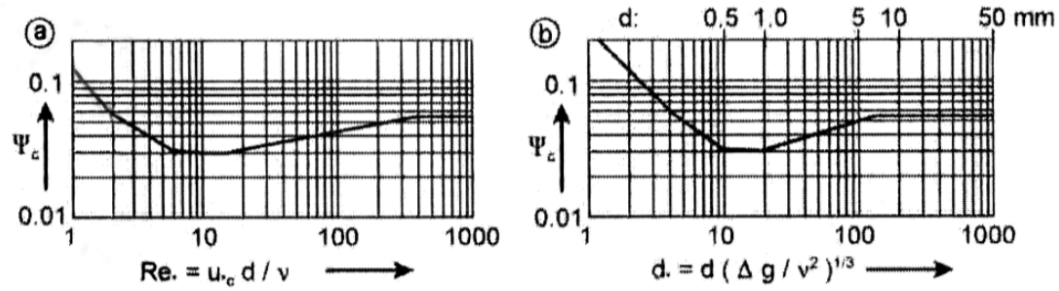

Figure 2.5: Shields parameter as a function of Re_* and d_* (Schiereck, 2016)

2.4. Izbash & Shields formula for logs

The stability of a log bed protection is different from a stone bed protection. This is mainly due to the different dimensions of the elements. Current stability criteria for stones rely on the fact that small rocks can be schematised as spheres with a specified diameter. Logs however are cylindrical and can therefor not be expressed by a single parameter. A log with a similar diameter, but different length can behave differently under hydraulic load. In this section the Izbash and Shields formula are modified for logs.

2.4.1. Izbash for logs

Çete and Haage (2016) applied the Izbash method to logs. First deriving the formula for flow parallel and perpendicular to the length of the log, figure 2.6 and equations 2.15 and 2.16.

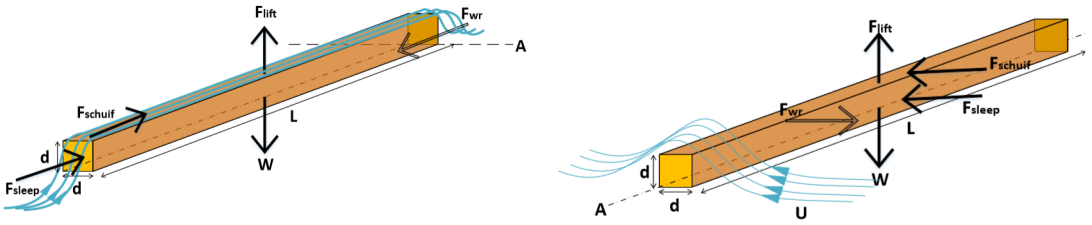

(a) Flow parallel to the log

(b) Flow perpendicular to the log

Figure 2.6: Schematisation of flow parallel and perpendicular to logs (Çete and Haage, 2016)

$$u^2_{c,parallel} = \Delta g d \left(\frac{L^2}{k_1 d^2 + k_2 d L + k_3 L^2} \right) \tag{2.15}$$

$$u^2_{c,perpendicular} = \Delta g d \left(\frac{L}{k_4 L + k_5 d} \right) \tag{2.16}$$

- L [m] Log length
- d [m] Log diameter
- $k_1 - k_5$ [-] Dimensionless parameters

Accounting for arbitrary angles ($\alpha \neq 0° \wedge 90°$) the formulas can be combined into equation 2.17. For derivations see (Çete and Haage, 2016).

$$u^2_c = \Delta g d \left(\frac{L^2}{k_1 d^2 + k_2 d L + k_3 L^2} + \frac{L}{k_4 L + k_5 d} \right) \tag{2.17}$$

The equation for flow parallel to the log was simplified by assuming that the influence of coefficients k_1 and k_2 were negligible with respect to k_3, because in general $L^2 >> d^2$ and $L^2 > dL$. This assumption reduced equation 2.15 to equation 2.18. This is similar to the general Izbash equation (equation 2.10) allowing for direct comparison with the Izbash formula for rock.

$$u^2_c = \frac{\Delta g d L^2}{k_3 L^2} = \frac{\Delta g d}{k_3} = 2C^2 \Delta g d \quad \text{with} \quad \frac{1}{k_3} = 2C^2 \tag{2.18}$$

van Leeuwen, P. et al. (2016) found that this assumption was incorrect. The order of the coefficients $k_1 d^2$, $k_2 dL$ and $k_3 L^2$ were 10^{-3}, 10^{-2} and 10^{-4} respectively. Parameter $k_3 L^2$ was an order of 10 to 100 smaller. The results from Çete and Haage (2016) are therefor not representative of the actual value of C. If we only take $k_2 dL$ into account and neglect $k_1 d^2$ and $k_3 L^2$, the log length to diameter ratio is introduced, equation 2.19.

$$u^2_c = \frac{\Delta g d L^2}{k_2 dL} = \frac{\Delta g dL}{k_2 d} = 2C^2 \Delta g d \quad \text{with} \quad \frac{L}{d} \frac{1}{k_2} = 2C^2 \tag{2.19}$$

2.4.2. Shields for logs

Çete and Haage (2016) also applied the Shields method to logs. The load is defined by the exposed surface area of the log to the flow. The strength is defined as the submerged weight of the log. This is done for a single log, parallel to the flow, in equation 2.20.

$$\psi_c = \frac{\tau_c dL}{(\rho_s - \rho_w) g d^2 L} = \frac{u^2_{*,c}}{\Delta g d} = f(Re_*) \tag{2.20}$$

The left side of the equation is identical to the Shields equation for rock. The right side ($f(Re_*)$) appears to also be identical, see equation 2.21 (Çete and Haage, 2016).

$$\frac{\text{inertia}}{\text{viscosity}} \sim \frac{\rho U^2 / L}{\mu U / dL} = \frac{Ud}{\nu} = f(Re_*)$$

$$f(Re_*) = \frac{u_{*,c} d}{\nu} \tag{2.21}$$

For a log perpendicular to the flow equation 2.20 is identical, while for $f(Re_*)$ the inertia and viscosity are now proportional to the log diameter instead of the log length.

$$\frac{\text{inertia}}{\text{viscosity}} \sim \frac{\rho U^2/d}{\mu U/d^2} = \frac{Ud}{\nu} = f(Re_*)$$

$$f(Re_*) = \frac{u_{*,c}d}{\nu} \tag{2.22}$$

2.4.3. Applicability of modified equations

The derivation for Izbash shows that for logs this stability criteria is proportional to rock with a factor of L/d. The derivation for Shields shows that for logs this stability criteria is identical to rock. Both equations remain quite simple, allowing for easy implementation in the model and in practice. The Izbash method only requires an adjustment using a dimensionless factor. This factor is easily determined. The Shields method is identical and requires no additional computation.

Though the Shields method appears to be the better option, one should keep in mind that L/d could have a significant influence on stability. If the ratio is close to 1 the logs are similar to spheres, but for very small and very large ratios logs are discs or rods. The effect of L/d is unknown and researched in this thesis and focus will be on the Shields parameter.

2.5. Settling velocity

Settling is the process of a particle sinking in a medium. In hydraulic engineering the term is mostly used for (very) small particles (clay and sand) sinking in water. The settling velocity is the terminal velocity at which a particle sinks. This velocity has extensively been researched for single particles. For a cloud of particles the settling velocity for each individual particle is reduced. This is known as hindered settling.

Three methods for determining the terminal settling velocity (i.e. the maximum possible vertical fall velocity) can be distinguished: Stokes', Grace's and Newton's methods. The methods can be applied to a laminar, transitional and turbulent flow regime respectively. These methods are based on spherical particles, like sand, and not for cylindrical particles, like logs. In this section only the methods for cylindrical particles are discussed. For all the derivations see appendix E.

2.5.1. Cylindrical particles

Logs are non-spherical particles. They are best described as (right circular) cylinders. The equations for spherical particles are modified to account for the different shape. Stokes' and Newton's settling velocity for spherical particles (w_s) can be rewritten using cylinder dimensions, see equations 2.23 and 2.24 (derivations in appendix E).

$$w_s = \frac{\pi(\rho_s - \rho_w)gd^2}{48\mu} \qquad \textit{Stokes} \tag{2.23}$$

$$w_s = 1.428\sqrt{\Delta g d} \qquad \textit{Newton} \tag{2.24}$$

These two equations are proportional to the equation for spheres. Stokes' settling velocity is proportional with a factor $48/(18\pi)$=0.849. Newton's settling velocity is proportional with a factor 1.428/1.73=0.825.

It was not possible to rewrite Grace's method for cylinders. A correction can be made by introducing a shape factor parameter $\xi = w_{ns}/w_s$, where w_{ns} is the settling velocity of a non-spherical particle. This parameter is a function of the volumetric form factor (K) and d^* (equation 2.14), see equation 2.29. The volumetric form factor is the ratio of the volume (V) of a particle and an 'area-equivalent diameter', d_a (i.e. the diameter of the sphere with the same projected area (Wilson et al., 2006)). The value of K is 0.524 for spheres and 0.260 for sand. For cylinders the value depends on the L/d ratio and orientation. Saucier (2000) developed a dimensionless shape factor (γ). This dimensionless parameter can be used to determine the volumetric form factor.

$$K = \frac{V}{d_a^3} = \frac{V}{\left(\sqrt{4A_p/\pi}\right)^3} \tag{2.25}$$

Saucier (2000) started with defining the presented area (A_p) as:

$$A_p = \gamma \left(\frac{m}{\rho_s} \right)^{2/3} = \gamma V^{2/3} \tag{2.26}$$

- γ [-] Dimensionless shape factor
- m [kg] Mass

For any right circular cylinder the presented area can be defined using the dimensions of the cylinder and an orientation, see figure 2.7. For any orientation the presented area and volume are given by:

$$A_p = Ld\cos\left(\theta - \frac{\pi}{2}\right) + \frac{\pi}{4}d^2|\cos(\theta)| = d^2\left(\frac{L}{d}\sin(\theta) + \frac{\pi}{4}|\cos(\theta)|\right) \qquad \frac{m}{\rho_s} = V = \frac{\pi}{4}d^2L \tag{2.27}$$

Where θ is the angle in radians.

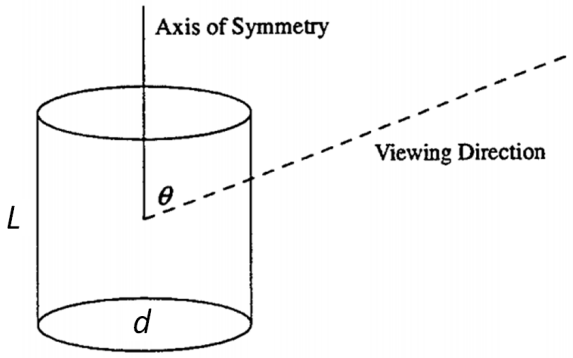

Figure 2.7: Cylinder dimensions and orientation (Saucier, 2000)

Combining equations 2.26 and 2.27 and solving for γ:

$$\gamma(\theta) = a\sin(\theta) + b|\cos(\theta)| \qquad a = \left(\frac{\pi}{4}\frac{L}{d}\right)^{-2/3}\frac{L}{d} \qquad b = \left(\frac{\pi}{4}\frac{L}{d}\right)^{-2/3}\frac{\pi}{4} \tag{2.28}$$

When L/d and θ are known and γ is solved, A_p can be determined using equation 2.26 and K using equation 2.25. If the L/d ratio equals 1.0 and θ=$\pi/2$, the value of K is close to that of spheres (0.547). If θ=0 the value of K is larger ($\pi/4 \approx 0.785$).

The L/d ratio for the logs used in the experiments equals 10-20 (see section 3.1). The function $\gamma(\theta)$ is plotted in figure 2.8a for multiple L/d ratios. The figure shows that the maximum γ value is not located at θ=0.5π and not one but two maximums are visible. The two maximums occur due to symmetry. The maximum values of γ and $\theta_{\gamma=\gamma_{max}}$ (equations 2.30 and 2.31) are shown in figure 2.8b. The values for K can now be determined, from which the shape factor ξ can be determined. Figure 2.9 illustrates the dependence of ξ on d^* and K. The analytic expression is:

$$\log(\xi) = -0.55 + K - 0.0015K^{-2} + 0.03(1000)^{K-0.524} + \frac{-0.045 + 0.05K^{-0.6} - 0.0287(5500)^{K-0.524}}{\cosh\left(2.55\left[\log(d^*) - 1.114\right]\right)} \tag{2.29}$$

$$\gamma_{max} = \sqrt{a^2 + b^2} = \left(\frac{\pi}{4}\frac{L}{d}\right)^{-2/3}\left[\left(\frac{\pi}{4}\right)^2 + \left(\frac{L}{d}\right)^2\right]^{1/2} \tag{2.30}$$

$$\theta_{\gamma=\gamma_{max}} = \arctan(a/b) = \arctan\left(\frac{L/d}{\pi/4}\right) \tag{2.31}$$

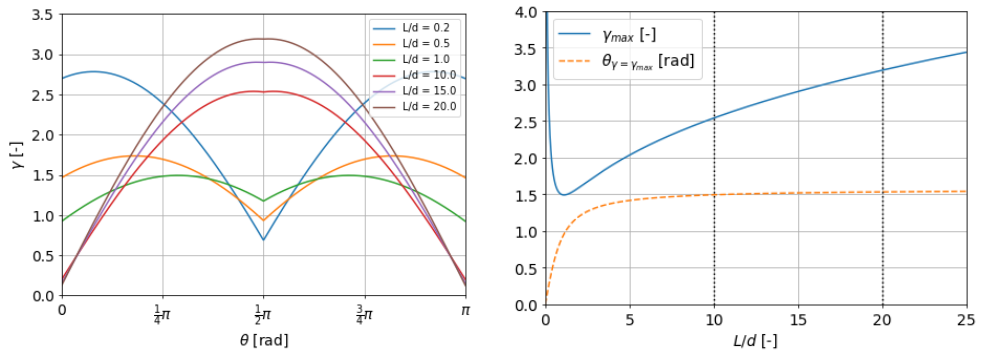

(a) γ as a function of θ

(b) γ_{max} and θ_{max} as a function of L/d

Figure 2.8: (a) γ as a function of theta for multiple L/d ratios (b) Maximum values for γ and θ as a function of L/d

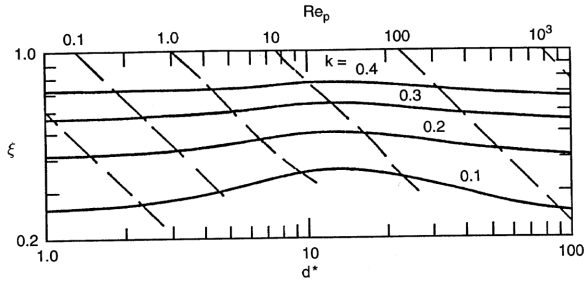

Figure 2.9: The shape factor ξ as a function of dimensionless particle diameter d^* and volumetric form factor K (R. Clift, 1978)

2.5.2. Wall effect

Wall effects occur in a horizontally confined fluid (here:water) in which a particle settles. The downward flux of the particle has to be compensated by an upward flux of the fluid. This counter flux has a retarding effect on the settling velocity of the particle. The retarding effect is a result of the counter flux increasing the drag on the settling particle and forcing the particle to orientate in a more aerodynamic position to allow more flow past the particle. It is important to eliminate wall effects as much as possible. Lau et al. (2010) did several experiments on wall effects on cylinders (4<L/d<21) in the inertial and turbulent flow regime (600<Re<16100) in cylindrical tanks. They developed two equations that determine the ratio of settling velocity in a column with finite width (D) to an unconfined column, the wall factor ($w_s/w_{s,\infty}$). This factor depends on multiple parameters, one of which is θ. *Note that here θ is differently defined as in figure 2.7.* The two equations by Lau et al. (2010) (2.32 and 2.33) are given below. Equation 2.32 describes the angle of a settling particle with the horizontal plane, see figure 2.10. The angle is a result of maximising the surface area exposed to the flow (recall equation 2.27). Equation 2.33 is a semi-empirical formula in which the force balance is taken into account (square root) and a factor that represents the correlation of the wall effect. **Note: d, l and D are in millimetres and θ in radians.**

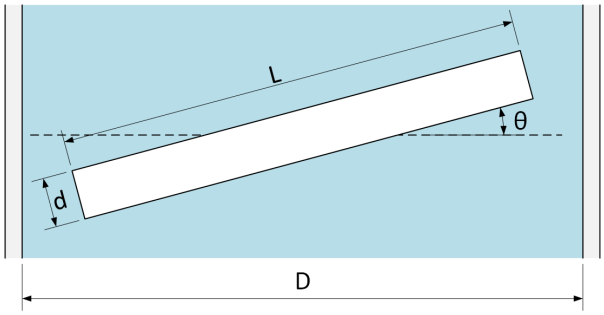

Figure 2.10: Settling of a cylindrical particle in a confined fluid

$$\theta = \frac{\pi}{2}\left\{\frac{0.005\left(\frac{L}{d}\right)}{0.005\left(\frac{L}{d}\right)+\exp\left[-7.0L^{-0.03}\frac{L}{D}\right]}\right\} \tag{2.32}$$

$$\frac{w_s}{w_{s,\infty}} = \sqrt{\frac{dL}{dL\cos\theta+\frac{\pi}{4}d^2\sin\theta}}\left[1-\left(\frac{d}{D}\right)^{3/2}\right] \tag{2.33}$$

2.5.3. Settling with a current

In general rivers always flow. Settling of a particle will therefor not only have a vertical velocity component due to gravity, but also a horizontal component from the current. In a tidal river like the *Oude Maas* currents occur bidirectional (upstream and downstream). During low water the current is directed downstream and during high water upstream. During the transition from high to low and vice versa there is a period of 'slack water'. During this period no current is present in the tidal river. This period is ideal for placing a bed protection because no horizontal velocity component has to be taken into account. In this thesis the settling of logs with a current is not researched. Nonetheless it is important to know what the effect of a horizontal velocity component is on the settling of a particle.

WL (1960) and de Reus (2014) researched the displacement of dumped rock in flowing water from a side dumping barge. They found that the upstream rocks block most of the incoming current, sheltering the rocks downstream. This leads to a compression of the rock volume, depicted in figure 2.11a. The magnitude of compression depends on the flow velocity (figure 2.11b) and the thickness of the dumped volume. Here thickness is the length scale of the rock volume perpendicular to the flow. Rock dumped perpendicular to the flow, figure 2.12a, has a smaller thickness than rock dumped parallel to the flow, figure 2.12b. *Note that the magnitude of the current at which the offsets in figure 2.11b occur are specific to the research of de Reus (2014).*

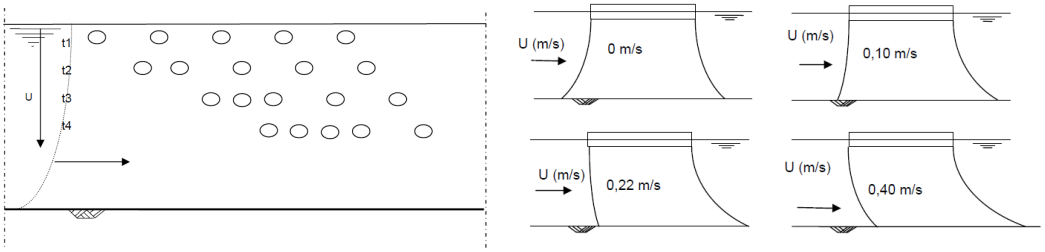

(a) Compression of a rock volume due to a current. The upstream rocks shelter the rocks downstream.

(b) Schematic representation of the offset due to a current

Figure 2.11: Compression and offsets of the dumped volume due to current (de Reus, 2014)

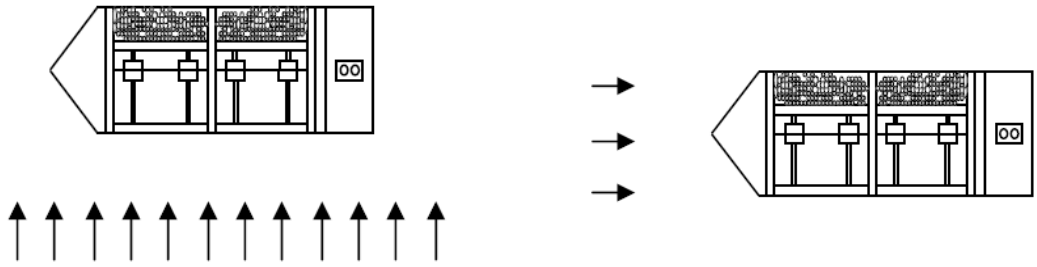

(a) Rock dumped perpendicular to the flow

(b) Rock dumped parallel to the flow

Figure 2.12: Perpendicular and parallel dumping of rock from a side dumping barge (de Reus, 2014)

The basic equation for the offset depends on the water depth (h), depth averaged velocity ($\overline{U}$) and settling velocity (w_s) and is given in equation 2.34. WL (1960) expanded the equation to take the angle between the

dumped rock and current into account. The research by de Reus (2014) found a slight alteration of those equations. The equations by de Reus are given in equation 2.35 and 2.36. Corresponding coordinate system is given in figure 2.13.

$$\text{offset} = h\frac{\overline{U}}{w_s} = h\frac{\sqrt{C_D/2}\cdot\overline{U}}{\sqrt{\Delta g d_n}} \tag{2.34}$$

$$x_{\text{offset}} = \sin\alpha\frac{h\overline{U}}{\sqrt{\Delta g d_n}}\sqrt{0.45C_D\cos\alpha^2 + 0.5C_D\sin\alpha^2} \tag{2.35}$$

$$y_{\text{offset}} = \cos\alpha\frac{h\overline{U}}{\sqrt{\Delta g d_n}}\sqrt{0.45C_D\cos\alpha^2 + 0.5C_D\sin\alpha^2} \tag{2.36}$$

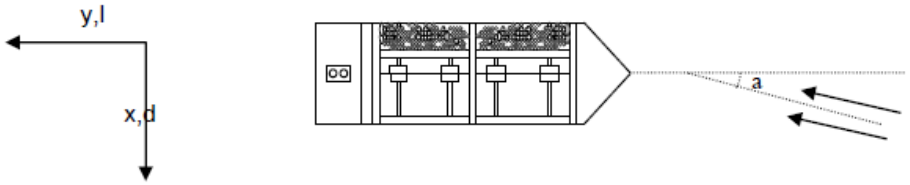

Figure 2.13: Coordinate system for equations 2.35 and 2.36 (de Reus, 2014)

de Reus (2014) found that for the rock dumped perpendicular to the flow the compression effect is negligible due to the small thickness of the volume. Small thickness leads to little sheltering of rocks downstream. The offset also decreased with increasing number of rocks dumped at once because downstream rocks are more sheltered. If we replace rock with logs and dump the logs perpendicular to the flow it can be expected that sheltering can also be neglected. If the offset equations can be used for logs is unknown but it is expected that with the correct value for the drag coefficient C_d a good guess can be made.

2.6. Magnus effect

The Magnus effect is named after Heinrich Gustav Magnus in 1852 (Magnus, 1999). He researched why cannonballs had a curved trajectory through the air. The phenomena is visualised in figure 2.14. The effect is related to the friction between the medium and the object. As a 2D rotating object travels through a medium (e.g. air or water) the relative velocity at the top and bottom of the object are different. One side of the object will move in the same direction as the trajectory (less relative velocity), while the other side moves in the opposite direction (more relative velocity). The medium at the side with the smaller relative velocity is able to stay attached to the surface longer (i.e. the point of flow separation occurs further behind the object). The streamlines of the medium at this side are deflected towards the other side. According to Newton's third law the resulting net force of the medium requires an opposite directed force generated by the object. The latter force is known as the Magnus force.

The Magnus force F_M per unit length of a (right circular) cylinder is described in equation 2.37 Nakayama and Boucher (1999).

$$F_M/L = \rho_w U G \qquad G = (2\pi r)^2 s = 2\pi r^2\omega \tag{2.37}$$

- U [m/s] (Relative) velocity
- G [m^2rad/s] Vortex strength
- s [revolutions/s] Revolution speed of the cylinder
- ω [rad/s] Angular velocity

A rotating cylinder will experience frictional torque. Frictional torque is the friction between a medium and the surface of a rotating object. The generated friction exerts a torque on the object opposite to the

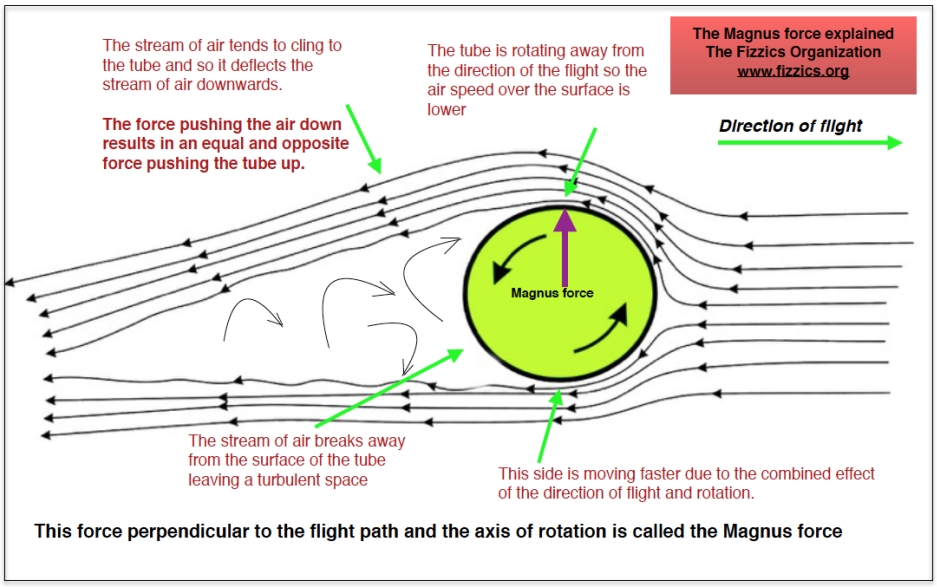

Figure 2.14: Magnus effect visualised Fizzics (2019)

angular velocity. The frictional torque can be divided into two parts, the two circular ends and the cylindrical part.

Considering a disc with radius r_0, thickness b and let $\mathrm{d}F_T$ be the friction force on an elementary ring area $2\pi r\mathrm{d}r$ at a given radius $r\omega$ (figure 2.15). Assuming that $\mathrm{d}F$ can be calculated in a similar way as normal drag, i.e. proportional to a friction coefficient (f) times an exposed surface area ($2\pi r$) times a velocity ($r\omega$) squared, the frictional force on one circular end of the cylinder is as follows Nakayama and Boucher (1999):

$$\mathrm{d}F = f\frac{\rho_w(r\omega)^2}{2}2\pi r\mathrm{d}r$$

Integrating over the radius the frictional torque T_1 is:

$$T_1 = \int_{r=0}^{r_0} r\mathrm{d}F = f\frac{\pi}{5}\rho_w\omega^2 r_0^5 \tag{2.38}$$

The same can be done for the cylindrical part, assuming equal friction coefficient and $r = r_0$, the friction force F' becomes:

$$F' = f\frac{\rho_w(r_0\omega)^2}{2}2\pi r_0 b$$

The frictional torque T_2 is $F'r_0$, or:

$$T_2 = \pi f\rho_w\omega^2 r_0^4 b \tag{2.39}$$

Combining equations 2.38 and 2.39 the total friction torque T is:

$$T = 2T_1T_2 = \pi f\rho_w\omega^2 r_0^4\left(\frac{2}{5}r_0 + b\right) \tag{2.40}$$

If we use cylindrical dimensions thickness d equals length L.

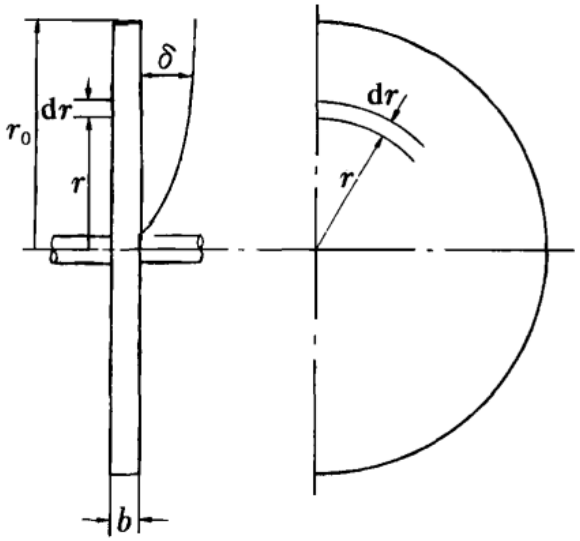

Figure 2.15: A revolving disc (Nakayama and Boucher, 1999)

3

Experimental setup

Two scaled physical model experiments were performed in the Fluid Mechanics Laboratory at the Civil Engineering & Geosciences faculty of Delft University of Technology.

The full scale (prototype) logs are scaled to model size in section 3.1. In section 3.2 the setup of the first model is presented. The first model tests the settling behaviour of logs for several release mechanisms. A qualitative analysis of the results gives insight in how logs settle, what can affect the behaviour and what differences can be observed for the different release mechanisms. The conclusions from the first model are implemented in the second physical model. The second model is presented in section 3.3. The model tests the stability of a log bed protection (log filter). A scaled log filter is constructed in a flow flume. The discharge in the flume is increased until movement or transport of the logs is observed. From the captured and recorded data the stability of the log filter is quantified. The collected data requires post processing. The methods used for post processing are discussed in section 3.4. Physical models are a scaled version of reality. Not every aspect of a physical model is equally scaled. In section 3.5 the different scales are summarised.

3.1. Model logs

3.1.1. Choice of material

Although logs can be accurately represented as right circular cylinders there are a few aspects that make logs different from cylinders. These aspect are listed below and shown in figure 3.1. Rootwards (logs with the roots still attached) are excluded from this research because their shape deviates too much from cylinders.

- Slightly crooked shape of logs
- Heterogeneous density and diameter
- Bark roughness
- Branch collars

(a) Crooked (b) Rough bark (c) Smooth bark (d) Branch collar

Figure 3.1: Aspects of logs that deviate from right circular cylinders.

A crooked (bend) shape affects the settling and rolling behaviour of a log. The log will try to settle in the most stable orientation (figure 3.2a). When a crooked log wants to roll, it will be difficult because the centre of mass is not located on the turning axis (figure 3.2b). The mass of a log is heterogeneous. The heavier parts of the log want to settle faster and are more resistant to external forces. The cross section of a log is generally circular. However locally deviations can occur. For example on places where branches are cut off (collars) the cross sectional shape is non-circular, figure 3.2c. This changes rolling and hydraulic loaded behaviour. The log is less likely to roll over a large collar. Collars also affect the interlocking behaviour of logs. Large collars of logs can interlock, increasing resistance to shear forces. Bark roughness impacts the force due to drag. A hydraulic rough surface experiences larger drag forces than a smooth surface.

For the above mentioned reasons it is chosen to use willow twigs as model logs. The primary reason for this is bark roughness. Using twigs instead of fabricated cylinders incorporates all the above mentioned aspects and can therefor be directly related to full scale logs (assuming bark roughness scales correctly). Willow is chosen as wood type because it is very common in The Netherlands, it grows quickly and is already available from the Room of the River project. In this projects trees have to be cut to accommodate the river adjustments and can therefor be used for a log bed protection. These logs have a length of approximately 5 m and diameters between 0.3-0.7 m, with a mean of 0.5 m.

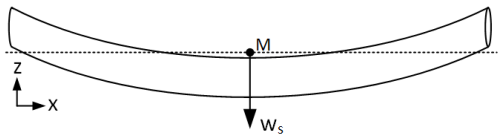

(a) Streamlined settling of a crooked shaped log

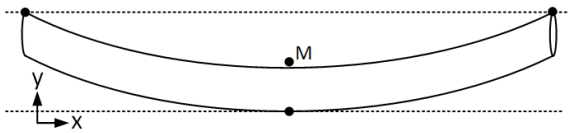

(b) Centre of mass offset from turning axis due to a crooked shape

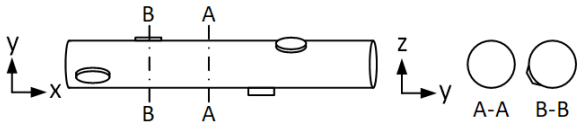

(c) Branch collars

Figure 3.2: Schematisation of a crooked shape and branch collars (M is the centre of mass, dashed line the turning axis)

3.1.2. Model log dimensions

The dimensions of the model logs should retain the hydraulic properties (Froude and Reynolds number) of the full scale (prototype) logs. This is not achievable since hydraulic scaling is done with Froude scaling, which does not allow for accurate Reynolds scaling. However the hydraulic load on a cylinder is dependent on the drag coefficient. This drag coefficient is roughly constant in the turbulent flow regime, see figure 3.3a. Because of this, lower or higher Reynolds numbers can be used in the model while maintaining decent accuracy for the hydraulic load. The model log diameters used in the experiments are 1-2 cm. Calculating the corresponding Reynolds numbers ($\mathcal{O}(10^5)$, see appendix F) shows that the model logs are still in the turbulent regime. The log length is set to 20 cm. The L/d ratio is then 1:10-1:20. Using figure 3.3b and some interpolation the corresponding drag coefficient is then considered constant in the turbulent regime with a value of 0.8.

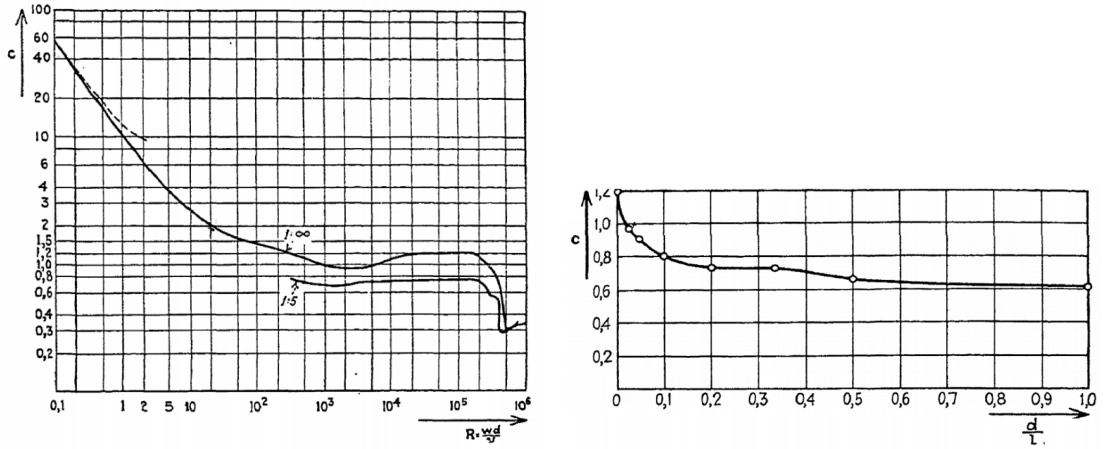

(a) Drag coefficients vs. Reynolds number for cylinders with infinite length and L=5d

(b) Drag coefficients vs. d/L of cylinders for Re=10^5

Figure 3.3: Drag coefficients vs. Reynolds numbers and slenderness (d/L) for right circular cylinders (Wieselsberger, 1914)

Willow branches of 1.5-2.0 m were used in this thesis. The diameter of the branches ranged from just over 2.0 cm to just below 1.0 cm. The branches were cut to 20 cm long twigs. Eleven categories were used, ranging from 1.0-2.0 cm, with increments of 0.1 cm. Each category had a range of ±0.05 cm (table 3.1). The diameter of each twig was measured at both ends. The average diameter determined in which category the twig belonged. Twigs thicker than 2.0 cm, thinner than 1.0 cm, larger or shorter than 20 cm or with a very asymmetric shape were excluded. Each category was marked with a piece of coloured tape, except for category 1.7 cm (figure 3.4). The twigs are submerged in water to saturate. The saturation rate and density was monitored periodically during the course of this thesis. The twigs are referred to as logs or model logs.

Figure 3.4: Twigs marked with coloured tape

Category	Limits [cm]	# of logs
1.0 cm	0.95≤ d <1.05	17
1.1 cm	1.05≤ d <1.15	42
1.2 cm	1.15≤ d <1.25	66
1.3 cm	1.25≤ d <1.35	110
1.4 cm	1.35≤ d <1.45	128
1.5 cm	1.45≤ d <1.55	94
1.6 cm	1.55≤ d <1.65	96
1.7 cm	1.65≤ d <1.75	128
1.8 cm	1.75≤ d <1.85	154
1.9 cm	1.85≤ d <1.95	144
2.0 cm	1.95≤ d <2.05	112

Table 3.1: Eleven categories, their corresponding diameter range and number of logs available.

The density of the model logs did not meet expectations when the experiments had to be performed. Nails were used to increase the weight of the logs to achieve a desired density, see section 4.

3.2. Settling experiment

The settling behaviour of logs is tested using a wooden rectangular tank of 60x60x50 cm, see figure 3.5a. In order to view settling of the logs from the side two of the sides are made out of perspex. Logs are dropped using various methods and their behaviour (settling velocity and settling distribution) are observed and recorded. During the experiments a video and photo camera are used. The video camera is used to capture the settling velocity and settling behaviour from a side view. The photo camera is placed above the tank facing down to record the end locations of the logs. The water depth in the tank is 46.5 cm so that it is equally scaled to the

log dimensions (≈1:30). A radial pattern is placed on the bottom of the tank to quantify the location of the midpoint of the logs in the horizontal plane. The diameter of each circle increases with 5 cm. A full circle is split in 72 segments, covering 5 degrees each. A striped pattern is placed on one side of the tank to quantify the location of the midpoint of the logs to extract the settling velocity. Each column is 5 cm wide and each row is 1 cm thick.

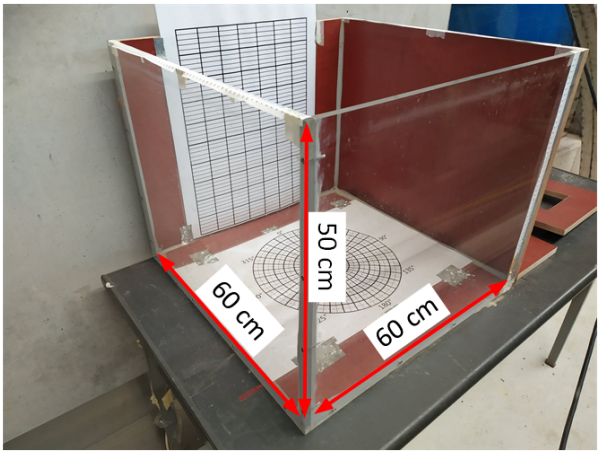

(a) 3D view

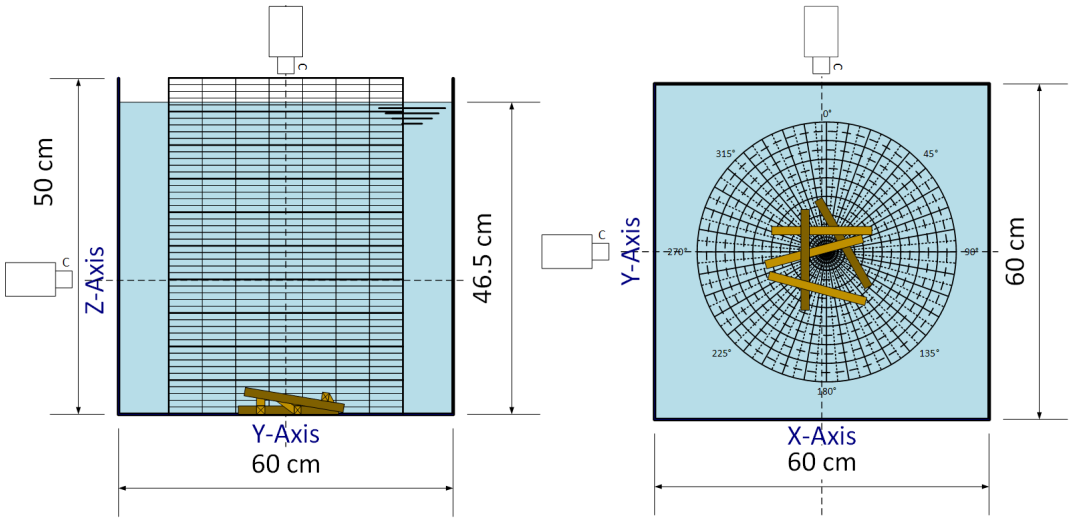

(b) Side and top view

Figure 3.5: (a) 3D view of the tank (b) Left: side view of the setup, both cameras used Right: top view of the setup, either camera used

3.2.1. Release mechanisms

Four release mechanisms are explored. The first mechanism is manual release of the logs, one by one. A wooden beam is placed over the tank. This beam acts as guidance so that the logs are dropped as horizontally and centred as is possible. Each log is dropped from a specified height in horizontal or vertical orientation. The main purpose of this first method is to measure settling velocity and gain insight in the spatial variation of the settling locations. A manual release along a beam is imperfect and logs are likely to hit the water with some angular velocity and angle. Expected is that the rotation is minor and angle small enough so that they can be neglected after the log has hit the water. If it is observed that the rotation was too fast and/or angle too large the experiment is discarded and repeated.

The second method is a hatch, see figure 3.6a. The hatch simulates a sudden release of multiple logs at once. A comparison can be an excavator claw that quickly opens. A claw is incapable of holding a large amount of logs, which is why the maximum number of logs that is dropped using the hatch is set to 10. The logs are placed on the hatch, which is then opened. This is repeated a couple of times, depending on how many logs are available. These experiments gain insight in what the stacking behaviour is of logs for multiple

drops at one location.

The third method is a funnel, see figure 3.6b. The funnel represents a hatchbarge ship in which a large amount of logs can be stored and dropped at once. A large amount of logs (bulk) is placed in the funnel after which they are released. Dropping a large number of logs changes the behaviour of how the logs settle. If the number of logs is large enough hindered settling can occur, reducing settling velocity. Near the bottom, collisions between logs also changes how the logs end up on the bed.

The fourth is the manual release of logs from a slope, see figure 3.6c. This method tests the Magnus effect. The Magnus effect is the phenomena where due to the angular velocity of a rotating object, a force is generated perpendicular to the velocity vector of the object. The logs obtain the required angular velocity from rolling off the slope.

Details of the hatch and funnel mechanism can be found in appendix G.

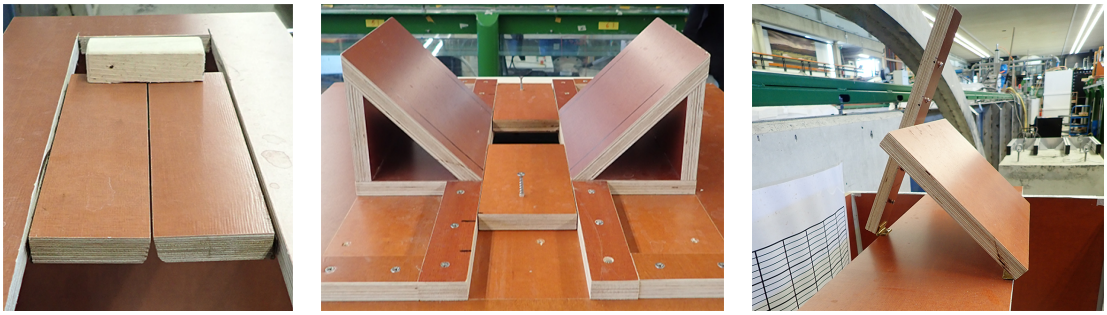

(a) Hatch mechanism (b) Funnel mechanism (c) Slope mechanism

Figure 3.6: Release mechanisms used in the settling experiment

The number of logs used for each experiments is shown in table 3.2. Experiment IDs are defined using three letters and one number. The first position indicates the drop orientation, the second position the drop method and the third the objective of the test. Letters used for each position are listed below. For example HMV indicates that the logs are released horizontally (H) by hand (manual, M) and the settling velocity (V) is measured. The number at the end indicates the log diameter (so 10 refers to log diameter 1.0 cm). No experiments were done with log diameter 1.6 cm, explained in section 4.3.

1. (H) Horizontal, (V) Vertical
2. (M) Manual, (H) Hatch, (F) Funnel, (S) Slope
3. (S) Settled distribution of single logs
   (T) Settled distribution of stacked logs
   (B) Settled distribution of bulk
   (V) Settling velocity
   (M) Magnus effect

Number	10	11	12	13	14	15	17	18	19	20
Experiment	Number of logs									
HMV	10x1	10x1	10x1	10x1	10x1	10x1	10x1	10x1	9x1	10x1
HMS	10x1	10x1	10x1	10x1	10x1	10x1	10x1	10x1	10x1	10x1
HMT	10x1	40x1	40x1	14x1	26x1	29x1	25x1	20x1	25x1	20x1
VMT	10x1	40x1	40x1	14x1	26x1	29x1	25x1	20x1	25x1	20x1
HHB	1x10	4x10	4x10	1x10	2x10+6	2x10+9	2x10+5	2x10	2x10+5	2x10
HFB	17x1	40x1	50x1	14x1	26x1	29x1	25x1	20x1	25x1	20x1
HSM	10x1	10x1	10x1	10x1	10x1	10x1	10x1	10x1	10x1	10x1

Table 3.2: Number of logs used for each settling experiment

3.3. Flume experiment

3.3.1. General setup

The second experiment is performed in a flow flume with dimensions 14.30x0.40x0.38 m (length x width x height). The flow depth should be smaller than 1/3 the flume width (38/3=12.7 cm) to be able to neglect wall friction effects (Stuifbergen, 1981). Chosen is a flow depth of 14 cm (scale=1:100) and wall friction effects are assumed to be negligible.

The flow into the flume is very turbulent and non-uniform. To achieve a uniform flow the minimal required length before the test section needs to be 30-50 times the water depth (Schiereck, 2016). With a water depth of 0.14 m this length is 4.2-7.0 m. Due to the presence of a weir at the exit of the flume the test section should not extend to the end of the flume. A weir causes velocity potential refraction (flow contraction). Assumed is that 3.0 m in front of the weir is sufficient to neglect this influence.

The transition from a smooth bed (false bed) to a rough bed (log filter) affects the boundary layer. The boundary layer has to adjust to the new roughness. When assuming that the development of this boundary layer is similar to the development of a mixing layer, the length required for the boundary layer to fully develop should be six times the water depth, or 0.84 m (Schiereck, 2016). In the flume this length is 1 m and known as the roughness layer. The log filter is 2 m long.

On full scale a total of five metres is available for the bed protection, two metres for overhead and three metres for the log filter, see figure 1.2. This allows a filter thickness of three to ten log layers. Scaling this down to model size, with 4 cm overhead in the flume and 14 cm flow depth, 20 cm remain for the log filter. If only logs with a 2.0 cm diameter are used a total of ten layers is possible. A minimum of four layers is desired for the log filter. Three layers to represent the filter function, as outlined by Bouman (2018), and one extra layer that acts as stability layer. This layer is allowed to deform and be damaged to a certain degree such that the filter function is not lost. Due to the limited number of logs available four layers will be constructed. The maximum required log filter height is 8.0 cm. As bed material sand is chosen with a d_{n50}=400 μm. This is coarse enough to not become mobile while testing and fine enough to not be large relative to the log diameter.

The test section is 1.5 m long, from the end of the mesh to the end of the log filter. The first and last 0.25 m (approximately four times the filter thickness) of the log filter are used to allow the flow to fully enter and exit the log filter.

These considerations lead to the design shown in figure 3.7. At locations 1, 2 and 4 the water level is measured. At location 3 an Acoustic Doppler Velocimeter (ADV) is located to measure the velocity profile. The red box indicates the section that is covered by a submerged laser. The 1 metre section from a smooth to rough bed and the first 50 cm of the log filter is covered with a coarse steel mesh. This is to prevent logs at these locations to become mobile. The mesh is assumed coarse enough to not influence the roughness. At the end of the log filter no mesh is placed to not limit mobility of logs that would otherwise become mobile. One should keep in mind though that because the flow exits the log filter, an upwards flow increases lift forces, potentially mobilising logs before mobility would occur from shear stresses.

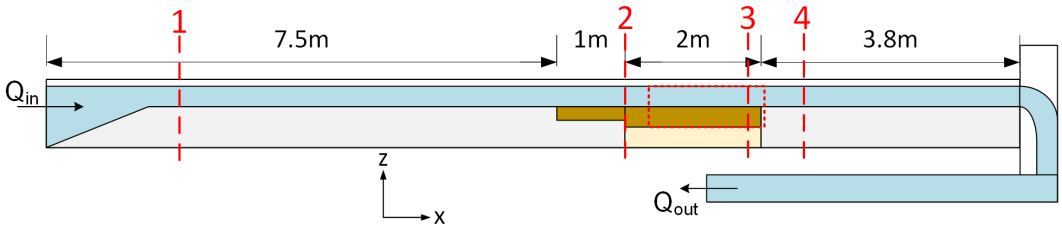

Figure 3.7: Side view of flume setup, vertical dimensions not to scale.

3.3.2. Details of the test section

A detailed overview of the test section is given in figures 3.8 and 3.9. The log filter is build from two main layers. The 'foundation' layer consists of three layers that simulate the filter function. Limitations of the placement accuracy of the release mechanism did not allow these layers to be placed by dumping. The foundation layer is constructed by hand. The resulting top layer of the foundation layer is considered to be sufficiently representative of a dumped layer. Logs of the second (middle) layer were placed in the centre. Where normally other logs would be located next to these logs, short 4-6 cm, 1.5 cm thick red PVC rods with a density

of 1500 kg/m^3 were placed instead. The 'stability' layer is the layer which is tested for stability. These logs are placed using the release mechanism.

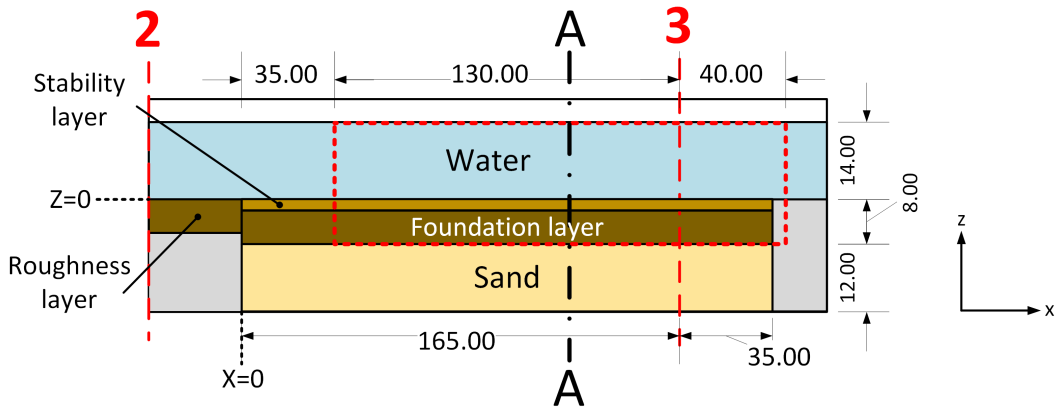

Figure 3.8: Detailed side view of the flow flume model

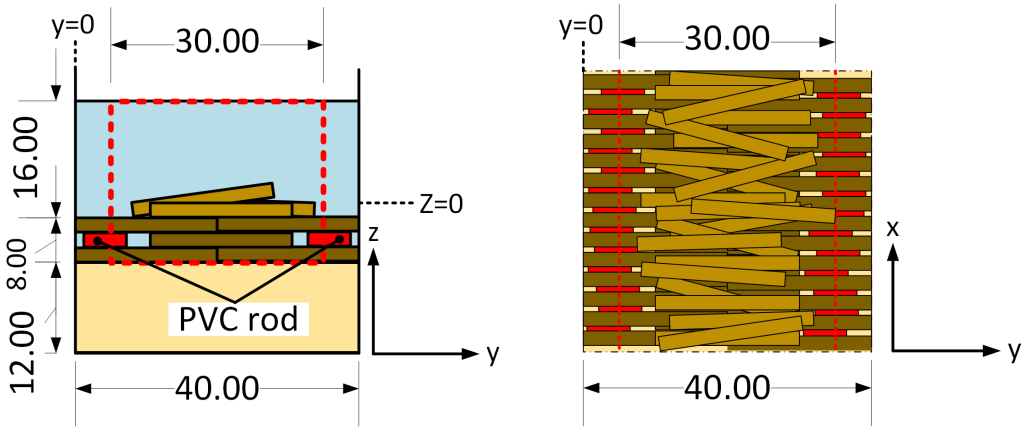

(a) Cross section as location A-A

(b) Top view of a part of the test section

Figure 3.9: (a) Cross section of the test section (b) Top view of a part of the test section

3.3.3. Measurements and instruments

Several measurements are done before, during and after each experiment. The measurements and corresponding instrument as well as their location(s) are listed in table 3.3.

Measurement	Instrument	Location
Time	Computer	-
Discharge	Rehbock weir	-
Water level	Depth gauge	1, 2 & 4
Velocity profile	Velocimeter (ADV)	3
Bed profile	Laser	Test area
Video	Camera (side and top)	Test area

Table 3.3: Measurements, instruments and locations of flume test

Acoustic Doppler Velocimeter

An Acoustic Doppler Velocimeter (ADV) measures the flow velocity using the Doppler effect. The Doppler effect is the change in pitch of a sound when there is a relative velocity between the source and the receiver. For example a police car with sirens turned on travels passed you on high speed. When the car approaches the pitch of the siren rises, and when the car passed the pitch lowers.

The Vectrino ADV from Nortek AS (NortekAS, 2017) transmits an acoustic pulse. This pulse is echoed by the moving particles in the water. The echo received by the ADV is translated into a velocity. The ADV used in this experiment is a side looking ADV, figure 3.10a. This ADV measures velocities in three directions (x, y and z) at 5 cm from the probe head in a 3-15 mm volume, figure 3.10b.

The water in the flume is too clear for the ADV pulses to echo. Small hydrogen bubbles are created in the water using electrolysis. A stainless steel rod (anode) was placed over 2 m upstream of the ADV and a mesh of horizontal platinum wires (cathode) was placed in front of the ADV (indicated by the red arrow in figure 3.10a). By electrolysis hydrogen bubbles are created at the cathode end and oxygen bubbles at the anode end.

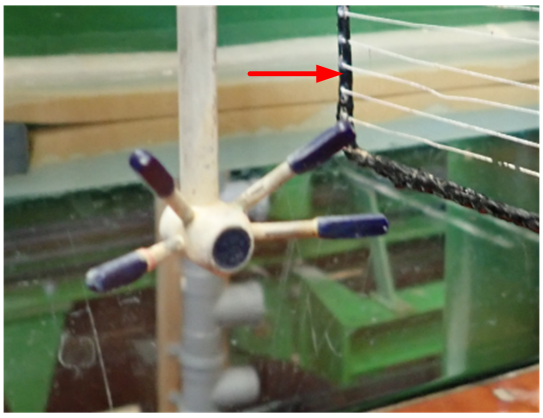

(a) Side looking ADV in the flume. Red arrow the platinum wires.

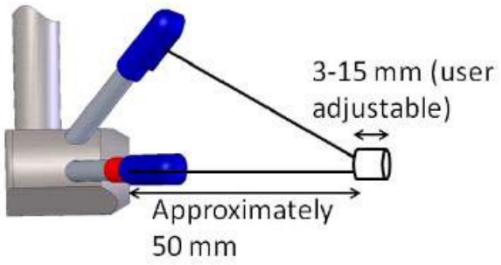

(b) ADV measurement volume (NortekAS, 2017)

Figure 3.10: (a) ADV in the flume (b) ADV measurement volume

Laser

Bed level scans are done before and after each experiment. A laser is placed in a 'boat' that can be partially submerged, figure 3.11. This is required to eliminate refraction of the laser signal due to surface waves. The boat is connected to a vertically adjustable mount. The mount can be moved across the width of the flume. The mount is placed on a cart that can travel along the flume. This construction allows the laser to move in 3D. The laser scans an area of 170x30 cm (indicated by the red dotted area in figures 3.7 to 3.9). This covers the entire length of the test area and 75% of the flume width.

The cart on which the mount is placed has a wheel that acts as a trigger. When the cart is moved the wheel rotates, generating pulses that are send to the laser. This means that only in the longitudinal direction of the flume measurements can be done. By moving the mount in transverse direction after each pass a 2D height map of the log filter is created.

Each pass of the laser covers 170 cm, see figure 3.9. The laser could not cover the entire width of the flume but only the centre 30 cm. The laser is moved 0.5 cm after each pass, meaning a total of 47 passes are done to create one height map.

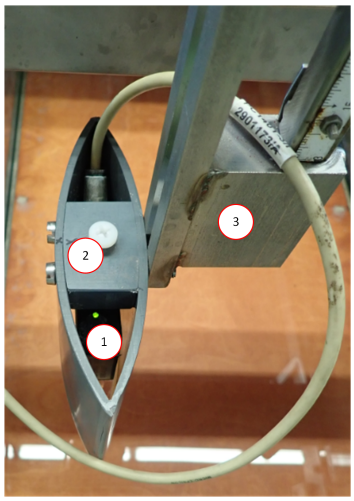

Figure 3.11: (1) Laser (2) Boat (3) Mount

Rehbock weir

The Rehbock weir is a rectangular weir that can be used to accurately calculate the discharge of an open channel flow (here: return flow). The Rehbock weir equation describes the discharge over the weir as a function of the water head over the weir to weir height ratio, equation 3.1.

$$Q[m^3/s] = q_{Rehbock} \cdot B_{Rehbock} = m' \frac{2}{3} h_e \sqrt{\frac{2}{3} g h_e} B_{Rehbock} \tag{3.1}$$

$$m' = 1.045 + 0.141 \frac{h_e}{h_w} \tag{3.2}$$

$$h_e = h_k + 0.0011 \tag{3.3}$$

- h_k [m] Water level at two times the weir height, upstream
- h_e [m] Effective height
- h_w [m] Weir height

Water level h_k is digitally measured in voltages. Using the function $h_k = f(V)$ from calibration the voltage is transformed into h_k from which the discharge is calculated.

3.3.4. Test series

The test series consists of five types of experiments, listed below. The first type (RP) tests the effect of the bed roughness on the flow above the log filter. The second type (SP) tests the stability of the log filter for different log diameters and densities for logs perpendicular to the flow. The third type (SR) also tests the stability of the log filter but for logs parallel to the flow. The fourth type (CP) tests the stability of the log filter for a collection of logs with different diameters perpendicular to the flow. The last type (BP) tests the effect of backfilling the log filter with sand on the stability. A list of all experiments is presented in table 3.4. Cross sections of each experiment can be found in appendix H.

Some experiments are not only tested for stability. For example experiment SP18b tests the stability of the log filter and during the experiment the internal flow is observed by releasing dye (dissolved potassium permanganate) near the log filter. A second example is experiment SP17c. Before the stability test is started a velocity profile is measured that can be used for analysis of the flow above the log filter.

- RP: Roughness, perpendicular orientation
- SP: Stability, perpendicular orientation to the flow
- SR: Stability, parallel orientation to the flow
- CP: Collection (grading) of logs with different diameters, perpendicular orientation to the flow
- BP: Backfilling of the log filter, perpendicular orientation to the flow

Experiment	d	2D scan		Measurement		Observation
	[cm]	Before	After	Velocity profile	Stability	Internal flow
RP18a	1.8	✓		✓		
RP18b	1.8	✓		✓		
RP18c	1.8	✓		✓		
SP18a	1.8	✓	✓		✓	
SP18b	1.8	✓	✓		✓	
SP18c	1.8	✓	✓		✓	✓
SP16a	1.6	✓	✓	✓	✓	
SP16b	1.6	✓	✓		✓	
SP16c	1.6	✓	✓		✓	
SP14a	1.4	✓	✓		✓	
SP14b	1.4	✓	✓		✓	
SP14c	1.4	✓	✓	✓	✓	✓
SP17a	1.7	✓	✓		✓	
SP17b	1.7	✓	✓		✓	
SP17c	1.7	✓	✓	✓	✓	
SR18a	1.8	✓	✓		✓	
SR18b	1.8	✓	✓		✓	✓
SR18c	1.8	✓	✓		✓	
CP15a	1.5	✓	✓		✓	
CP15b	1.5	✓	✓		✓	
CP15c	1.5	✓	✓	✓	✓	
BP14a	1.4	✓	✓		✓	
BP14b	1.4	✓	✓		✓	

Table 3.4: All flow flume experiments

3.4. Data processing

Before data can be collected from equipment, like an ADV, one must make sure that they are calibrated. When calibrated the equipment can be used to collect data. This data needs to be post-processed to remove any data point that is not related to the parameter that is measured (most commonly spikes in a data series). This section outlines the steps taken in post-processing.

3.4.1. Calibration

The height h_k over the Rehbock weir (from which discharge is calculated) is digitally recorded by reading the voltage (V) on from a voltmeter. From calibration the $V - h_k$ relationship is obtained. The submerged laser also needs to be calibrated. It is important to note that the signal from a laser is dependent on the medium (here: air or water). The laser thus has to be calibrated while submerged. The laser measures the distance z_{laser} to the bed and outputs a corresponding voltage (V). From calibration the $V - z_{laser}$ relationship is obtained. Calibration graphs are provided in appendix I.

3.4.2. Post processing

There are two signals for which post processing was needed, the Laser and ADV signal. No spikes in the Rehbock weir signal were observed, so no post-processing was required.

Laser signal

The laser signal only needs to be checked for measurements that were outside the accuracy range of the laser (8-26 cm). The minimal and maximum distance to the bed are 13 cm and 21 cm respectively. Protrusion of logs above the bed level was never larger than 2 cm, meaning a minimal distance of 11 cm was measured at all times.

The laser had a measuring frequency of 10 Hz/mm. The formula obtained from calibration was used to directly convert the voltage to a distance (in cm) during a measurement. The distance was then adjusted to a distance with respect to the bed level, see figure 3.12 and equation 3.4. With all measurements within the range of the laser, it is sufficient to only compute the average value per mm.

$$z_{laser} = f(V) \qquad z = z_{laser} - (h - h_{laser}) \tag{3.4}$$

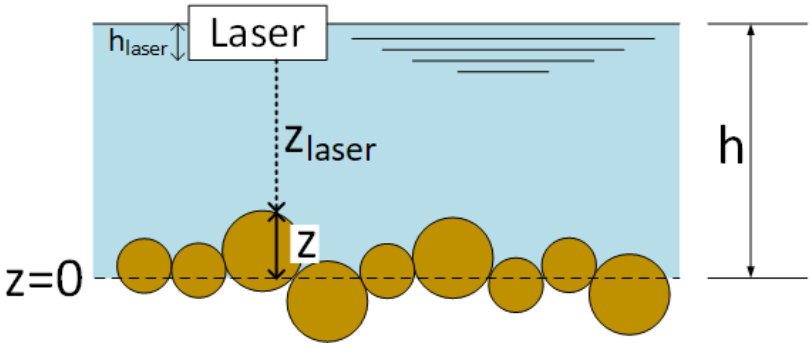

Figure 3.12: Graphical representation of the measured height by the laser compared to the coordinate system.

ADV signal

The data collected from the ADV requires post processing for several reasons. Firstly, the signal correlation and Signal to Noise Ratio (SNR) thresholds need to be met. This means that only data points where these two thresholds are exceeded (correlation and SNR values larger than the threshold) are taken into account. It is recommended that the correlation threshold is 80% and the SNR threshold 15%.

A reliable method is the phase-space threshold method developed by Goring and Nikora (2002). The method defines an enclosed ellipsoid around the data points. The points outside the ellipsoid are considered as spikes. The spikes are replaced by interpolation of a third order polynomial. The function for the polynomial is found from fitting through 12 data points at either side of the spike. At each iteration the enclosed ellipsoid shrinks. Iteration continues until replacement of spikes no longer has an effect on the enclosed ellipsoid (i.e. spikes are no longer detected or the number of spikes is minimised).

3.5. Scale effects

A perfect physical model scales all forces equally, retaining all properties and characteristics of the prototype. However this is not always achievable. When a physical model scales improperly, a discrepancy (scale effect) is introduced that affects the results of the research. Because of this results are not directly applicable to the prototype without taking these scale effects into account. Scale effects are quantified by determining the ratio of the parameter (i) between model and prototype (equation 3.5). A physical model always aims to have $n_i = 1.0$. All parameters and scales are summarised in table 3.5.

$$n_i = \frac{i_{model}}{i_{prototype}} \tag{3.5}$$

Parameter	Symbol	Prototype	Model	n_i
Water depth	h [m]	14.0	0.14 (0.47)	100 (30)
Flow velocity	$\overline{U}$ [m/s]	2.0	0.20	$\sqrt{100}$
Log length	L [m]	5.0	0.20	25
Log diameter	d [m]	0.3-0.7	0.01-0.02	≈33
Slenderness	L/d [-]	7-17	10-20	1.18-1.43
Froude	Fr [-]	0.17	0.17	1
Reynolds	Re [-]	10^7	10^4	10^3

Table 3.5: Prototype and model parameters. The number between brackets is the water depth for the settling experiment.

Three different type of scales can be distinguished. The first is the geometry scale. The model logs are of the order $\mathcal{O}(30)$ smaller than the prototype logs. The slenderness scale is not scaled 1:1 because the length of the prototype logs is scaled less. The effect of a different slenderness is assumed to be negligible. The second type of scale is the flow scale. The water depth has a much larger scale than the geometry scale. This was

required to neglect 2D effects of the flow in the flume. Also the flume did not have sufficient height if the water depth had the same scale as the geometry of the logs. The last scale is the hydraulic scale. Scaling is done to preserve the Froude number (1:1). The Reynolds number is therefor scaled with $\mathcal{O}(1000)$. For the load on the logs however this has little effect as discussed in section 3.1.2.

Because the water depth is scaled three times more than the log geometry the flow velocity distribution acting on logs is different. This is visualised in figure 3.13. Although the shape of the velocity profiles is similar the model logs experience larger flow velocities. For the stability of the logs this has negligible effect because the shear velocities are a property of the velocity profile. However when the model logs are transported higher up in the water column they will experience larger velocities and are therefor transported more easily than prototype logs will be.

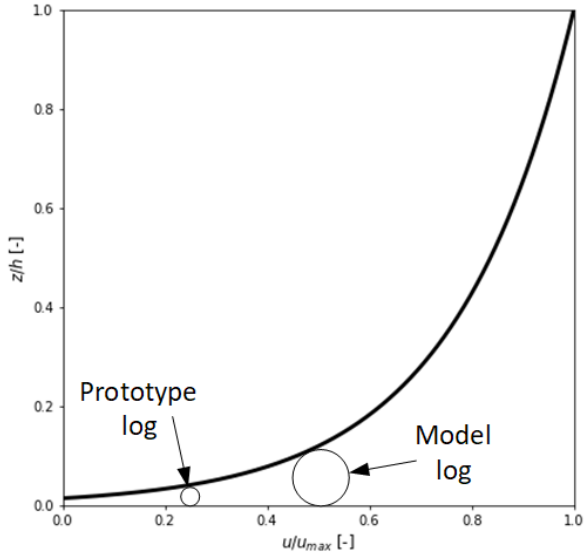

Figure 3.13: Model and prototype log diameter scale compared to velocity profile

4

Saturation process

No knowledge of the natural saturation rate of logs was found. The only indication of the total saturation time required was a note in the KRW pilots (Sieben, 2016). Logs were left to saturate over several years. With a log length scale of 1:25 and assuming linear scaling it was expected that the model logs would saturate in roughly 2-3 months. After one month of monitoring the density it was concluded that the logs would not fully saturate in 2-3 months. It was chosen to investigate potential causes for this slow saturation rate and possible solutions to increase the saturation rate.

4.1. Saturation rate

The saturation rate is here defined as the rate at which the density of a log increases when submerged in (fresh) water. When a log is submerged, the trapped air inside the log is slowly replaced by water. When all the air is replaced by water the log is fully saturated.

A control group, consisting of an assortment of logs with diameters of primarily 1.6 cm, 20 cm long logs, is measured over a period of eight months. The density ρ_{log} in kg/m^3 and saturation rate in density per day (ρ_{log}/day) are shown in figure 4.1.

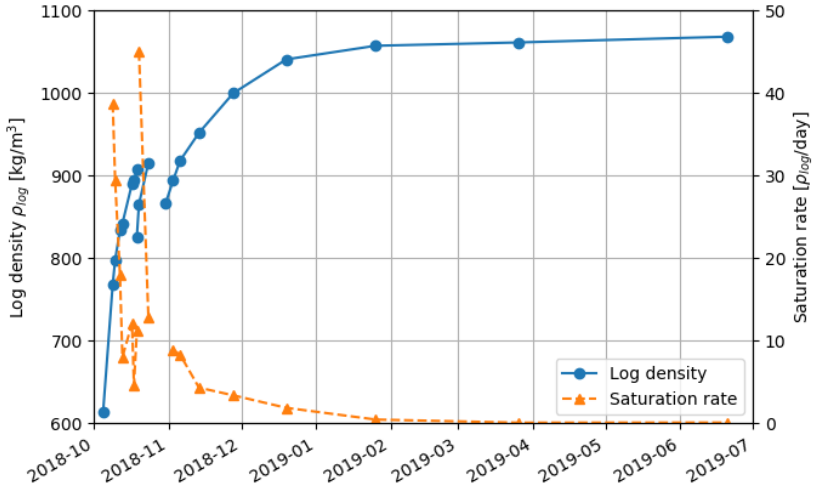

Figure 4.1: The density and saturation rate of the control group from October 2018 to July 2019

Three periods can be seen in figure 4.1. The first period, from October 4^{th} 2018 to October 18^{th} 2018, shows a rapid increase in density but also a rapid decrease in saturation rate. The density is increased by 50%, while the saturation rate decreased to roughly 20% of the initial rate. If this trend continued the density never reach a desired value of 1100 kg/m^3 or higher before the experiments are performed. It was suggested that the bark of the logs acted as a barrier for water to penetrate the wood.

The bark was stripped off the logs and the logs were measured again. This second period, from October 18^{th} 2018 to October 23^{th} 2018, shows a similar trend as in the first period. Removing the bark initially decreased the density of the logs, which means that the mass of the bark contributes a lot to the overall density of the wood at that point. The saturation rate increased after removal of bark. This can logically be explained that by removing bark more dry wood came into direct contact with the water and increasing the surface area. One of the stripped logs is shown in figure 4.2. From analysing this log it became clear that bark indeed acts a barrier. Both ends of the log (solid red boxes) are the most saturated while the middle parts of the log is relatively dry. A clear transition between wet and dry can be seen (dashed red box), showing that the log saturates from end to centre.

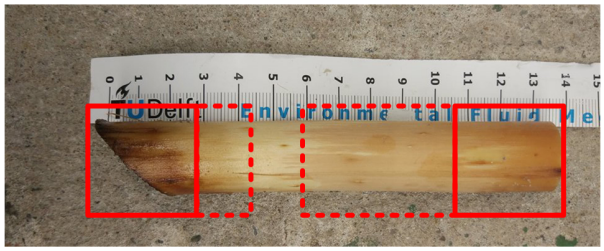

Figure 4.2: A log where the bark is stripped off

More logs were used to see how a log saturates and what could accelerate the saturation rate, see section 4.2. This meant that some logs were removed from the control group, slightly decreasing its overall density again. From this point period three starts, from October 30^{th} 2018 up to July 20^{th} 2019. The logs now stripped of bark were left to saturate. Water was periodically refreshed. The density kept increasing throughout this period, but with each measurement the absolute increase was lower than the previous measurement. This can also be seen in the saturation rates, which decreased throughout this period. The last measurement showed a density of 1068 kg/m^3 with a saturation rate of 0.08 ρ_{log}/day. This is lower than the desired density of 1100 kg/m^3 or higher.

4.2. Internal saturation

The internal saturation of a log is investigated using two methods. The first method is drilling holes, the second cutting logs in shorter pieces. Holes, 2 mm in diameter, are drilled through the width of a log, evenly spaced. Logs of 20 cm are cut to pieces of 10, 5 and 2 cm.

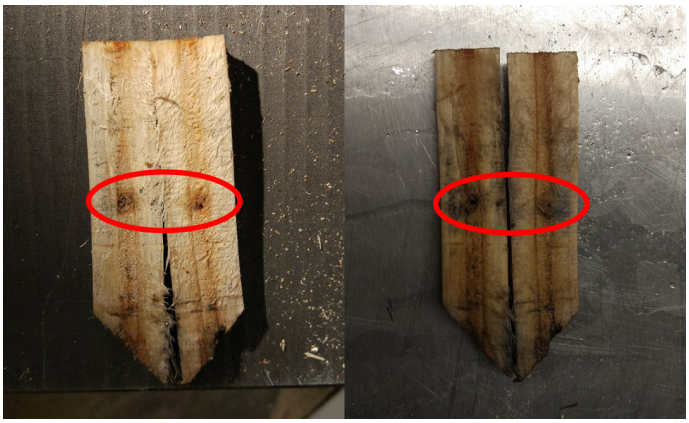

(a) (Left) One day after drilling (Right) Submerged for one day after the left image

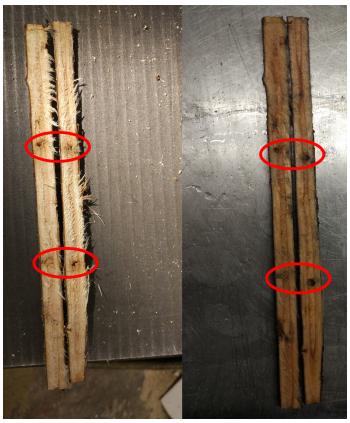

(b) (Left) One day after drilling (Right) Submerged for one day after the left image

Figure 4.3: Two logs where holes are drilled, indicated by the red circles

Figure 4.3 shows two logs where holes are drilled, indicated by the red circles. When the holes were drilled, the logs were submerged. After one day, when the saturation is quickest (as seen in the previous section) the

logs are cut along the length of the log. This is shown in the left image of each figure. A circular pattern of saturation is observed, however it is very small. In order for this method to be effective a lot of holes have to be drilled, which is practically unfeasible. Moreover the holes can clog up, reducing the effect in the long term. The two halves of the logs were submerged again for one day. This can be see in the right image of each figure. The logs can now saturate along the entire length, neglecting the effect of drilling holes.

Figure 4.4 shows a log cut in 2 cm pieces. The top image shows the saturation after the log is cut, the bottom image is one day after the log is cut and submerged again. The burn marks from cutting in the middle six pieces clearly show that the centre of the log is far less saturated. Nonetheless some saturation along the circumference of the pieces can be observed, indicated by the red arrows. This is probably related to the fact that bark was stripped of the log. One day after cutting the pieces already show far more saturation. This confirms that most of the saturation process is along the length of the log.

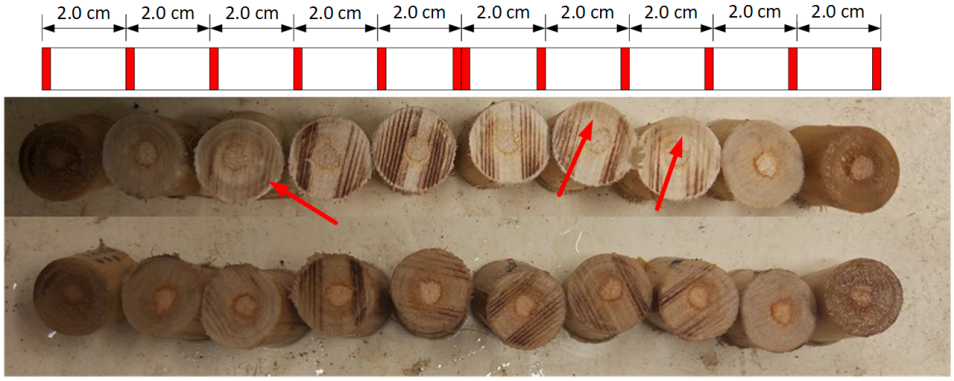

Figure 4.4: One 20 cm log cut in 2 cm pieces. The sides that are visible are shown in red. (Top) Saturation after cut (Bottom) Saturation one day after cut and submerged

The longitudinal saturation of logs is related to the wood cell structure. Wood cells run parallel through a log (tracheids). In softwood (like willow) these cells are open, connecting it to other cells. This means that these cells can act as conduits. A conduit is a channel for conveying water or other fluids. Ray cells, running along the cross section of a log, allow for water to move across to other cells. Ray cells are much shorter and less effective conduits. In hardwood the cells are all closed, meaning they do not act as conduits. Instead, a pore (vessel) is present. Both wood types and their general structure are presented in figure 4.5.

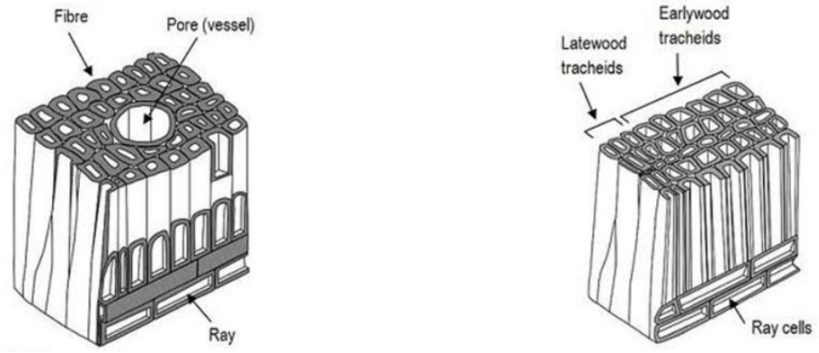

Figure 4.5: (Left) Hardwood (Right) Softwood (AndrewGoTo, 2019)

4.3. Increasing the density

Due to a limited amount of time available before the settling experiments had to be performed the density of the logs was artificially increased so that the settling experiment could be performed. The weight of the logs was increased using nails (nickle plated to prevent corrosion). For each diameter, a nail was hammered through the centre at both ends, see figure 4.6.

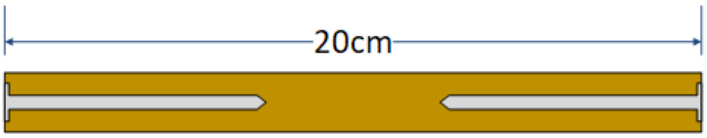

Figure 4.6: Impression of a nailed log

The aim was to achieve a density of 1100 to 1200 kg/m^3. Expecting an increase of 100 to 150 kg/m^3 for the rest of the saturation period the logs would not become unnaturally dense. Not all logs from each log diameter were used. This was not necessary to perform the settling experiment and also allowed the remaining logs to saturate naturally for a longer period of time. The logs that are used for the settling experiment are referred to as the first batch.

Depending on the density and the log diameter a matching nail was chosen, see appendix J. Afterwards the mean density was measured in sets of four or five logs. The matching nail for logs with diameter 1.6 cm was not found. These logs are not used in the settling experiment. The achieved densities are shown in figure 4.7 and conclude that nails are a successful method to increasing the density. A standard deviation of less than 2% was measured except for log diameters 1.1 and 1.3 cm, where 5.80% and 2.98% was measured respectively, see table 4.1.

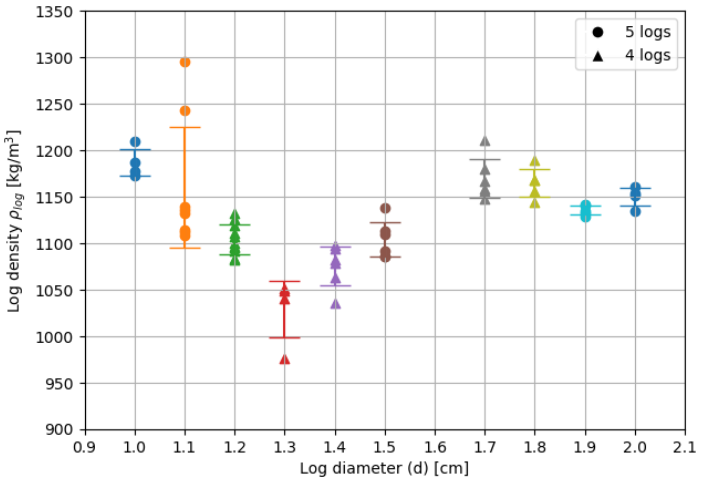

Figure 4.7: Density measurements of the logs used in the settling experiment after nailing (first batch).

d [cm]	1.0	1.1	1.2	1.3	1.4	1.5	1.6	1.7	1.8	1.9	2.0
# of logs	17	40	50	14	26	29	-	25	20	25	20
Mean [kg/m^3]	1186	1124	1103	1029	1075	1104	-	1170	1165	1136	1150
Std. Dev [%]	1.19	5.80	1.42	2.98	1.94	1.69	-	1.77	1.29	0.45	0.83

Table 4.1: Number of logs, mean density and standard deviation of the first batch after nailing.

When the flume experiment had to be performed (four months after the settling experiment was nailed) the non-nailed logs were not at the desired density of 1100 kg/m^3. Therefor these logs were also hammered with nails and are referred to as the second batch. Different nails had to be used for the second batch than were used for the first batch because of different saturation rates between the first batch with nails and second batch without nails. Exact cause for this is not investigated. Likely cause is the separation of two groups in

different containers with different water refreshing frequencies. The water of the first batch was refreshed almost daily because they were used for the settling experiment, while the water from the second batch before nailing was refreshed roughly weekly.

Figure 4.8 shows the measured densities of the second batch logs without nails and their respective densities with nails compared to the measured densities of the first batch. No matching nail for log diameter 1.7 cm was found. This is the only log diameter that will be tested in the flume experiment with a natural density.

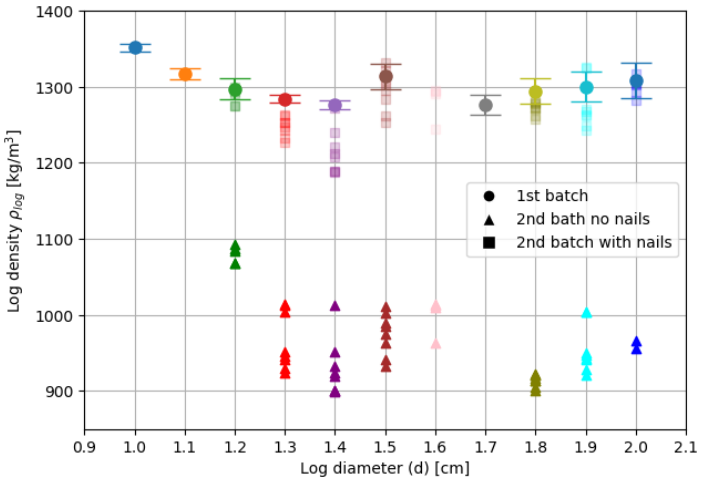

Figure 4.8: Density measurements of the second batch before and after nailing. First batch with nails given as mean with one standard deviation.

4.4. Maximum achieved densities

Here the maximum achieved density for the logs used to research the saturation process and the logs used for the experiments (first and second batch) are evaluated.

As mentioned in section 4.1 the control group reached a density of 1068 kg/m^3 after eight months. 95% of the maximum density was reached 54 days after the logs were first submerged on October 4^{th} 2018. The last 5% was reached in the following seven months. A very slow saturation rate of 0.08 ρ_{log}/day was still present after eight months. It is possible that these logs eventually reach a density of 1100 kg/m^3 but this is not verified in this thesis. The log cut in 2 cm pieces reached a maximum density of 1116 kg/m^3, figure 4.9. Within one month the centre pieces caught up with the edge pieces. This shows how dominant the length of the log affects the saturation rate. After three months the maximum density was practically achieved. After eight months no significant difference in density is observed and differences are mostly related to measuring inaccuracies. The assumption that the logs would saturate in 2-3 months is therefor not entirely incorrect. The expected density of 1100 kg/m^3 or more for the control group was incorrect instead.

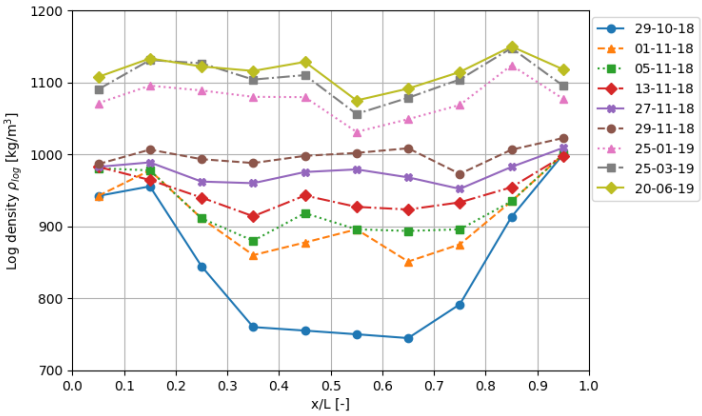

Figure 4.9: Density measurements of 2 cm log pieces without bark over a period of 8 months

The final measured densities for the logs used in the settling and flume experiments are given in table 4.2 and figure 4.10. Maximum densities of 1228-1414 kg/m^3 were reached. Most of the gained density was reached in the first three months, just like the control group. Note that between February 27th 2019 and March 3th 2019 the second batch was added to the first batch. This explains the sudden drop in mean density on March 3th 2019 except for log diameter 2.0 cm where the second batch increased the overall density. The last three months do no show any significant increase in density apart from log diameters 1.8 and 1.9 cm. For log diameter 1.6 cm no measurements were done up to March 3th 2019 because they were not present in the first batch, same for log diameter 1.7 cm on March 3th 2019 and May 23th 2019 but for the second batch. For the last measurement on June 20th 2019 the 1.7 cm logs from the first batch were used as well as the logs without nails. The latter shown in figure 4.10 by a single point ('x'). These logs achieved a mean density of 1025 kg/m^3.

d [cm]	1.0	1.1	1.2	1.3	1.4	1.5	1.6	1.7	1.8	1.9	2.0
Mean [kg/m^3]	1343	1308	1289	1228	1241	1283	1313	1293	1353	1341	1414
Std. Dev [%]	1.03	1.49	1.13	0.75	1.12	0.84	0.33	0.99	0.93	1.09	1.56

Table 4.2: Maximum reached densities and standard deviation of the first and second batch combined

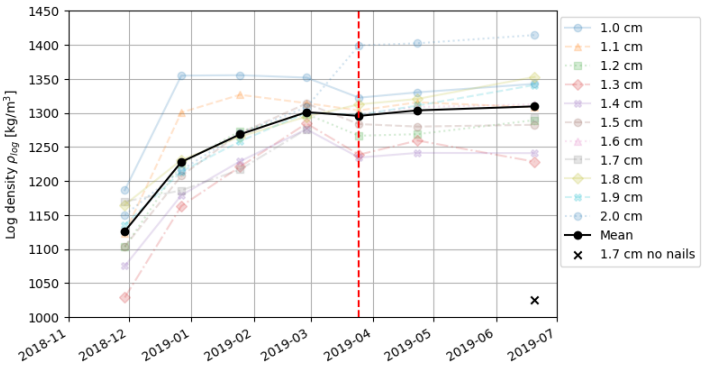

Figure 4.10: Mean density of each log diameter with nails. The red dotted line indicates when the second batch was added to the first batch.

The true density of the logs is the density without the nails. We can calculate what the density of the logs is without the extra weight from the nails, see table 4.3. None of the true densities of the logs is larger than 1100 kg/m^3.

It remains unclear if the logs (willow twigs) would ever reach densities of 1100 kg/m^3. In this research only the 2 cm pieces achieved this density by natural saturation. This could indicate that the logs from the first and second batch were not fully saturated at the end of this research. A reason for this can be the method of saturation. The saturation of the logs was achieved through natural water pressure only, generated by the water depth in which the logs were submerged. The water depths were not regulated. Greatly increasing the water pressure could increase the density further. One method to achieve this is by using a diaphragm vacuum pump (Spänhoff, 2007). The maximum density can then be achieved within minutes. This method was not applied in this research due to budget limitations.

d [cm]	ρ_{log} [kg/m^3]	$m_{nail,avg}$ [g]	true ρ_{log} [kg/m^3]
1.0	1343	2.374	1040
1.1	1308	2.547	1040
1.2	1289	2.534	1064
1.3	1228	3.497	965
1.4	1241	4.115	974
1.5	1283	5.655	963
1.6	1313	5.655	1031
1.7	1293	8.171	933
1.8	1353	9.097	995
1.9	1341	9.097	1020
2.0	1414	12.995	1001

Table 4.3: True log densities without nails reached after correcting for the weight of the nails

5

Settling behaviour of logs

This chapter discusses the results from the settling experiment. Section 5.1 discusses the settling velocity measurements. The settling behaviour of the four drop methods is discussed in section 5.2. The Magnus effect is discussed in section 5.3. The last section discusses the construction of the stability layer (section 3.3.2) of the log filters based on the results from the settling experiment.

5.1. Settling velocity

From video recordings the settling velocity (w_s) is measured. The timestamp (t_i) for each 5 cm of settled distance is recorded, see figure 5.1. The settling velocity is then calculated:

$$w_s = \frac{0.05}{t_i - t_{i-1}} \qquad \text{i from 1 to 7} \tag{5.1}$$

Each log diameter is dropped horizontally oriented 10 times from 15 cm above the water surface in 46.5 cm deep standing water. Visual observations showed that when logs hit the water they decelerate. After this period of deceleration the log accelerates until it reaches terminal settling velocity. The period in which the log decelerates is ignored in the measurements so the influence of wave reflection from the walls can be neglected. This meant that from z = 35 cm a measurement was started. Consequently seven measurements for each drop were possible (at z = 30, 25, 20, 15, 10, 5 and 0 cm). These averaged measurements are shown in figure 5.2 for all log diameters. Figures for each individual log diameter can be found in appendix K.

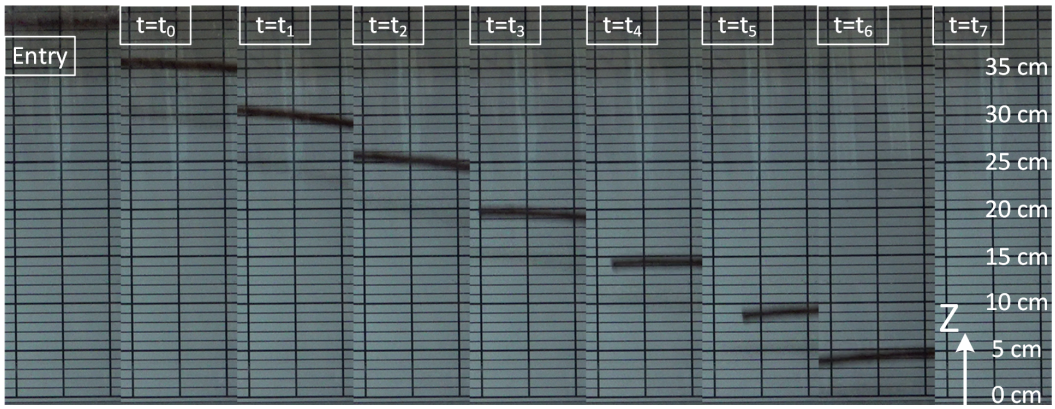

Figure 5.1: Example of settling velocity measurement. End of deceleration due to impact at t=t_0

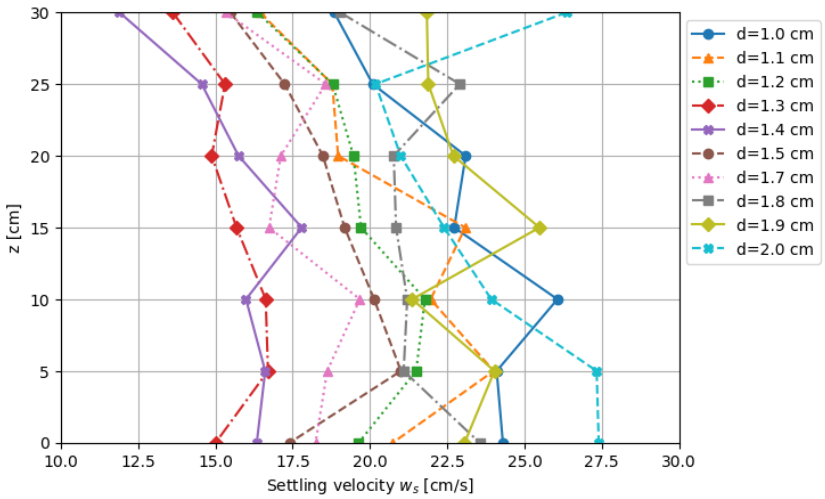

Figure 5.2: Average settling velocities of each log diameter for all seven measurements

d [cm]	$\overline{w_{s,z=15cm}}$ [m/s]	$\overline{w_{s,z=10cm}}$ [m/s]	$\overline{w_{s,z=5cm}}$ [m/s]	$\overline{w_{s,z=0cm}}$ [m/s]	$w_{s,m}$ [m/s]
1.0	0.227	0.261	0.241	0.243	0.243
1.1	0.231	0.220	0.240	0.207	0.225
1.2	0.197	0.218	0.215	0.196	0.207
1.3	0.157	0.166	0.167	0.150	0.160
1.4	0.178	0.160	0.166	0.163	0.167
1.5	0.192	0.201	0.210	0.174	0.194
1.6	-	-	-	-	-
1.7	0.183	0.172	0.204	0.173	0.183
1.8	0.208	0.212	0.211	0.236	0.217
1.9	0.255	0.234	0.240	0.231	0.235
2.0	0.224	0.239	0.273	0.274	0.253

Table 5.1: Settling velocity measurements for the last four data points. For log diameter 1.9 cm only nine logs were measured.

From figure 5.2 it is confirmed that the log accelerates after it decelerated from impacting the water surfacer. The last four measurements show the most constant settling velocities. These four measurements are used to obtain the terminal settling velocity. The mean of the ten drops of these last four measurements ($\overline{w_{s,z}}$) are given in table 5.1. The last column ($w_{s,m}$) is the mean settling velocity over the last four measurements.

Calculating the settling Reynolds number (Re_s=$\mathcal{O}(10^3)$) showed that the logs settle in the turbulent regime. For this reason only Newton's settling velocity for cylinders (equation 2.24) is required for comparison of the measurements with the theory. Because the logs settled in a confined water column a correction for the wall effect is applied to the measurements. Calculations of the settling Reynolds number and wall effect can be found in in appendix L.

Table 5.2 summarises the measured, corrected and Newton's settling velocities. For the small log diameters the measurement correspond well with equation 2.24. For log diameters 1.3 cm to 1.9 cm large differences, larger than 10%, are observed. Measured velocities are smaller than equation 2.24 suggests. Applying the correction for wall effect does not have a positive effect on the results. Settling velocities are smaller after correction, increasing differences. The differences in measured and theoretical settling velocities can be related to three aspects: density, water depth and the measurement setup.

- Calculation of Newton's settling velocity are done with the mean log densities. Variations in the density of logs effect the measured settling velocities. For example, if the mean density is 1100 kg/m^3 for a log diameter but the ten logs used have a mean density of 1150 kg/m^3 the measured settling velocity will be larger than the theoretic settling velocity. Vice versa for ten logs with a mean density of 1050 kg/m^3.

d [cm]	$w_{s,m}$ [m/s]	Eq: 2.24 [m/s]	Difference (%)	$w_{s,m}/w_{s,\infty}$ [-]	$w_{s,\infty}$ [m/s]	Difference (%)
1.0	0.243	0.243	+ 0.01	1.108	0.220	- 7.17
1.1	0.225	0.228	- 1.72	1.092	0.206	- 7.73
1.2	0.207	0.209	- 1.20	1.079	0.192	- 6.36
1.3	0.160	0.173	- 7.48	1.068	0.150	-11.61
1.4	0.167	0.199	-16.37	1.058	0.158	-19.56
1.5	0.194	0.227	-14.24	1.050	0.185	-17.03
1.6	-	-	-	-	-	-
1.7	0.183	0.247	-25.98	1.037	0.177	-27.70
1.8	0.217	0.273	-20.63	1.032	0.210	-22.16
1.9	0.235	0.266	-11.68	1.027	0.229	-13.08
2.0	0.253	0.277	- 8.86	1.023	0.247	-10.01
		Mean	-10.81			-14.24
		Standard deviation	8.23			6.79

Table 5.2: Corrected measured settling velocities compared to Newton's method for non-spherical particles.

The effect of density could explain minor differences in measured and theoretic settling velocities. It does not explain large differences found for log diameters 1.7 and 1.8 cm. This is shown in figure 5.3.

- The time it takes an object to reach terminal settling velocity is affected by the mass of the object and the cross sectional area (balance between gravity force and drag force). A heavier object with equal cross sectional area and shape will take longer to reach terminal settling velocity. This requires a longer distance (here: water depth).

- Measurements are done with a video recording. This is not ideal because the line of sight from camera lens to object and background are different. This means that a measurement where an object passes a line that is situated in the background is inaccurate. This is shown in figure 5.4. During measurements this is taken into account as much as possible.

The settling velocity measurements showed that Newton's method, modified for logs, is most accurate. Application of the modified equation (equation 2.24) was most accurate for small log diameters. For large log diameters smaller settling velocities than Newton's equation suggests are measured. On average the settling velocities are 16% smaller. Likely cause for this is insufficient water depth. The larger logs have more mass and therefor take longer to reach terminal settling velocity. A correction for wall effect decreased accuracy.

The first large difference outside one standard deviation is observed for log diameter 1.4 cm. These logs have a mean mass of 35 grams, or 791 kg on prototype scale. Logs heavier than 791 kg will in practice reach 84% of the terminal settling velocity on average. This is important to consider when dumping logs in rivers where a current has influence on the distribution and settling location of the logs.

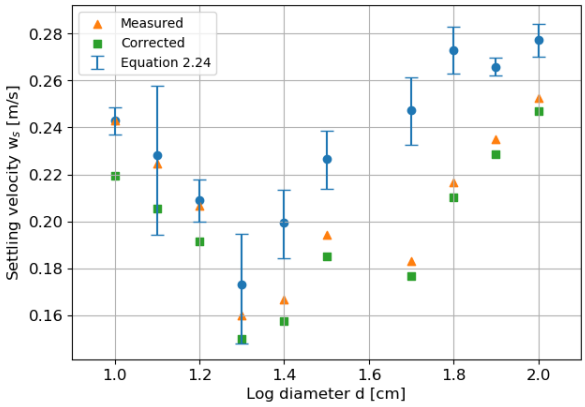

Figure 5.3: Measured and corrected settling velocities ($w_{s,m}$ and $w_{s,\infty}$ respectively) compared to Newton's settling velocity (included ± 1 std. dev. of w_s due log density variation.

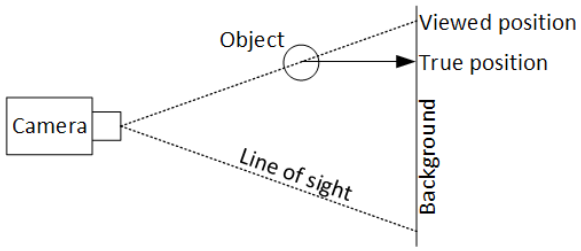

Figure 5.4: Effect of camera line of sight on the viewed position of an object compared to a background.

5.2. Release mechanisms

In this section the results of the four drop methods as described in section 3.2 and table 3.2 are discussed. Manual release experiments HMS, HMT and VMT are compared in terms of the distribution of the logs on the bed. The hatch experiment (HHB) and funnel experiment (HFB) are compared with each other and with the HMT experiment.

In section 5.2.1 only the first ten dropped logs from experiments HMT and VMT are used for the analysis. In section 5.2.2 all the dropped logs from experiments HMT are used for the analysis.

5.2.1. Manual release of logs

Experiments HMS, HMT and VMT were done on December 18^{th} to 21^{st} 2018. Linearly interpolated densities between November 29^{th} 2018 and December 27^{th} 2018 are used for calculations and analysis. The densities are given in table 5.3 and shown in figure 5.5 with their standard deviation.

d [cm]	1.0	1.1	1.2	1.3	1.4	1.5	1.6	1.7	1.8	1.9	2.0
$\rho_{log,HMS}$	1301	1244	1186	1120	1146	1178	-	1182	1212	1191	1197
$\rho_{log,HMT}$	1307	1250	1195	1130	1153	1182	-	1182	1214	1194	1200
$\rho_{log,VMT}$	1313	1256	1195	1130	1153	1182	-	1183	1217	1197	1201

Table 5.3: Mean log densities [kg/m^3] for experiments HMS, HMT and VMT

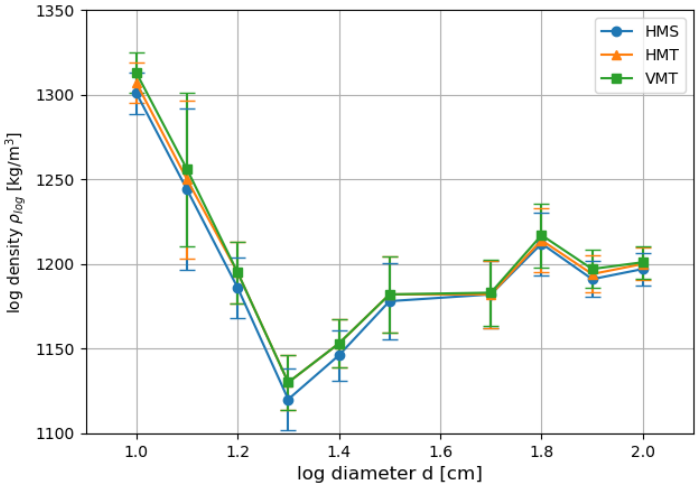

Figure 5.5: Mean log densities with 1 standard deviation for experiments HMS, HMT and VMT

For each type of manual release ten logs were dropped, one by one. After the ten logs are dropped the centre of each log is determined. A circle is drawn with a radius equal to the furthest distance found. An example of this is shown in figure 5.6. All figures can be found in appendix M. The spread of logs dropped in experiments HMS and HMT is a lot less than for experiment VMT. This is directly related to the release mechanism. Logs naturally settle in a horizontal orientation. A log that enters the water vertically oriented will want to rotate to a horizontal orientation. This causes the log to settle away from the drop location. This

was not always observed for the VMT experiments, likely due to insufficient water depth. The cause of the many different orientations is related to how the logs hit the bed. Most logs hit the bed vertically, sometimes bounce a little and then fall over. This is illustrated in figure 5.7a.

The difference between HMS and HMT experiments is less noticeable. In general logs in the HMT experiments show a larger spread than the HMS experiments despite the logs being dropped one by one. The cause for this are collisions. When a settling log collides with a settled log either or both of the logs will roll away from each other, see figure 5.7b. This can cause logs to roll further away from the drop location.

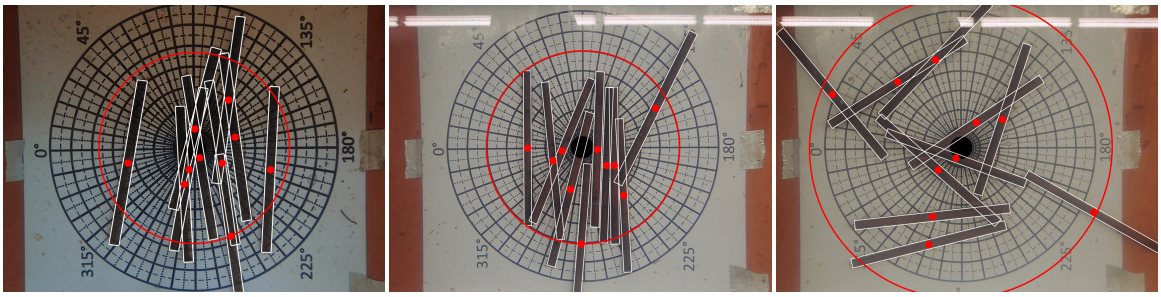

(a) HMS12 (b) HMT12 (c) VMT12

Figure 5.6: Results for experiments HMS12, HMT12 and VMT12

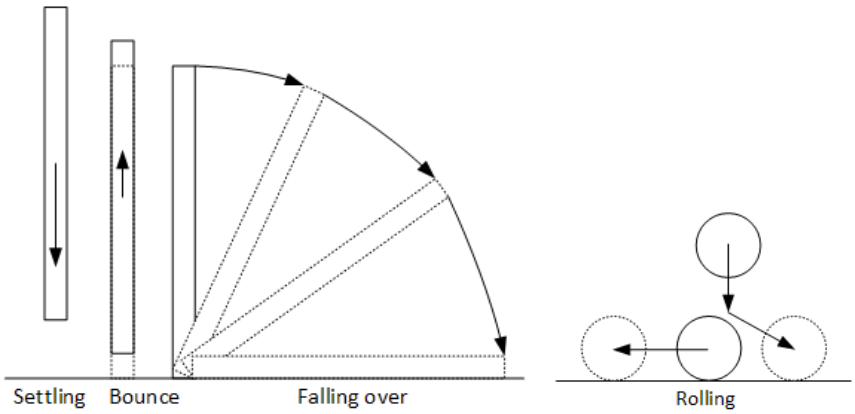

(a) Falling over (b) Rolling on the bed

Figure 5.7: Falling over and rolling of logs found in manual release experiments

Heavier logs settle faster and are less sensitive to external forces such as pressure differences due to surface waves. For example, the same happens when we drop a bowling ball and a feather in air at the same location. The bowling ball is much more likely to land right below the drop location, whereas the feather is easily affected by wind and drag. The mean and maximum distance (in log diameters) of the HMS, HMT and VMT experiments are plotted versus the log mass per unit length in figure 5.8. Indeed the mean and maximum distance decreases as the log mass increases can be observed. The mean and maximum distances are given in number of logs diameters. This means that for a logs with equal weight and length but different diameters, the log with the larger diameter will have a larger spread. Logs with a larger diameter experience more drag and are more likely to collide.

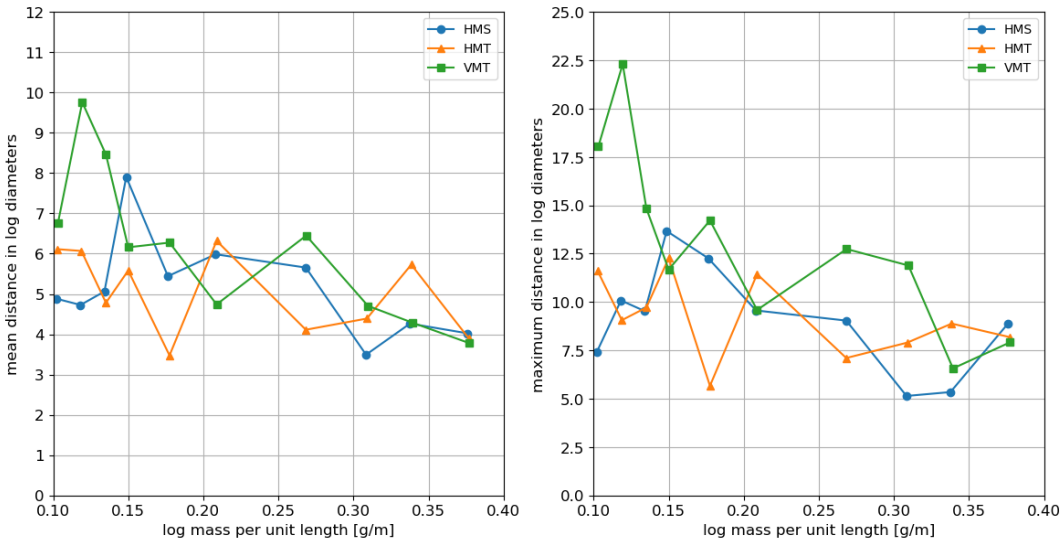

Figure 5.8: Mean (left) and maximum (right) distance in number of log diameters vs. log mass per unit length

A side view of both stacking orientations (horizontal and vertical) also shows that dropping logs horizontally creates a denser structure, see figure 5.9. Here 40 logs were dropped one by one. A denser structure is beneficial to the filter function. A denser (but open) filter has smaller pores, reducing flow velocities inside the structure. Turbulent eddies inside the structure are smaller, reducing pressures and shear stresses. This increases the local stability of the log filter and the sand underneath. A tighter packed log filter is also smoother on the surface. This reduces the shear stresses acting on the top layer of the log filter, increasing global stability.

Figure 5.9: Difference in stacking behaviour (Top) Horizontally dropped (Bottom) Vertically dropped.

5.2.2. Horizontal distribution of bulk

Experiments HHB (hatch) and HFB (funnel) were done on January 7^{th} and 8^{th} 2019, respectively. Linearly interpolated densities between December 12^{th} 2018 and January 1^{th} 2019 are used for calculations and analysis. The densities are given in table 5.4 and shown in figure 5.10. No standard deviations were known on January 5^{th} 2019 and are therefor not included in the figure.

d [cm]	1.0	1.1	1.2	1.3	1.4	1.5	1.6	1.7	1.8	1.9	2.0
$\rho_{log,HMT}$	1307	1250	1195	1130	1153	1182	-	1182	1214	1194	1200
$\rho_{log,HHB}$	1355	1310	1243	1185	1198	1231	-	1198	1244	1231	1236
$\rho_{log,HFB}$	1355	1311	1245	1187	1200	1233	-	1199	1245	1232	1238

Table 5.4: Mean log densities [kg/m^3] for experiments HMT, HHB and HFB

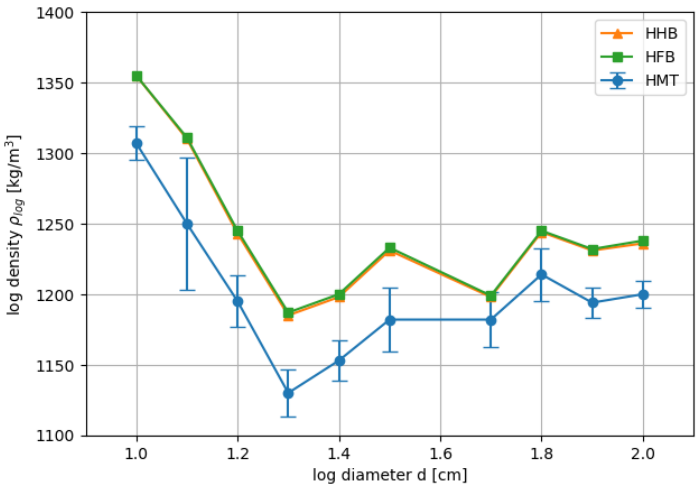

Figure 5.10: Mean log densities for experiments HMT, HHB and HFB

The HMT experiments are used again in this section. In the previous section only the first ten dropped logs were used. To compare stacking of logs droppbed one by one with the hatch and funnel mechanisms the HMT experiment was extended. All the logs from the first batch were used, see table 5.5. Logs were dropped in sets of 10 for the hatch mechanism. If less than 10 logs were left for experiments HMT and HHB they were also dropped.

d [cm]	1.0	1.1	1.2	1.3	1.4	1.5	1.6	1.7	1.8	1.9	2.0
HHB	10	4x10	4x10	10+4	2x10+6	2x10+9	-	2x10+5	2x10	2x10+5	2x10
HMT & HFB	17	40	50	14	26	29	-	25	20	25	20

Table 5.5: Number of logs used for the (extended) HMT, HHB and HFB experiments

Hatch mechanism

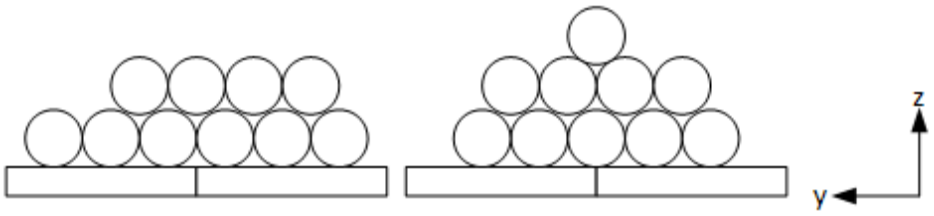

Figure 5.11: (Left) scheme for log diameters 1.0-1.4 cm (Right) scheme for log diameters 1.5-2.0 cm

The logs were placed on top of the hatch in a pyramid shape, shown in figure 5.11. The logs dropped from a height of 5.6 cm in 46.5 cm deep standing water. In figure 5.12 the results for experiments HMT12 and HHB12 are shown. For all figures see appendix N. The hatch experiments generally show a wider spread of logs in y-direction and more logs have rotated. In x-direction no significant difference is observed.

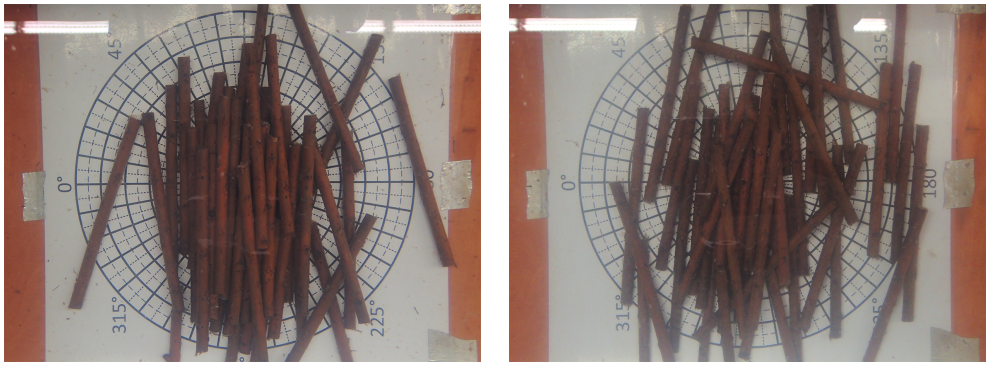

(a) HMT12 (b) HHB12

Figure 5.12: Stacking of 40 (4x10) logs for experiments HMT12 and HHB12

The wider spread is related to angular velocities of logs and rolling on the bed, see figure 5.13. In this figure ten logs of log diameter 1.4 cm are dropped using the hatch mechanism. In approximately 2.5 seconds the logs reach the bed, but it takes another 3.5 seconds before all the logs have stopped rolling on the bed. In these 3.5 seconds it was observed that due to wave reflections at the surface, orbital motions are present in the water column and near the bed. These orbital motions have an effect on the behaviour of the logs during settling and when rolling on the bed. The effect is not quantified in these experiments but the effect for logs on the bed is assumed to be negligible small compared to the rolling effect.

Subsequent drops of logs after the first set generally do not spread wider than the first set. The logs settle between the first logs. The logs present on the bed act as a blockade to rolling logs. With increasing amount of logs on the bed this effect is enhanced. Logs that do settle further than the logs that are already on the bed are likely rotated. The different orientation causes the log to be 'pushed' away as it collides with other logs. Because multiple layers are created no reliable distances could be obtained from these experiments as was done in the previous section.

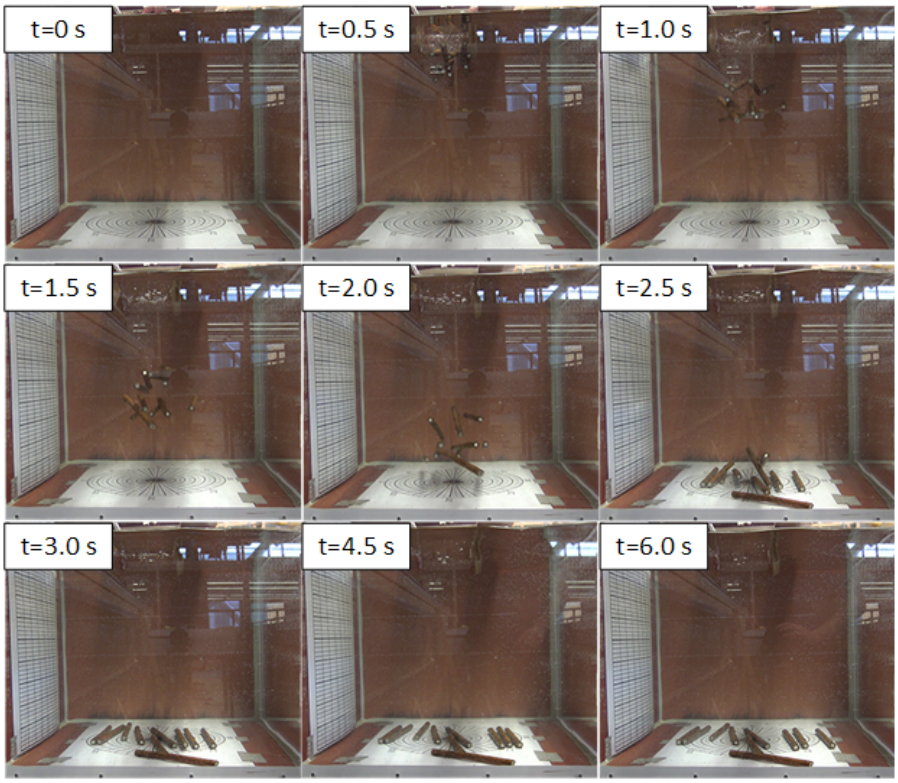

Figure 5.13: Time series of ten logs of log diameter 1.4 cm settling using the hatch mechanism

No difference in how the logs stack has been observed between the HMT and HHB experiments. Only one case stands out, see figure 5.14. In this figure a side view of experiments HMT18 and HHB18 are shown. Twenty logs were dropped in both experiments. Two logs are clearly raised above the rest of the logs in the bottom image (experiment HHB18). These logs can cause settling logs to rotate horizontally and/or vertically as well as act as a slope along which the settling logs can settle. If this occurs a less dense structure is created. However it is also possible that a next drop will cause these logs to be pushed down or rolled away by collisions. It is not known under what circumstances either scenario occurs.

Figure 5.14: Two types of stacking behaviour (Top) Only horizontal stacking (Bottom) Occasional vertical stacking

Funnel mechanism

All available logs from the first batch were used for the funnel mechanism. For each log diameter the experiment was done thrice. One test of experiments HFB10 and HFB12 are shown in figure 5.15. All figures can be found in appendix O. For log diameter 1.0 cm the logs appear to settle in a ring around the drop location. For log diameter 1.2 cm a very wide spread in y-direction is found. A lot of logs have settled far away from the drop location. Some even reached the walls of the tank.

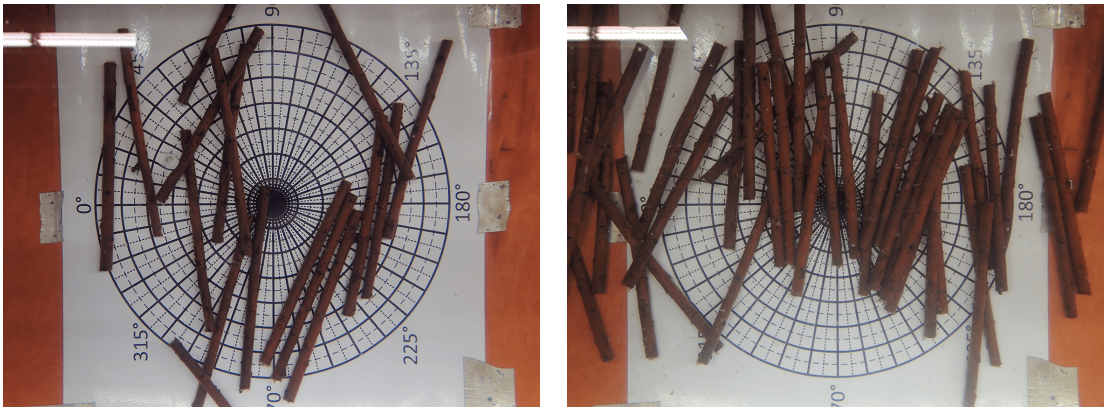

(a) One test of experiment HFB10

(b) One test of experiment HFB12

Figure 5.15: Two different type of results (a) Logs settle in a ring around the centre (b) Logs settle like a strip

Figure 5.16 shows a time series of one test from experiment HFB12. A total of 40 logs was dropped for log diameter 1.2 cm. The funnel mechanism allows continuous stream of logs that enter the water. When the first logs enter the water the following logs push these logs aside, forming a U-shape. The orbital motion of the surface wave holds some of the logs closer to the surface because the surface is moving upwards. Secondly the orbital motion pushed some inwards. When the wave 'reverses' the downwards motion pushes the logs that were left behind down. The last logs that entered catch up with the first logs because they enter the water with higher velocities. This causes a lot of collisions between logs high up in the water column. As the logs settle and collide they spread and the outer logs rotate. The first logs that reach the bed are the last logs to

enter the water. The first logs that entered the water are pushed to the outside and settle further away from the drop location.

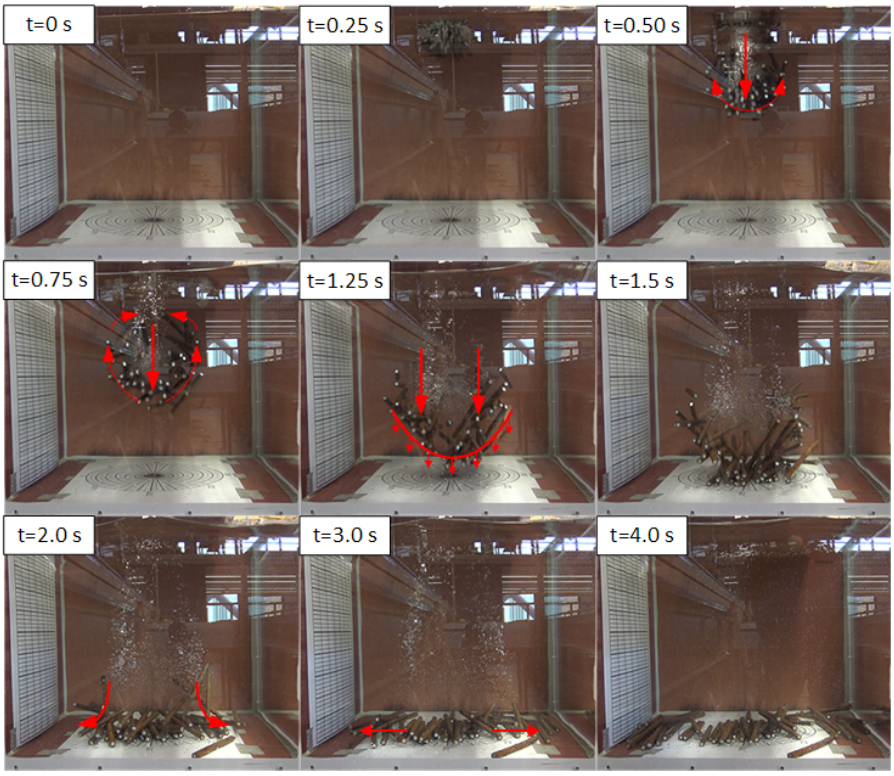

Figure 5.16: Time series of 40 logs of log diameter 1.2 cm settling using the funnel mechanism

For each experiment the centre of the logs have been determined and a 95% confidence interval ellipsoid is calculated. Figure 5.17 shows the three tests of experiments HFB10 and HFB12. All figures can be found in appendix P. For most of the experiments the ellipsoid extends beyond the figures in y-direction, meaning the spread is actually larger than 50 cm. In x-direction the spread averages around 30 cm.

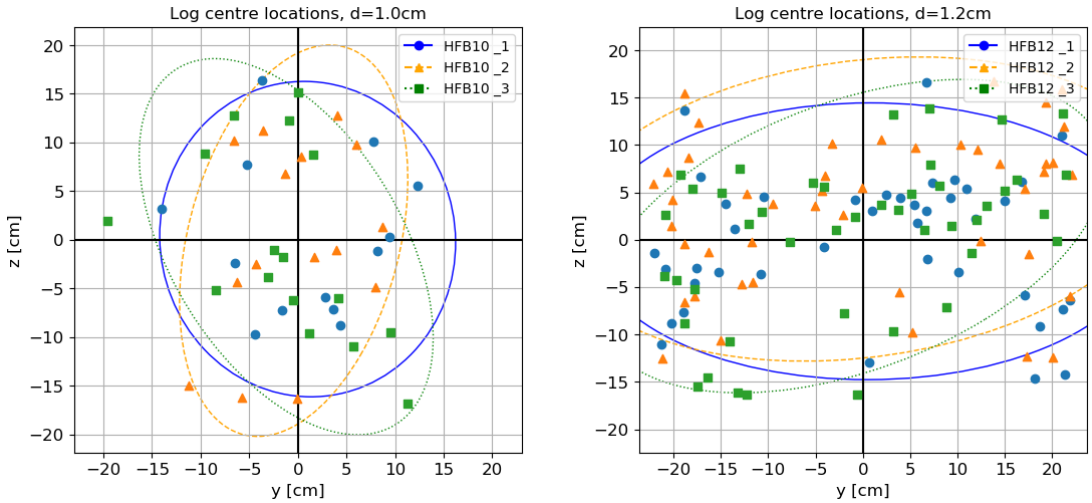

(a) Log diameter 1.0 cm

(b) Log diameter 1.2 cm

Figure 5.17: 95% confidence interval ellipses for experiments HFB10 and HFB12

Due to the wide spread in y-direction and relatively small spread in x-direction the funnel mechanism is a

suitable option for constructing a bed protection. The mechanism allows large quantities of logs to be placed as strips. In this thesis a spread of 1.5 times the log length was found. Consequently when constructing a log bed protection strokes should have a spacing of 1.5 times the log length. This creates an overlap that is large enough for logs to settle independently of the strokes next to it but small enough to not create large trenches between strokes. When extending the stroke in length the spacing should have minimal overlap. This guarantees that one layer is constructed at a time. From the HFB experiments the spread in y-direction suggests a spacing of 2-2.5 log lengths.

5.3. Magnus effect

The slope experiment was done on 10-01-2019. Linearly interpolated densities between 27-12-2018 and 25-01-2019 are used for the analysis. The densities are given in table 5.6 and shown in figure 5.18 with their standard deviation.

d [cm]	1.0	1.1	1.2	1.3	1.4	1.5	1.6	1.7	1.8	1.9	2.0
$\rho_{log,HSM}$	1355	1313	1248	1191	1203	1238	-	1201	1247	1235	1242

Table 5.6: Mean log densities [kg/m^3] for experiment HSM

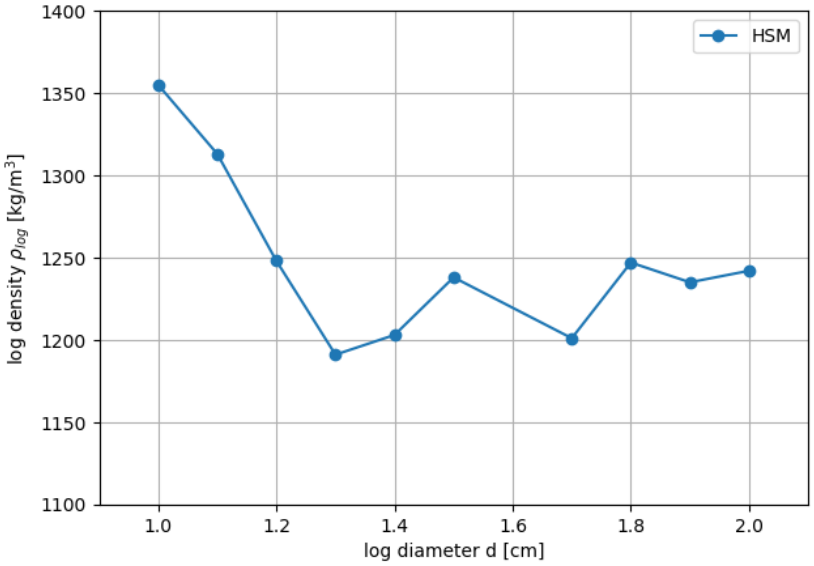

Figure 5.18: Mean log densities for experiment HSM

Logs were released at the top of a 20 cm long slope, angled 15 degrees with the horizontal axis. The bottom of the slope was positioned 7.5 cm above the water surface. For each log diameter ten logs were dropped. Using a video camera the first 20 cm of settling was recorded. Four types of settling were observed: drifting, stalling, changing direction and changing orientation. The four types are shown in figure 5.19.

- Drifting: When the log enters the water the Magnus force immediately generates a horizontal acceleration. As the velocity increases so does the Magnus force. Because of this the initial path of the log is mostly linear. As the log looses angular velocity due to friction the Magnus force decreases. The vertical acceleration becomes larger than the horizontal acceleration and the log starts to settling more vertically.
- Stalling: When the log enters the water the Magnus force is briefly dominant over the gravitational force. This causes the log to 'stall' in the water column for just a moment. Afterwards the log shows a parabolic path.
- Changing direction: When the log enters the water the angular velocity is small and friction quickly dissipates the rotation. The gravitational force is dominant over the Magnus force. When the angular

velocity is completely lost the log wants to settle in the most streamlined orientation. For a crooked shaped cylinder this orientation can cause the log to rotate in the opposite direction, reversing the horizontal velocity. This can happen a few times as the log finds the most streamlined orientation.

- Changing orientation: When the log enters the water one end of the log settles further, orienting the log more vertically. The Magnus force on both ends is directed in opposite directions, enlarging the vertical orientation of the log. As the drag starts to decrease (due to the vertical orientation) and thus the log starts to settle the Magnus force at both ends of the log will be in the same direction.

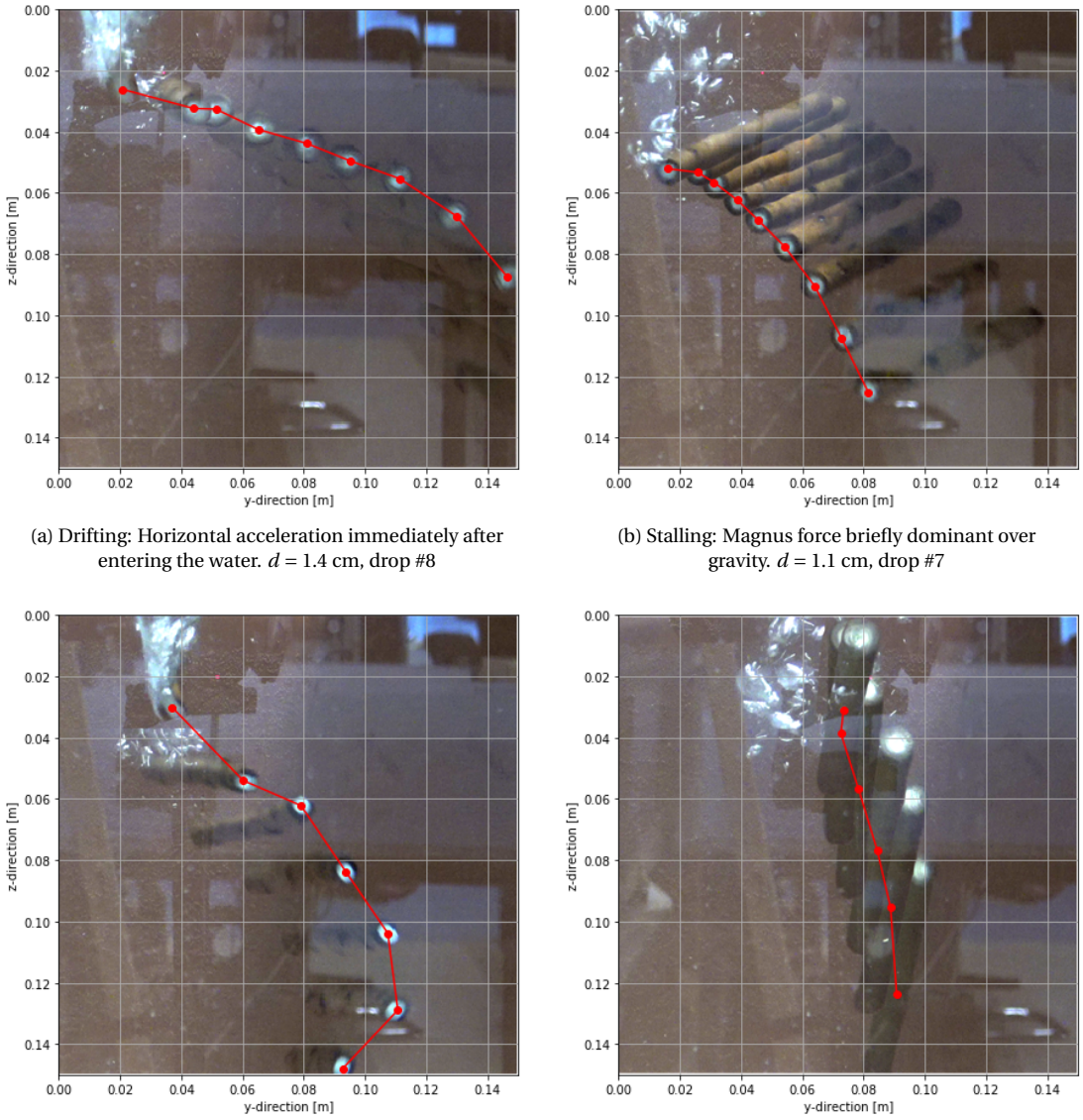

(a) Drifting: Horizontal acceleration immediately after entering the water. d = 1.4 cm, drop #8

(b) Stalling: Magnus force briefly dominant over gravity. d = 1.1 cm, drop #7

(c) Changing direction : Magnus force is lost as angular velocity is dissipated. d = 1.0 cm, drop #1

(d) Changing orientation: Magnus force enlarges initial vertical orientation (no horizontal acceleration). d = 1.4 cm, drop #9

Figure 5.19: Four types of settling found in experiment HSM for logs experiencing the Magnus force

5.4. Construction of the stability layer

The stability layer of the log filters are constructed using the funnel mechanism, see section 3.2.1. One stroke is constructed from multiple drops. The spacing of drops was researched in section 5.2.2. The spacing in x-direction was 2-2.5 times the log length (40-50 cm) and in y-direction 1.5 times the log length (25 cm). The

water depth in the flume is 1/3 the water depth in the tank. This requires a different spacing in x-direction than what is found in section 5.2.2. Secondly the number of logs that could be used for creating the bed protection was limited to approximately 100 for each experiment (table 3.1.

The spacing for the experiments RO18, SP18, SP16, SP14, SP17 and BP14, figure 5.20 was set to 30 cm. Five drops were needed, consisting of 20 logs, to create the stability layer. This combination allowed some overlapping to create a more smooth layer. The outside two drops were spaced slightly different. For the drop at x=65 cm the location was shifted 5 cm downstream (from x=60 to x=65 cm) so the settling logs would not collide with the mesh covering the first 50 cm of the test section. For the same reason the drop at x=180 cm was positioned 20 cm upstream of the false bed.

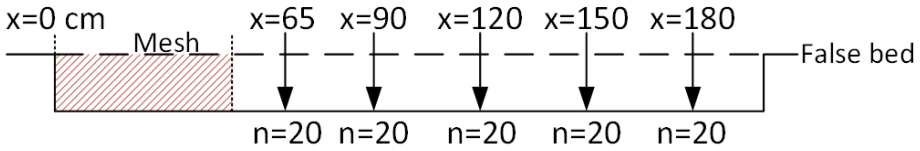

Figure 5.20: Spacing and number of logs used for constructing the stability layer for experiments RO18, SP18, SP16, SP14, P17 and BP14

The spacing and number of logs for experiments SR18a, SR18b and SR18c were all different, see figures 5.21 to 5.23. Initially a wide spacing with a large number of logs was used, figure 5.21. The spacing was set to 1.5 times the log length (30 cm) plus an extra 5 cm to minimise overlap because logs settle end-to-end. Logs settling end-to-end with insufficient spacing creates less dense and rougher layers, reducing stability, see figure 5.24. In experiment SR18b an extra drop was added in between the first two drops but with less logs, figure 5.22. Experiment SR18a showed that the spacing could be reduced to about 25 cm. This was applied in experiment SR18c where a spacing of 25 cm was used, figure 5.23.

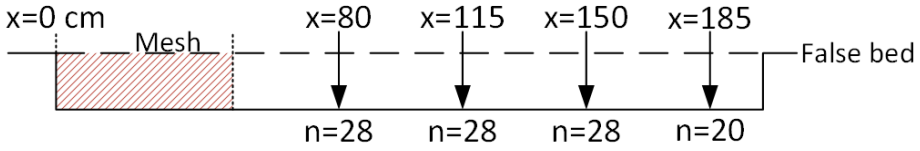

Figure 5.21: Spacing and number of logs for constructing the stability layer for experiments SR18a

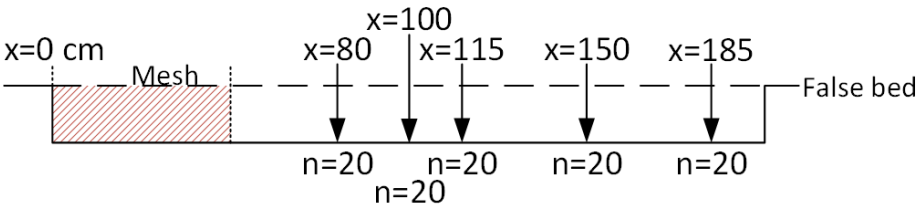

Figure 5.22: Spacing and number of logs for constructing the stability layer for experiments SR18b

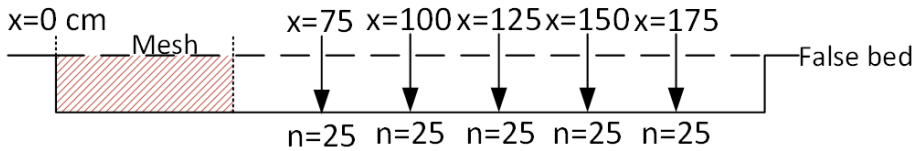

Figure 5.23: Spacing and number of logs for constructing the stability layer for experiments SR18c

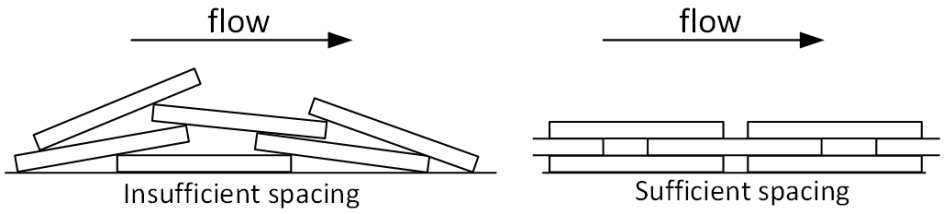

Figure 5.24: Effect of spacing on end-to end settling of logs

For experiment CP15 the construction of the stability layer had similar spacing as the SP and BP14 experiments but the number of logs was increased because the dropped logs now have a grading, see figure 5.25. The grading increased the total number of logs that could be used to construct the log filter. This is also required because the mean log diameter is 1.5 cm and 20 logs is not enough to create an entire strip with enough thickness. Each drop consists of 30 logs and is made up of 3 logs from each diameter except 1.7 cm. The last drop consists of 20 logs because when dropping 30 logs there were collisions with the false bed.

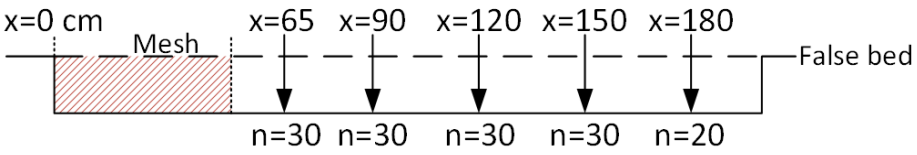

Figure 5.25: Spacing and number of logs for constructing the stability layer for experiment CP15

6

Roughness of a log filter

In this chapter the results from the roughness experiments in the flume are presented and discussed. After the ADV data is filtered the flow over the log filter is analysed. The goal was to find a correlation between the roughness of the log filter and the zero velocity level (z_0). A function is found that links the log diameter to z_0.

A total of seven experiments are done. The stability layers of the experiments are constructed as described in section 5.4. For each experiment the velocity profile above the filter is measured for two to four discharges. Table 6.1 summarises all experiments.

Exp.	d [cm]	h [cm]	Q [l/s]				Note
RP18a	1.8	14	2.07	4.61	11.20	14.92	For Q=11.20 l/s the velocity profile was measured at three locations
RP18b	1.8	14	2.07	2.79	14.38	17.62	
RP18c	1.8	14	2.79	7.98	12.97	16.81	
SP16a	1.6	14	2.67	7.23			
SP14c	1.4	14	4.36	8.82			
SP17c	1.7	14	2.75	6.19			
CP15c	1.5	14	7.14	12.27			Mixed log diameters, mean 1.5cm

Table 6.1: All tests for which the velocity profile was measured

6.1. ADV Measurements

The flow velocities are measured at location 3 (figure 3.9 and table 3.3), 165 cm from the start of the test section. When the flow reaches the test section it should be fully adjusted to the bottom roughness of the log filter. It is important to verify if the flow at the start of the test section is equal to the flow at the end of the test section. If this is the case the shear velocity is uniform along the log filter. The shear velocity is crucial for the Shields stability analysis, see equation 2.20. For experiment RO18a, Q=11.20 l/s, the velocity profile is measured at three locations: x=85, 125 and 165 cm. The velocity profiles are shown in figure 6.1.

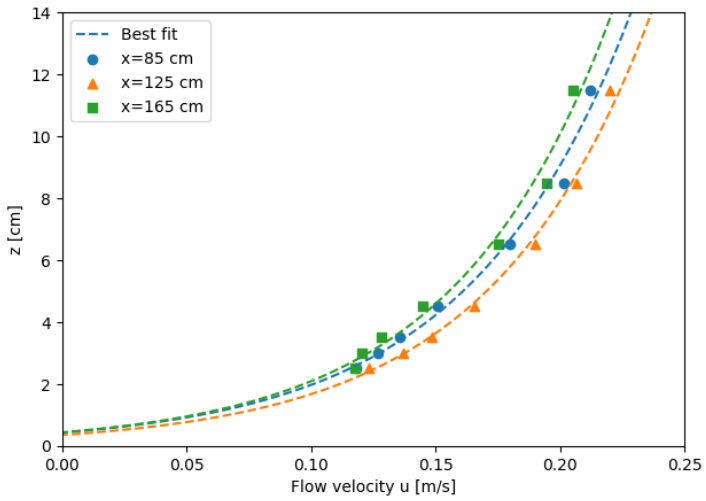

Figure 6.1: Velocity profiles measured at three locations for experiment R018a, Q=11.20 l/s.

The shear velocity at respectively x=85, 125 and 165 cm was 0.02686, 0.02637 and 0.02605 m/s. The maximum difference is negligibly small (3%). We can assume that the shear velocity measured at x=165 cm acts across the entire test section.

Before the velocity profiles can be analysed the ADV measurements are processed. Each ADV measurement is filtered for all three directions (x, y and z) separately using the phase-space threshold method described in section 3.4.2. The total number of spikes replaced after filtering are computed as a percentage of the total number of data points. Figure 6.2 shows a histogram of the percentages for each direction. The highest percentage found is 12.15% and occurred only once. For the roughness analysis we are mainly interested in the mean flow velocities and less in the turbulent characteristics. For this reason 12.15% is considered acceptable and all measurements can be used for the roughness analysis.

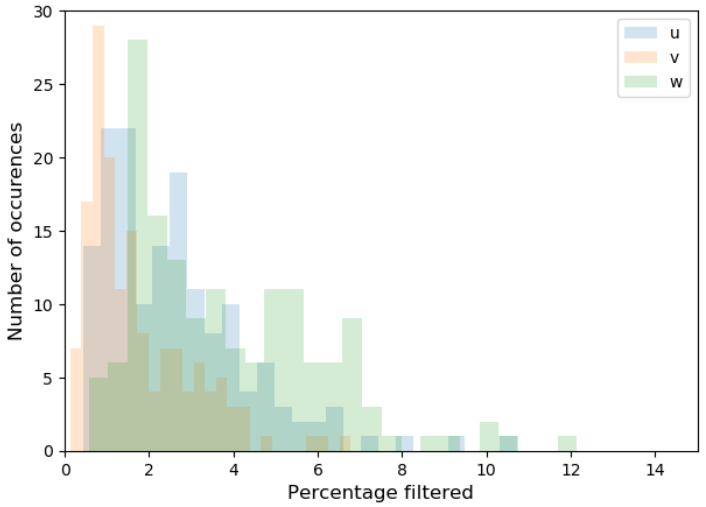

Figure 6.2: Histogram of the percentage filtered

6.2. Flow above a log filter

Analysis of the flow above a log filter is done in five stages. First the 2D scans of the log filter profiles are analysed to obtain the mean and standard deviation of the filter height, figure 6.3. The velocity profile (section 2.2.2) is fitted to the data points. The equation of the velocity profile is repeated below, equation 6.1. The fitted parameters are z_0 and u_*. This is the reference fit. Equation 6.1 is modified (equation 6.2) to take the mean height of the log filter (h_{filter}) w.r.t. the hydraulic plane (z=0) into account. The modified equation is fit to the data points. From these two fits the zero velocity level (z_0) as a function of log diameter and profile variation

(standard deviation of the filter height, σ_{filter}) are determined. Using the obtained function(s) for z_0 a last fit is done for equations 6.1 and 6.2.

$$u = \frac{u_*}{\kappa} \ln\left(\frac{z}{z_0}\right) \tag{6.1}$$

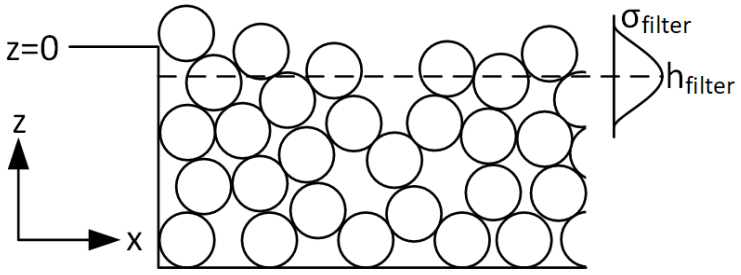

Figure 6.3: Visualisation of parameter definitions used for filter roughness analysis

6.2.1. 2D scan of a log filter

A total of seven profiles were scanned of which one is shown in figure 6.4. The rectangular area surrounded with a red dashed line is the area taken into account for h_{filter} and σ_{filter}. The reason for this is explained below. All eight 2D scans can be found in appendix Q. Table 6.2 summarises the results.

Due to the method that is used to scan the filter profile and post-process the data the 2D map appears distorted. The starting x-coordinate for a pass was not always the same as the end x-coordinate of the previous pass. This means that for each pass the x-coordinates are slightly shifted. For determining the mean and standard deviation of the filter profile this discrepancy can be neglected.

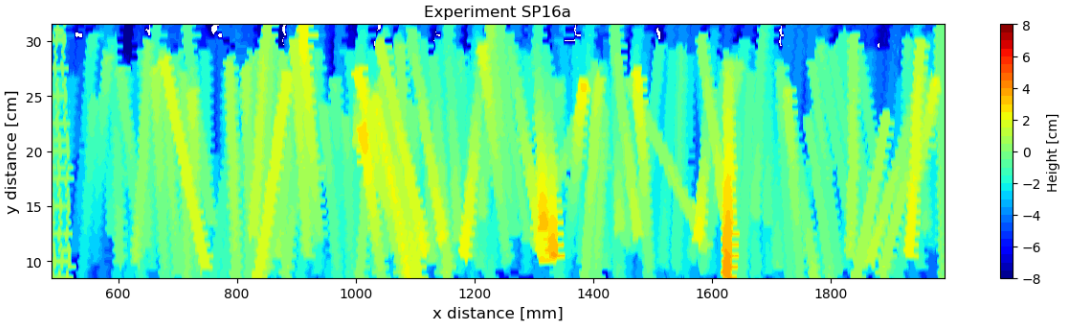

Figure 6.4: 2D scan for profile SP16a

Exp.	d [cm]	h_{filter} [cm]	σ_{filter} [cm]
RP18a	1.8	-1.596	0.595
RP18b	1.8	-1.915	0.590
RP18c	1.8	-1.933	0.567
SP16a	1.6	-0.694	0.746
SP14c	1.4	-1.591	0.491
SP17c	1.7	-1.340	0.432
CP15c	1.5	-0.799	0.543

Table 6.2: Properties of the profiles used for the roughness analysis

Because only one strip of logs is representing the log filter it is important to check what the sensitivity is of h_{filter} and σ_{filter} on how much of the 2D scan is taken into account. From both ends 5 cm is ignored to remove the influence of the mesh and false bottom. The width of the 2D scan taken into account is the centre

20 cm (equal to the log length). The sensitivity of the width on h_{filter} and σ_{filter} is shown in figure 6.5. Both h_{filter} and σ_{filter} appear to flatten for small widths. This is a consequence of narrowing the 2D scan up to the point where the width is (very) small compared to spread of the logs in y-direction. In other words, the 2D scan becomes 1D (independent of the y-direction). The horizontal location and orientation of the log no longer has an effect on h_{filter} and σ_{filter}. This is visualised in figure 6.6.

In practice, if a scan is made of a large area containing a large number of strips it is not required to narrow the area to obtain the mean and standard deviation. The influence of gaps in the filter and trenches between strips is negligible in this case.

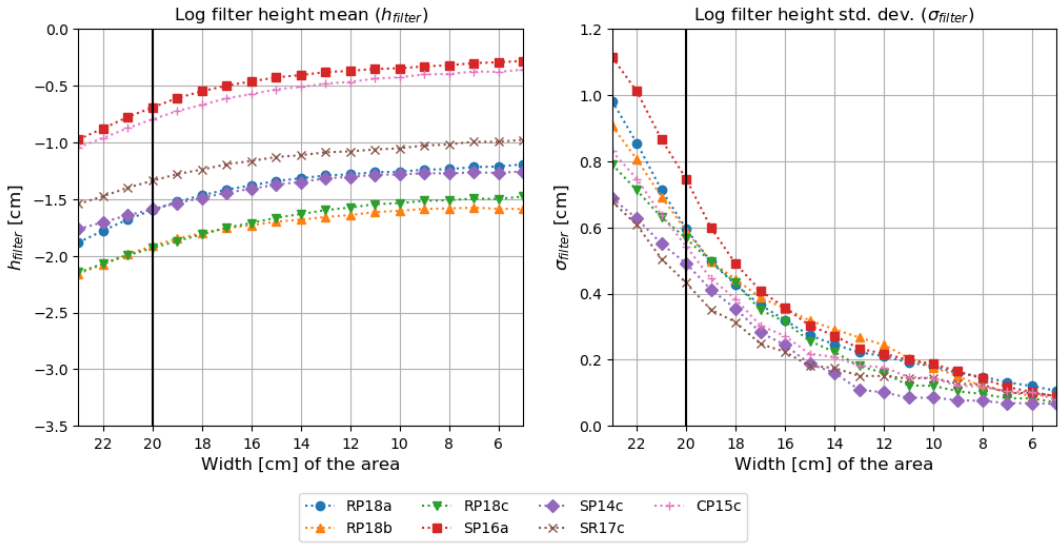

Figure 6.5: h_{filter} and σ_{filter} vs. the width of the 2D scan. The intersections with the black vertical line are used in this thesis and given in table 6.2

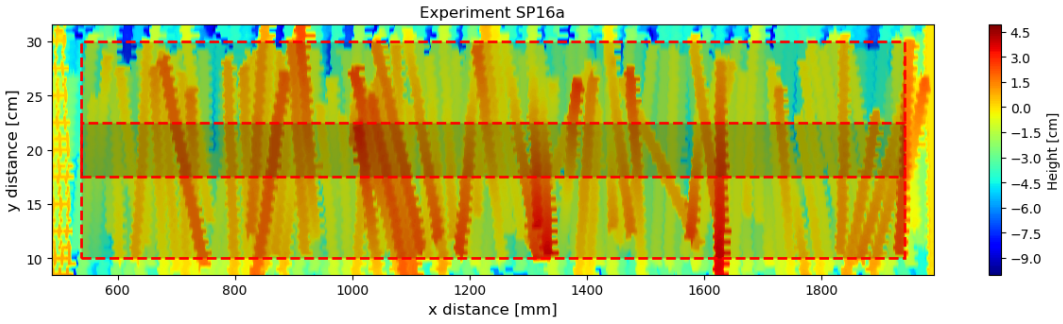

Figure 6.6: (Outside region) Area for width=20 cm (Inside region) Area for width=5 cm

6.2.2. Reference fit

A best fit of equation 6.1 is done for the data points to create a reference fit. For profile RP18a the best fit is given in figure 6.7a. The fit is accurate but not all four lines go through the same point for u=0 m/s, the zero velocity level (z_0). This is because z_0 is fitted and not yet a property of the log filter. To confirm that equation 6.1 is valid for the flow in the flume all results (20 measurements) are plotted on a semi-logarithmic scale in figure 6.7b. If the equation is valid the data points should be on a linear line going through the origin. This can be quantified by computing the Pearson Correlation Coefficient (PCC, or r_{pcc}). A r_{pcc}-value close to 1 means good correlation. The r_{pcc}-value for the data in figure 6.7b is 0.9935, and thus equation 6.1 is valid for the experiments. This also confirms that the flow is in the turbulent regime and not the transitional or laminar regime. This means that we can expect z_0 to be a linear function of the log filter roughness.

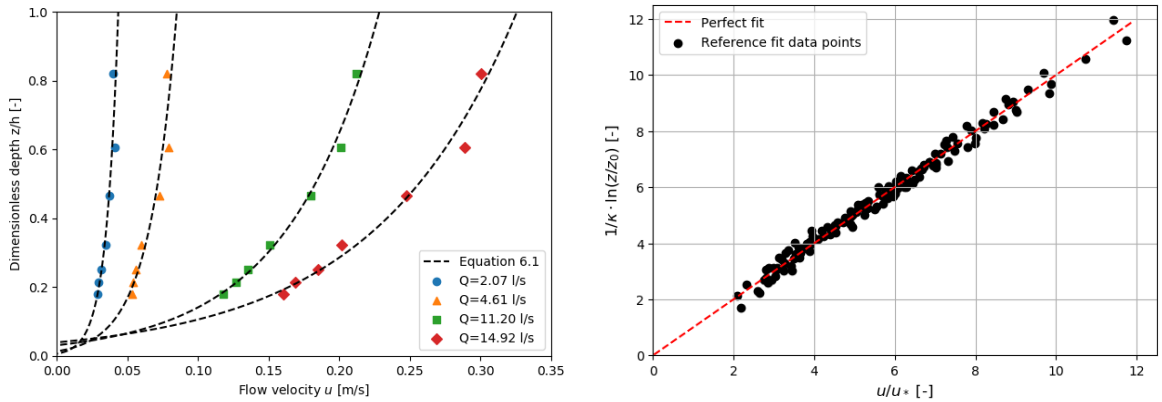

(a) Velocity profile fit for experiment RP18a for all four discharges

(b) Semi-logarithmic scale plot of all 20 measurements

Figure 6.7: (a) Best fit lines for experiment RP18a (b) Semi-logarithmic plot for all data points

Expected is that for each experiment z_0 is constant because it is independent of the flow and a property of the log filter and u_* increases linearly with discharge (i.e. flow velocity). The fitted parameters (z_0 and u_*) are plotted against the discharge in figure 6.8. Globally, z_0 is increasing with the discharge but the correlation is very weak (r_{pcc}=0.2493). The accuracy of the position of the ADV and the flow depth are of the same order as z_0 (millimetres). This means that slight differences in the true z-location of the ADV can have a significant impact on the z_0 value. The correlation for the shear velocity u_* is good (r_{pcc}=0.9724). The fit for shear velocity is more dependent on the flow near a z-location rather than the z-location itself. The linear regression of u_* does not go through the origin but the difference is small.

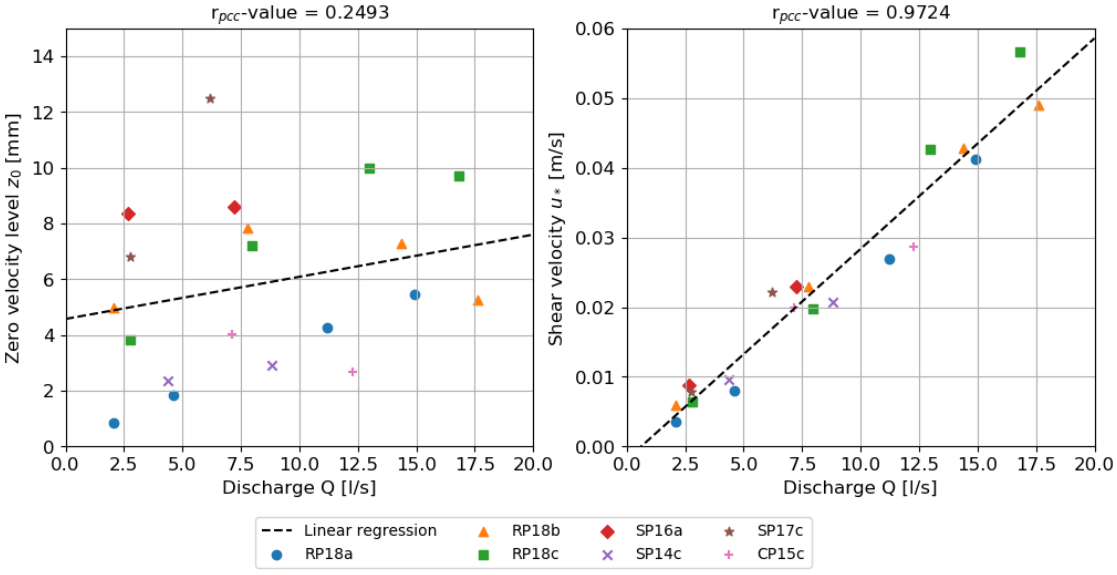

Figure 6.8: Fitted z_0 and u_* with linear regression

6.2.3. Adjustment for filter height

For a rock filter the hydraulic bed ($z = 0$) is usually set to the top of the bed, see section 2.2. For log filters this is not yet known. Several approaches are possible for defining z=0. In this thesis simply the log filter mean heights (h_{filter}) found in section 6.2.1 are used. We can modify equation 6.1 to take the mean height of the log filter into account, see equation 6.2. Equation 6.2 is fitted to the data points. The results are compared with the reference in figure 6.9.

$$u = \frac{u_*}{\kappa} \ln\left(\frac{z - h_{filter}}{z_0}\right) \tag{6.2}$$

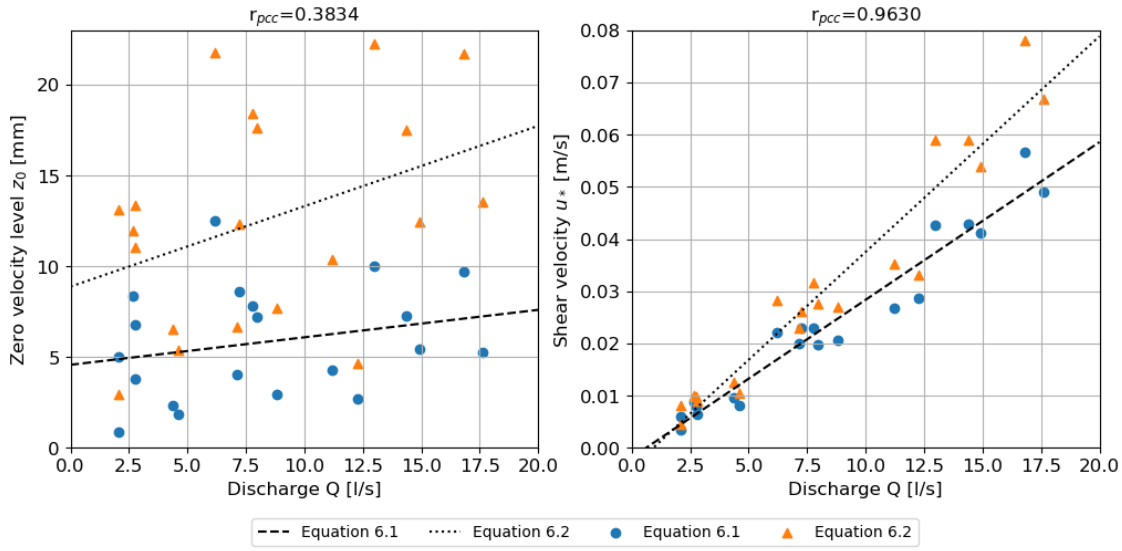

Figure 6.9: Fit using equation 6.2 compared to the reference (Best fit)

Both z_0 and u_* have increased compared to the reference. This is not surprising. Lowering the hydraulic bed will a require larger z_0 to compensate for $u_{z=z_0} = 0$. However this also requires the shear velocity to increase. The cause for this is that when z/z_0 decreases, so does u/u_*.

The correlation between Q and z_0 is still very weak (r_{pcc}=0.3834). Also the slope of the linear regression for equation 6.2 is three times larger than the slope of the linear regression for the reference. This means that for higher discharges differences in z_0 are amplified more and the accuracy of the z-locations of the measurements becomes more dominant. Figure 6.10 shows the effect of the modification to the velocity profile.

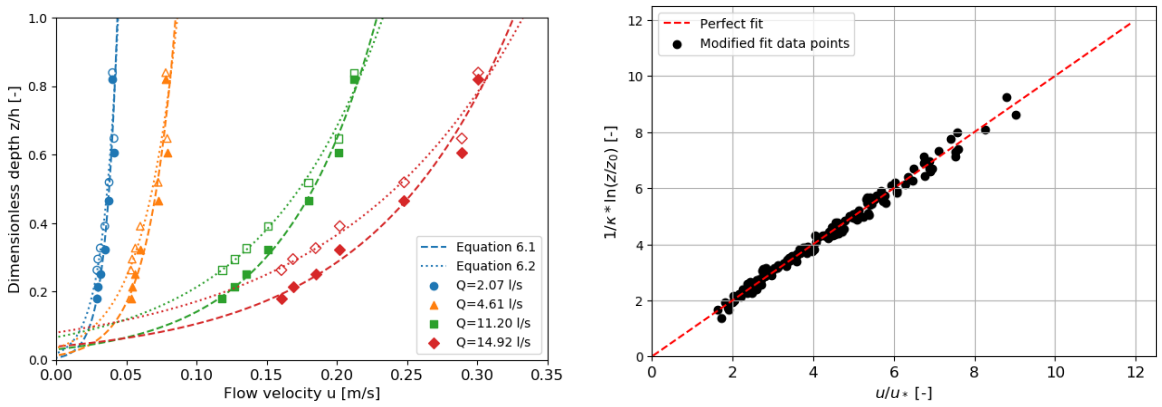

(a) Effect of equation 6.2 on the velocity profile

(b) Semi-logarithmic plot of all 20 measurements

Figure 6.10: (a) Difference in fit between equations 6.1 and 6.2. Open markers are the data points using equation 6.2 (b) Semi-logarithmic plot of all data points using equation 6.2

6.2.4. Function for zero velocity level

From the previous fits the z_0 values can be used to try and find the zero velocity level as a function of log filter diameter or variation. For rock z_0 is a function of the Nikuradse roughness coefficient k_r which is usually one or two rock diameters, see section 2.2.3. For logs the same approach is considered where k_r=d, and a slight alteration where k_r=σ_{filter}. These approaches result in the following two equations:

$$z_0 = c_1 \cdot d + p_1 \tag{6.3}$$

$$z_0 = c_2 \cdot \sigma_{filter} + p_2 \tag{6.4}$$

- c_1, c_2 Fitted slope
- p_1, p_2 Fitted intersection

The zero velocity level has a mean and standard deviation for each log diameter (d) and filter variation (σ_{filter}), see appendix R. For z_0 in equations 6.3 and 6.4 the mean are used. Figure 6.11 shows z_0 compared to the log diameter and profile variation. The linear regression shows that z_0 can be a linear function of the log diameter and is mainly independent of the filter variation.

A second linear regression was done for z_0 as a function of the log diameter. The intercept of the function was constrained to go through the origin (p_1=0), see figure 6.12. This is done because for an infinitely small diameter the roughness becomes negligible. The regression lines for the constrained function are less steep and at the same time less correlated with the data. The latter is a consequence of there being no clear correlation between log diameter and standard deviation in the measured profiles, see table 6.2. The values for parameters c_i and p_i are given in table 6.3.

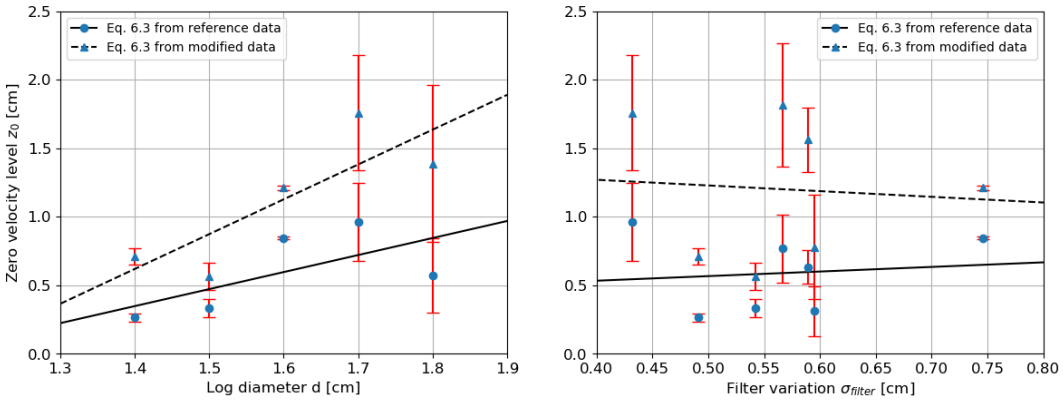

Figure 6.11: Zero velocity level linear regression for equations 6.3 and 6.4 (unconstrained)

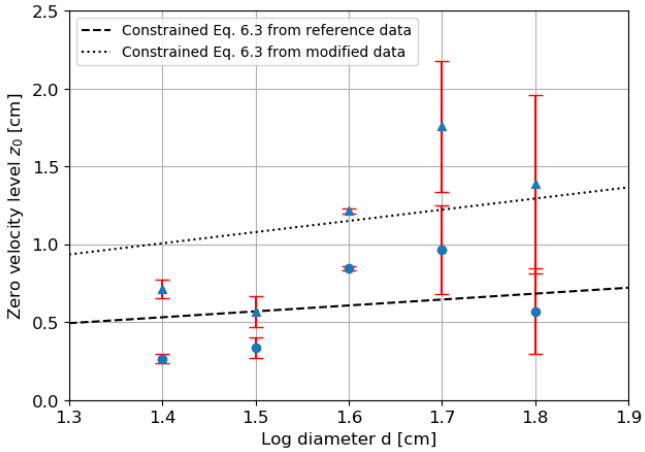

Figure 6.12: Linear regression of equation 6.3 with p_1=0 (constrained)

Parameter	Unconstrained		Constrained	
	Reference	Modified	Reference	Modified
c_1 [-]	1.24	2.54	0.38	0.72
c_2 [-]	0.34	-0.41	N.A.	N.A.
p_1 [cm]	-1.39	-2.94	0	0
p_2 [cm]	0.40	1.44	N.A.	N.A.

Table 6.3: Statistics of the linear regression for z_0

We will continue with only equation 6.3 with both the unconstrained and constrained fitted parameters. Implementing the parameters we obtain the following equations for z_0 as a function of the log diameter:

$$\textbf{Equation 6.1 with:} \quad z_0[m] = \begin{cases} 1.24d - 0.0139, & \text{Unconstrained} \\ 0.38d, & \text{Constrained} \end{cases} \tag{6.5}$$

$$\textbf{Equation 6.2 with:} \quad z_0[m] = \begin{cases} 2.54d - 0.0294, & \text{Unconstrained} \\ 0.72d, & \text{Constrained} \end{cases} \tag{6.6}$$

The above four equations can be used directly in equations 6.1 and 6.2, respectively. The only parameter that is now unknown is the shear velocity (u_*). A last fit is done to examine the change in u_* when using equations 6.5 and 6.6 for the zero velocity level. The obtained fits are shown in figure 6.13. As previously noticed the modified equation (equation 6.2) overestimates the shear velocity, see table 6.4. The unconstrained functions for z_0 are quite accurate with the reference fit. The deviation of is less than 5.5%. The constrained functions deviate a lot more, up to 15%. For determining the shear velocity at any given discharge during the flume experiments the slope of the linear regression for the best fit of equation 6.1 is used. This lead to the following equation:

$$f(u_*(Q)) : u_* = 2.858 \cdot 10^{-3} Q \tag{6.7}$$

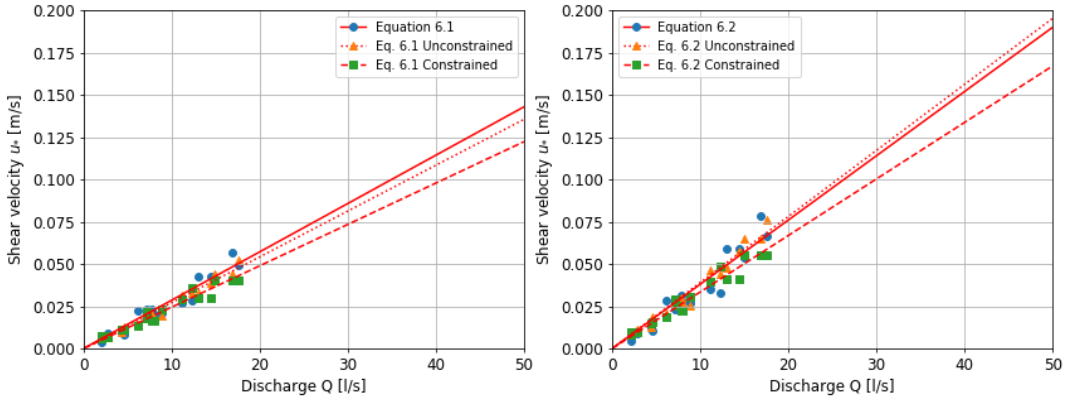

Figure 6.13: Shear velocity as a function of the discharge for equations 6.1 and 6.2 using equations 6.5 and 6.6 for the zero velocity level z_0

Equation	Best fit	Unconstrained	Constrained
Reference (Eq. 6.1)	$2.858{\cdot}10^{-3}$	$2.709{\cdot}10^{-3}$	$2.446{\cdot}10^{-3}$
Modified (Eq. 6.2)	$3.797{\cdot}10^{-3}$	$3.903{\cdot}10^{-3}$	$3.341{\cdot}10^{-3}$

Table 6.4: Slopes of the linear regression for the shear velocity (u_*) as a function of discharge (Q)

6.2.5. Comparison with a rock filter

In the previous sections the roughness of a log filter was analysed. A modified equation was used and an equation for z_0 as a function of the log diameter was found. The modified equation overestimated the shear velocity of the flow because of the relationship between u/u_* and z/z_0. The zero velocity level (z_0) increased and therefor so did the shear velocity u_*.

For rock filters z_0=$k_r/30 \approx d_{n50}/30$. For log filters we found four equations of which two were applicable (equation 6.5). For comparison with rock filters we consider the constrained function from equation 6.5:

$$z_0 \approx d/2.6 \tag{6.8}$$

The unconstrained function of z_0 from equation 6.5 for equation 6.1 resulted in similar results for the shear velocity as a function of the discharge. The constrained function of z_0 from equation 6.5 was less steep and therefor resulted in a 12% underestimation of the shear velocity as a function of the discharge.

The analysis in this chapter is not conclusive on the roughness of a log filter but shows that it is possible to define a relatively accurate function for the zero velocity level. The difference between defining the roughness of a rock and log filter can be related to the differences in geometry. The roughness of a rock filter can be considered uniform. The roughness of a rock filter is independent of the flow direction because a sphere has radial symmetry in all directions. The roughness of a log filter however is dependent on the flow direction. Flow perpendicular to the log length, as analysed in this chapter, experiences a different bottom roughness as a flow across an identical bed but parallel to the log length. Secondly logs can also be angled vertically. One end of the log can be located beneath the top layer of a log filter, while the other end is located above the top layer. The roughness of a log filter is thus expected to be very dependent on the flow direction.

7

Stability of a log filter

In this chapter the results of the stability experiments are presented and discussed. First the stability of Experiment (experiments SP and CP15) with logs perpendicular to the flow are discussed in section 7.1. Experiment SR18, where logs are parallel to the flow, is discussed in section 7.2. The backfilling experiments (BA14) are discussed in section 7.3. Observations of the internal flow during experiments is discussed in section 7.4. The stability layers of the log filters are constructed as described in section 5.4.

The stability of the logs was categorised in four phases, listed below. The first phase (initial motion) describes logs that show a rocking movement (wiggling). The next phase is deformation. Logs are displaced over short distances (order of log diameter) by relocation due rolling or short transport. After relocation the logs remain return to the first phase or show no movement. At the third phase first transport is observed. Logs are transported over distances of the same order as the log length (20 cm) or more. Few logs are transported at once at one ore multiple locations. The last phase is failure. When failure occurs transport of logs is frequent or a chain reaction occurs. One log becomes mobile starting a chain reaction where collisions mobilise other logs.

1. Initial motion — Rocking movement on the spot
2. Deformation — Relocation due to rolling or short transport
3. Transport — First transport over distances of order log length
4. Failure — Transport over several log lengths and/or chain reaction

The discharges at which a phase was observed were recorded and transformed into a shear velocity using equation 6.7. The shear velocity of each phase was used to determine the critical Shields parameter using equation 2.20. All obtained shear velocities can be found in appendix S.

7.1. Logs perpendicular to the flow

SP experiments and experiment CP15 (section 3.3.4) were done between June 29^{th} and July 11^{th} 2019. Log densities are linearly interpolated between measurements from May 23^{th} and July 20^{th} 2019. The log densities for each experiment are given in tables 7.1 and 7.2. In experiment SP17 logs with a diameter of 1.7 cm without nails were used. The density of these logs was measured on July 20^{th} 2019 (section 4.4). The log filters were constructed using the funnel mechanism, see sections 3.2 and 5.2.2. The average critical Shields parameter of each experiment are given in table 7.3, as well as the average critical Shields parameter for each phase. The average Shields parameter of each phase was plotted versus the dimensionless diameter d_* from equation 2.14, see figure 7.1. For experiment CP15 the dimensionless diameter d_*=217 with d=1.5 cm and ρ_{log}=1310 kg/^{3}. The critical Shields parameters for experiment CP15 are given as letters A, B, C and D for respectively phases 1, 2, 3 and 4.

Experiment	d [cm]	Date	ρ_{log} [kg/m^3]	$\sigma_{\rho_{log}}$ [%]	d_* [-]
SP18	June 29th 2019	1.8	1341	1.11	269
SP16	July 3rd 2019	1.6	1311	1.03	232
SP14	July 4th 2019	1.4	1241	2.06	187
SP17	July 6th 2019	1.7	1025*	1.13*	106

Table 7.1: Log densities for experiments SP18, SP16, SP14 and SP17. (*) Density measured on July 20th 2019.

d [cm]	1.0	1.1	1.2	1.3	1.4	1.5	1.6	1.8	1.9	2.0	Avg.
ρ_{log} [kg/m^3]	1341	1309	1286	1233	1241	1282	1312	1348	1336	1412	1310
$\sigma_{\rho_{log}}$ [%]	0.87	1.77	1.93	1.29	2.20	1.35	1.08	1.32	1.52	2.79	3.86

Table 7.2: Log densities for experiment CP15 on July 11th 2019

Experiment	Avg. critical Shields parameter ψ_c [m/s]			
	1. Initial motion	2. Deformation	3. Transport	4. Failure
SP18	0.055	0.093	0.137	0.224
SP16	0.049	0.085	0.141	0.190
SP14	0.041	0.099	0.169	0.240
SP17	0.061	0.089	0.156	0.237
CP15	0.042	0.075	0.137	0.182
Average	0.050	0.088	0.148	0.215

Table 7.3: Average Shields parameters (ψ_c) for experiments SP18, SP16, SP14, SP17 and CP15

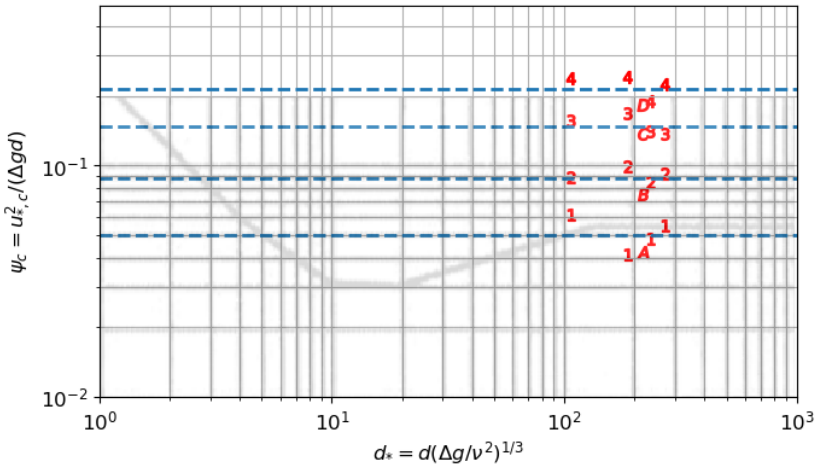

Figure 7.1: ψ_c vs. d_* for experiments SP18, SP16, SP14 and SP17 plotted with the critical Shields curve. Horizontal dashed lines are the averages for each phase.

The results from the stability analysis show that phase 1 (initial motion) correlates well with the critical Shields curve level 5 "*frequent particle movement at all locations*" (figure 2.4). In practice this level (ψ_c=0.055) is regarded as the failure threshold for rock bed protections. Rock bed protections are designed for ψ_c=0.03. Expected was that initial motion of the logs would be observed at a similar critical Shields value. This means that for rock of equal d_* a lot more movement would be present at the same level as where the logs were initially mobilised. In other words, the logs in this research are more stable than rock of equal d_*.

When a rocking motion (phase 1) logs was observed the logs were generally 'alone', meaning that they had no neighbouring logs that would lock it in its place. This is known as the interlocking effect. If initial motion was observed of an interlocking log it would remain in this state for longer than the logs that were alone.

When phase 2 (deformation) was observed the displaced logs would quickly find a new stable position. These positions were primarily located a few log diameters downstream where the log would be sheltered from the flow or near the wall of the flume where the log would settle parallel to the flow. The log filter returns to phase 1. These two types of deformation are shown in figure 7.2.

When a log filter enters phase 3 the logs were transported over short distances of the order of the log length. Logs would settle again similarly to what was found in phase 2. The transported logs collide with the log filter before settling, occasionally leading to another log or logs to be mobilised (chain reaction). These logs would locally cause for deformation or also become transported. The chain reactions are small and short.

Failure of the log filter occurs when a mobilised log like observed in phase 3 would initiate a large chain reaction at the location of mobilisation and/or by collision. An (extreme) example of this was observed in experiment SP16b, shown in figure 7.3.

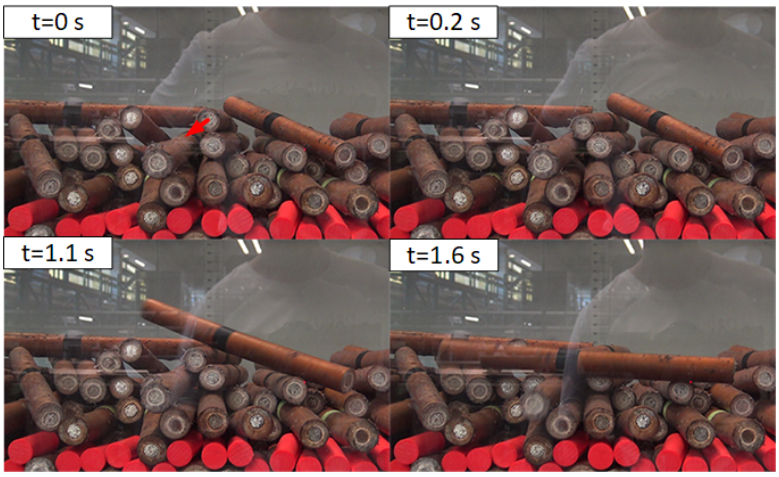

(a) Experiment SP18a: relocation by turning. One log shoots away (red arrow) initiating the deformation

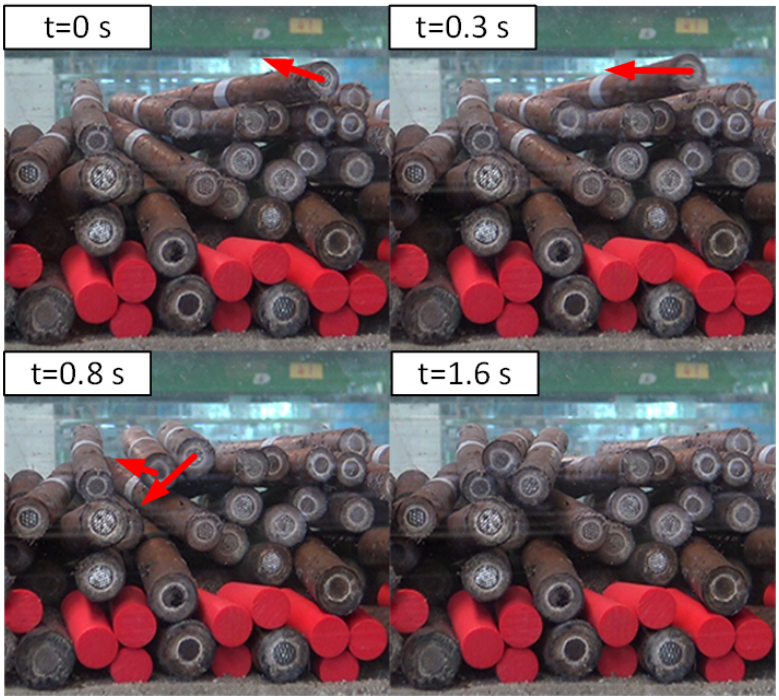

(b) Experiment SP16a: relocation by sheltering. Movement of the logs indicated by the red arrow

Figure 7.2: Deformation and failure phases observed in the flume experiments

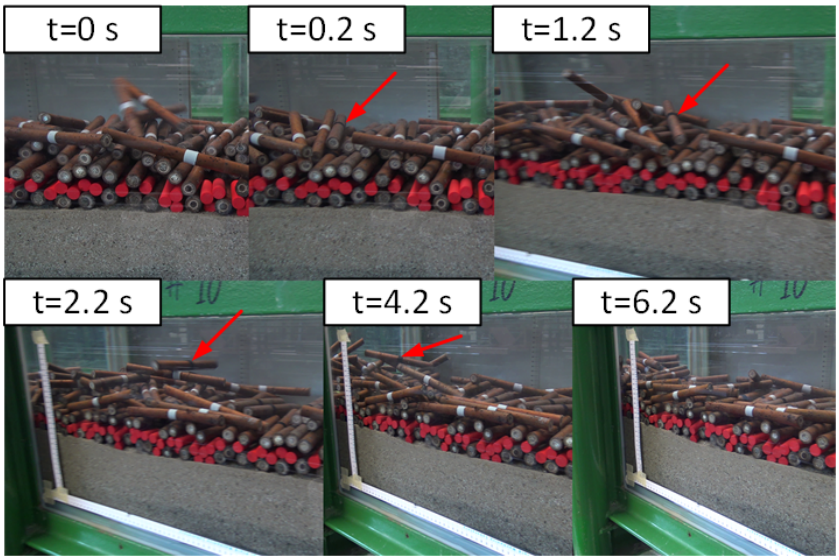

Figure 7.3: Experiment SP16b: failure by chain reaction. The red arrow points to a log from the foundation layer

It is suggested that the main cause for the better stability of a log filter compared to rock filters is the interlocking effect of logs. Due to the cylindrical geometry the centre of mass of a log in a log filter can be located (much) lower than the part exposed to the flow. The flow exerts a force on the exposed part of the log, generating a torque around a turning point. Depending on how much of the log is exposed to the flow the torque can be absorbed by other logs. This adds to the global stability of the log filter. Log that would otherwise be displaced or transported, potentially colliding and destabilising other logs, are kept in place by the interlocking effect.

7.2. Logs parallel to the flow

Experiments SR18a, SR18b and SR18c were done on July $7th$ 2019. Log density is linearly interpolated between measurements from May 23^{th} and July 20^{th} 2019, see table 7.4.

Equation 2.20 is also applied for logs parallel to the flow. It is assumed that the shear velocity acting on the log in parallel orientation is equal to logs perpendicular to the flow for which equation 6.7 was used. This leads to the following critical Shields parameters:

Experiment	d [cm]	Date	ρ_{log} [kg/m^3]	$\sigma_{\rho_{log}}$ [%]	d_* [-]
SR18a	July 7^{th} 2019	1.8	1346	1.26	271
SR18b	July 7^{th} 2019	1.8	1346	1.26	271
SR18c	July 7^{th} 2019	1.8	1346	1.26	271

Table 7.4: Log densities for experiments SR18a, SR18b and SR18c

Experiment	Avg. critical Shields parameter ψ_c [m/s]			
	1. Initial motion	2. Deformation	3. Transport	4. Failure
SR18a	0.042	0.107	0.229	
SR18b	0.066	0.078		
SR18c		0.101	0.175	
Average	0.053	0.095	0.201	
Avg. SP18	0.055	0.093	0.137	0.224

Table 7.5: Average Shields parameters (ψ_c) for experiments SR18a, SR18b, SR18c and SP18

On average the parallel logs had similar stability for phases 1 and 2. However for phase 3 where logs are transported the critical Shields parameter for parallel logs was 50% larger than for perpendicular logs. This is

a direct consequence of the orientation of the logs. Logs parallel to the flow experience lower drag forces and higher friction forces. Consequently the shear stress/velocity required to mobilise a log in parallel orientation has to be larger.

The types of deformations observed for the SR experiments were similar as the ones observed in section 7.1. However, instead of the logs rotating parallel to the flow the logs rotated perpendicular to the flow and settled in the trenches. In these trenches they are sheltered from the flow.

7.3. The effect of backfilling

Experiments BP14a and BP14b were done on July $14th$ 2019. Log density is linearly interpolated between measurements from May 23^{th} and July 20^{th} 2019, see table 7.6. Backfilling of the log filters is done using a funnel that holds 850 ml of sand. The diameter of the opening of the funnel is 1.3 cm. One funnel was used to backfill a 30x20 cm^2 area (length x width) of the log filter. A total of 4.25 litres (5x850) is backfilled, covering the total area (150x20 cm^2) with a 1.4 cm thick layer of sand (1 log diameter). The diameter of the sand was different for the experiments. Experiment BA14a was backfilled with sand with a diameter of 400μm (equal to the sand underneath the log filter) and experiment BA14b with a diameter of 150μm. On prototype scale this is gravel with a diameter of 1.2 and 0.45 cm, respectively. The critical Shields parameters are given in table 7.7.

Experiment	d [cm]	Date	ρ_{log} [kg/m^3]	$\sigma_{\rho_{log}}$ [%]	d_* [-]	d_{sand} [μm]
BP14a	July 11^{th} 2019	1.8	1241	2.20	217	400
BP14b	July 11^{th} 2019	1.8	1241	2.20	217	150

Table 7.6: Log densities for experiments BP14a and BP14b

Experiment	Avg. critical Shields parameter ψ_c [m/s]			
	1. Initial motion	2. Deformation	3. Transport	4. Failure
BP14a	0.045		0.145	0.221
BP14b	0.045		0.178	
Avg. SP14	0.041	0.099	0.169	0.240

Table 7.7: Average Shields parameters (ψ_c) for experiments BP14a and BP14b

The results from the experiments show no significant increase in stability for the log filters. It appeared that the sand did not add to the stability. The sand covering the top layer of the log filter quickly eroded by falling through the log filter pores. Most of the sand was eroded before the logs would naturally start rocking (phase 1). Throughout the experiment the sand continued to erode from the top layers and fall through the pores. In experiment BP14a most of the sand settled around the interface between the foundation layer and the stability layer, see figure 7.4a. In experiment BP14b the sand was able to reach the sand layer underneath the log filter, see figure 7.4b. The foundation layer is overall denser packed than the stability layer. The smaller pore size makes it harder for sand to fall through. Sand with a diameter of 400 μm is also more resistance to turbulence inside the log filter.

(a) Experiment BA14a, d_{sand}=400μm

(b) Experiment BA14b, d_{sand}=150μm

Figure 7.4: Locations of sand at the end of experiments BP14a and BP14b

7.4. Internal flow

The internal flow of a log filter was visualised in experiments SP18c, SP14c and SR18b. The discharge and depth averaged flow velocity when the dye was added are given in table 7.8.

Exp.	Discharge Q [l/s]	$\overline{U}$ [m/s]
SP18c	5.10	0.09
SP14c	18.30	0.33
SR18b	2.75	0.05
	9.76	0.17

Table 7.8: Discharge (Q) and depth averaged flow velocity ($\overline{U}$) when dye was added

The flow observed in figure 7.5 is representative of all four observations. The flow behind a log is diverted downwards. As the flow moves down and decelerates it gains vorticity, generating a vertical eddy behind the log. At locations where the flow is directed down some flow is able to reach deeper parts of the log filter. The porous flow of the log filter is minimal. Turbulence is quickly dissipated and the dye remained in place. Due to the presence of some wall flow the dye near the flume wall was transported downstream. For high discharges vertical eddies were observed less. Instead downwards diverted flow directly penetrated the log filter. Nonetheless the flow velocity and turbulence was quickly dissipated, indicating that the log filters functioned accordingly to the research by Bouman (2018). Although no dye was added during experiment BA14b vertical eddies were still observed. Backfilled sand was mobilised by vertical eddies created behind a log. The sand would be picked up and transported downstream.

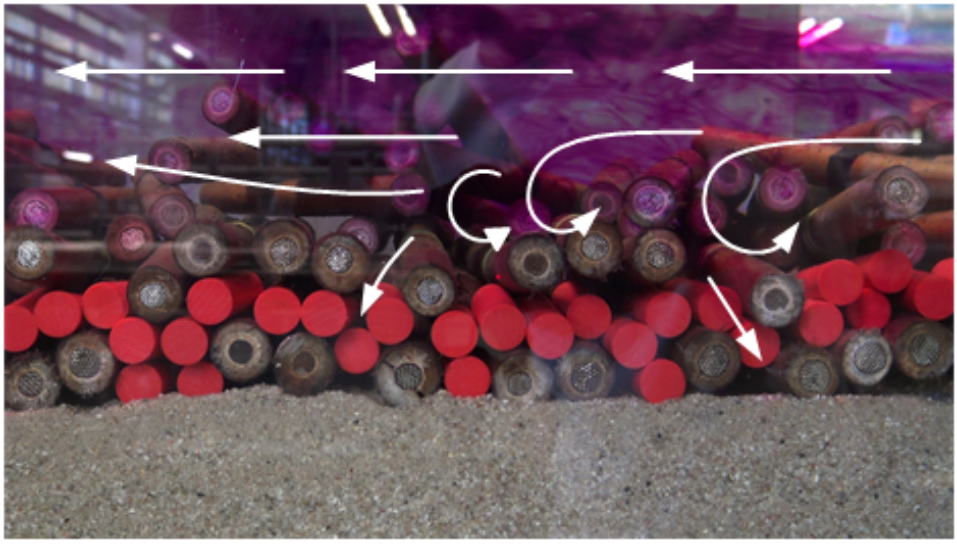

Figure 7.5: Streamlines of the flow observed in experiment SP18c

8

Discussion

The research in this thesis focused on the stability of log bed protections. The dependence of the stability on log mass (log diameter x log density), orientation and backfilling was researched. The internal flow of a log filter was observed using a dye. Furthermore the settling behaviour of logs was mapped by observing and measuring settling velocities and horizontal distributions. Thirdly the log density was monitored throughout the course of this thesis to gain insight in the saturation process. This chapter evaluates the results and discusses where the research is lacking. Connections are made between the results and the RWS pilot project

8.1. Limitations of the models

The number of model logs available for the experiments limited the variations possible for the experiments. Moreover the logs had varying densities and saturation rates. The long saturation process required the logs to be made heavier. This was done by hammering nails at both ends of the logs. This changes the moments of inertia. The moment of inertia around the centre axis of the logs decreased, while the moment of inertia around other axis increased. Less torque is required to roll logs and more torque is required to rotate logs. The effect was neglected in the experiments.

Two models were used in this research. In the first model only video cameras were used to process the experiments. The settling velocities and distribution had to determined by hand. Determining the settling velocities from a video recording requires a correction for perspective. In this thesis the correction was applied manually. The distributions were determined manually as well. From a top view image the centres of the logs were determined, a time consuming method.

The water depth in the flume was scaled differently than other geometry scales. The logs in the flume experiments are more easily transported because their relative size compared to the flow is larger than for the prototype logs.

8.2. Evaluation of the results

8.2.1. Monitoring of the log density

The log density is a key aspect of the feasibility of a log bed protection. For the design of a log bed protection the density is a frequently used parameter in stability equations (section 2.4). Unlike rocks, logs do not have a constant density. Logs for a bed protection need to saturate until the density exceeds that of the fluid in which it will be submerged. At this point the log sinks. The maximum achievable density of a log is not guaranteed beforehand but dependent on several factors such as water pressure, water temperature, wood type and wood quality.

In this thesis the density of willow twigs is monitored over a period of 8 months, chapter 4. The twigs were put in buckets and submerged by adding weight on top of the twigs. Periodically but irregularly the water would be refreshed. The water pressure and temperature were not regulated. At the start of the saturation process the density increased quickly. Nonetheless the saturation rate decreases quickly as well (observation show an exponential decay but this is not verified). In a period of 2-3 months the twigs would reach 95% of their maximum measured densities. Attempts were made to increase the saturation rate. Twigs were stripped of bark, drilled with holes or cut in shorter lengths. From this it was concluded that the primary saturation

is along the length of the twigs. Bark acts as a barrier to the dry wood. Removal of bark shortly increased the saturation rate but was insufficient. Drilling holes was futile. Cutting the logs in shorter lengths was the most effective. The practical application of this method for the pilot project is considered impractical. The willow twigs reached a maximum density between 1000-1100 kg/m^3. Some twigs never reached the threshold of 1000 kg/m^3.

The results showed that the saturation process of wood is not straightforward. Many factors influence the saturation rate and expected maximum densities are not guaranteed.

8.2.2. Evaluation of the settling behaviour

When constructing log bed protections in rivers it is important to know how the filter will end up. Structure porosity, permeability and orientation all play a role in the effectiveness of a filter. In this research the distribution of logs settling on a smooth flat bed was researched, see chapter 5.

The settling velocities measured in the experiments were accurate with Newton's settling velocity for particles in the turbulent regime, equation 2.24. For the heaviest logs the measured settling velocities were lower than expected. It is suggested that this was a result of insufficient water depth.

The experiments showed that horizontally dropped logs create filters with the lowest porosity. Logs dropped vertically settle in random directions and are difficult to stack layer by layer because a pyramid shape is created. When a volume of logs is dropped the experiments showed that larger volumes settle in a strip. Depending on the quantity and mass of the logs and the water depth the length of the strip is affected. Because each log diameter had a different density it was not possible to research the influence of different log diameters or densities. The water depth was also kept constant. A grading of log diameters and/or densities was not researched.

Experiments were done in standing water. In rivers a current will affect the settling of logs. This is not researched. Expected is that the theory available for rocks, discussed in section 2.5, can be applied to logs. Results from the settling experiments can be considered as a first step in determining the best construction method.

8.2.3. Evaluation of the filter roughness

The roughness of a log bed protection affects stability. The correct calculation of the bed roughness of a bed protection is an integral part of designing a safe and functioning bed protection. For rock bed protections equations exist to estimate the roughness. For log bed protections these equations are not verified.

In this thesis the roughness of a log bed protection is researched, chapter 6. The roughness of a bed protection can be expressed in terms of the zero velocity level z_0. From measuring the velocity profile above the log filter the zero velocity level was fitted. The measurements showed a dependency of z_0 on the discharge (flow velocity). For a rough bed z_0 should be independent of the flow. The discrepancy is related to the fact that z_0 is found through fitting. The accuracy of the z-coordinate of a measurement is of the same order as z_0 (millimetres). The accuracy of the data can therefor not be neglected in the analysis.

From the analysis two functions for the zero velocity level were found. The functions related z_0 to the log diameter of the log filter. The first function was a linear best fit. The second function a constrained linear best fit that required the function to pass through the origin. The second function resembles a similar function for z_0 that exists for rock filters. However this function causes a significant underestimation of the shear velocity. Adjustment of the hydraulic plane (z=0) did not increase the accuracy.

The roughness analysis showed that the roughness of a log filter is difficult to determine. Apart from the accuracy of the measurements the orientation of log filter with respect to the flow is important. The roughness of a log filter for one orientation is not necessarily the same as for another orientation due to the log geometry. Obtained functions for z_0 are research specific.

8.2.4. Evaluation of the stability criteria for a log filter

The stability of a log filter was researched using the critical Shields parameter (equation 2.20) in chapter 7. Results from the experiments showed that for logs perpendicular to the flow equation 2.20 can safely be used as a design criteria. The measured critical Shields parameters at which initial motion was observed for the log filters corresponds with the critical Shields parameter at which failure occurs for rock filters. The increase in stability of the log filters compared with rock filters is likely related to the interlocking effect of logs.

The stability layer of the log filters was uniform, except for one experiment. In this experiment the stability layer had a log diameter grading. Using the mean log diameter and mean density the critical Shields parameter correlated well with the other experiments. This suggests that when a grading is used for constructing a

log filter it is sufficient to use the mean log diameter and mean density. The effect of a different grading was not researched.

For logs with a different orientation, like parallel to the flow, equation 2.20 was coherent for the first two phases of stability. However it was assumed that the shear velocity acting on the parallel logs was equal to the perpendicular logs. It is not researched if this is true. Most likely the roughness of logs parallel to the flow is smaller and hence also the shear velocity.

The log filters in this research were constructed by hand and by using a funnel mechanism. In practice the entire log filter will be constructed using a certain mechanism. It is not researched what the effect is of constructing the first layers by hand and if a different mechanism results in a different stability. Secondly only one L/d ratio is researched. The L/d ratio is not included in equation 2.20. The effect of different ratios was not researched.

Backfilling of the log filter with sand did not result in significant changes in stability. Most of the sand was eroded before the first phase was reached. Backfilling with a larger volume could increase stability but this is not researched.

The log filters were approximately 4 log diameters thick. Bouman (2018) suggested that 3 log diameters would be sufficient. Observations of the internal flow (porous flow) of the log filters concluded that the log filters were functioning as intended. The effect of a different thickness of the log filter was not researched.

9

Conclusions

In this chapter we will answer the research question:

How well are stability criteria for rock bed protections applicable to log bed protections?

To answer this question the following subquestions are asked.

1. How do logs settle on a flat bed?
2. What is the roughness of a log bed protection?
3. How do log bed protections behave?

The saturation process of the model logs was measured throughout this research. From these measurements it became clear that using willow twigs as model logs is feasible, but time consuming if the saturation process is not accelerated. It was also found that the saturation process is primarily in longitudinal direction. A 5 m long 5 cm thick log will therefor need to saturate much longer than a 50 cm long 5 cm thick log. Attempts were done in to accelerate the saturation process: stripping logs of bark, drilling holes and cutting logs in smaller pieces. These attempts were not successful. It was opted to artificially increase the weight of the logs by hammering nails in both ends of the logs. This was successful but changes the moments of inertia of the log. This effect was neglected in the experiments.

The first subquestion "*How do logs settle on a flat bed?*" can be answered from the results of the settling experiment, discussed in chapter 5. Four release mechanisms were tested. From these tests it became clear that a horizontal drop orientation creates the most dense filter (lowest porosity) and the least spread. The hatch mechanism allows all logs to drop horizontally at the same time. The resulting distribution had a slightly larger spread than when logs were dropped one by one. The funnel mechanism allowed the most logs to be dropped at once. The resulting distribution, a strip of logs, is a good method for constructing log filters. A spread of 50-60 cm was found for the length of the strip and 30 cm for the width of the strip (i.e. 2-2.5 the log lengths and 1.5 lengths, respectively). As a large volume of logs settle using the funnel mechanism a U-shape is formed. When this U-shape reaches the bed collisions between logs increases the spread of the logs. Logs roll over the bed due to their inertia. The last mechanism rolled logs along a slope. As the logs enter the water they have an angular rotation. This creates a Magnus force. Four types of settling were observed:

- Drifting: Linear trajectory when the log enters the water
- Stalling: Parabolic trajectory when the log enters the water
- Changing direction: Angular velocity is dissipated. Oscillating direction due to stabilisation of the log
- Cancelling: Logs rotates vertically and settles

The second subquestion *What is the roughness of a log bed protection?* can be answered from the results of the roughness analysis. The velocity profiles above log filters for different discharges was measured. Equation 2.7 (Law of the Wall) was fitted to the data. The equation was modified to take the height of the log filter into

account (equation 6.2). This equation overestimated the shear velocity. The dependency of the zero velocity level on the log diameter and filter variation (standard deviation of the filter height) was determined. Only a correlation between the zero velocity level and the log diameter was found. Two functions were determined that correlates the zero velocity level with the log diameter. The first function is a best fit (unconstrained), the second constrains the fit to pass through the origin. This was done because the zero velocity level for a log with zero diameter is zero. Using both functions in the Law of the Wall equation and the modified equation showed that using the unconstrained function is accurate within 5.5% and the constrained function underestimated the shear velocity by up to 15%.

The last question *How do log bed protections behave?* can be answered from the stability experiments in the flume, chapter 7. The Shields stability criteria, equation 2.20, was used to determine the stability of the log filters. The initiation of motion for log filters corresponded with the failure stage for rock filters. Log filters are thus more stable than rock filters. The cause for this is most likely the interlocking effect of a log filter. Neighbouring logs stabilise each other by absorbing the hydraulic forces. Log filters also have a stabilising character. Displaced logs find new stable positions by settling in a sheltered area or by rotating parallel to the flow. When the hydraulic load becomes a deformation will not stabilise but instead escalate and start a chain reaction (failure).

We now answer the research question "*How well are stability criteria for rock bed protections applicable to log bed protections?*". In this thesis it became clear that for log bed protections tested in the flume experiments the stability criteria for rock bed protections can safely be applied. Log bed protections go through similar phases as rock bed protections. First a rocking movement is observed. Then small deformations occur. In the third phase logs are displaced over greater distances. Eventually the bed protection will fail. The critical Shields parameters at which these phases occur are larger than for rock. Designs for log bed protections that use the critical Shields parameter for rock bed protections are therefor guaranteed to be safe. It is unknown if the stability of log bed protections is dependent on the log length/log diameter ratio outside the range tested in this research (L/d=10-20).

10

Recommendations

Here recommendations are done regarding the RWS pilot project. The density of the willow twigs measured in this research showed that the saturation process of logs is time consuming. Logs of the same wood type but different diameter reached different densities. It is recommended to do more research on the maximum achievable densities. Varying with wood type, log length and log diameter would benefit the use of logs as a bed protection in the long term. For the use of wood as model logs it is advised to take the saturation time and frequent monitoring of the logs into account. If little time is available one could choose to either increase the weight using nails or by using a diaphragm vacuum pump. The latter can be an expensive alternative.

The tank experiments show that the funnel mechanism is most favourable for practical purposes. Large quantities of logs can be dropped at once with decent accuracy. The experiments however were rather simple and largely qualitative. If the drop method and accuracy of placement for logs is deemed important it is recommended to do more research on this topic. The TU Delft faculty of Civil Engineering & Geosciences already has a large 2x2x2m tank available in which experiments can be done on a larger scale with better methods and equipment. A mathematical model is already developed for dumped rock by (Cregten, 1995), de Reus (2014) and Meermans (1997).

The roughness of a log bed protection can be estimated in a similar way as rock bed protections. A function was found that related the roughness to the log diameter of the log filter. It is unknown if this function can be applied to log filters outside of this research. It is recommended to do more research on the roughness of a log bed protection if this is deemed necessary for a design. For a first estimate it is recommend to use the (mean) log diameter.

Stability analysis of the log filters shows that when using the equations for the critical Shields parameter, designed for rock filters, are used a conservative design is created. Generally critical Shields parameters are larger for logs than for rock with the same diameter. It is recommended to use the existing criteria for rock and use the rock critical Shields parameter of ψ_c=0.03. This ensures that deformations of the log filter remain small and unsafe situations are avoided.

The stability of logs parallel to the flow was approximately 50% larger than for logs perpendicular the flow. This leads to the idea that for the design of a log bed protection the foundation layer is oriented perpendicular to the flow while the stability layer (top layer) is oriented parallel to the flow.

It is also recommended to perform settling and stability experiments on a larger scale with different water depths, filter thickness and grading than is done in this research. More insight in the dependency of the stability of log bed protections on these parameters would not allow log bed protection to be designed at other locations than the pilot location (Oude Maas).

If backfilling of log bed protections is desired it is recommended to do more research in the volumes required to achieve significant increases in stability. Furthermore bundling of logs was not researched in this thesis. Research on the stability of log bed protections made out of bundles logs is required. This research should not be applied to bundled logs.

Bibliography

AndrewGoTo. Cell structure of hardwood and softwood, 2019. Accessed on August 21st 2019.

Laurens Beulink. Wood as a scour protection. Master's thesis, TU Delft, Februari 2018.

Roland Rubaij Bouman. Hydraulic load reduction as a function of depth in a filter layer consisting of logs. Master's thesis, TU Delft, July 2018.

Ceylan Çete and Samantha Haage. Bodemberscherming met behulp van boomstammen. *Bachelor Thesis*, 2016.

H.J. Cregten. Het gebruik van probalistische methoden bij het beoordelen van het stortresultaat van een zijstorter. Master's thesis, TU Delft, 09 1995.

CUR. Interface stability of granular filter structures, 2010.

J.S. de Reus. Het valgedrag van stortsteen onder invloed van stroming. Master's thesis, Delft University of Technology, 02 2014.

Fizzics. The magnus effect - a curved ball explained. https://www.fizzics.org/the-magnus-effect-notes-and-video/, 2019. Accessed on August 14th 2019.

Derek G. Goring and Vladimir I. Nikora. Despiking acoustic doppler velocimeter data. *Journal of Hydraulic Engineering*, 128(1):117–126, 2002.

J.R. Grace. Contacting modes and behaviour classification of gas—solid and other two-phase suspensions. *The Canadian Journal of Chemical Engineering*, 64(3):353–363, 1986. doi: 10.1002/cjce.5450640301. URL `https://onlinelibrary.wiley.com/doi/abs/10.1002/cjce.5450640301`.

G.J.C.M. Hoffmans. *The Influence of Turbulence on Soil Erosion*. Deltares select series. Eburon, 2012. ISBN 9789059726826. URL `https://books.google.nl/books?id=xqJweGwYw9QC`.

Raymond Lau, Meer Saiful Hassan, Wenyin Wong, and Tao Chen. Revisit of the wall effect on the settling of cylindrical particles in the inertial regime. *Industrial & Engineering Chemistry Research - IND ENG CHEM RES*, 49, 08 2010. doi: 10.1021/ie1012807.

G. Magnus. *Über die Abweichung der Geschosse*. Berlin, 1999.

W. Meermans. Voorspelling van het stort als gestort wordt vanuit een vast punt (dutch). Master's thesis, Delft University of Technology, 01 1997.

Y. Nakayama and R.F. Boucher. *Introduction to Fluid Mechanics*. Butterworth-Heinemann, 1999.

NortekAS. *The comprehensive manual*, 10 2017.

M.E. Weber R. Clift, J.R. Grace. *Bubbles, drops and particles*. Academic Press, 1978.

Rijkswaterstaat. KRW Jaarrapportage 2016. Technical report, Rijkswaterstaat, 2016.

Ruimte voor de Rivier. Planologische Kernbeslissing Deel 4. Technical report, PKB Ruimte voor de Rivier, 2018.

Richard Saucier. Shape factor of a random oriented cylinder. Technical report, Army Research Laboratory, 06 2000.

Gerrit J. Schiereck. *Introduction to Bed, bank and shore protection*. Delft Academic Press, 2016. Updated by H.J. Verhagen.

Arjan Sieben. Korte verkenning plaatsing hout Haringvliet/Hollands Diep tbv inventarisatie KRW maatregelen 2^{de} tranche. Technical report, Rijkswaterstaat, May 2016.

Bernd Spänhoff. Vacuum-pressure prewetting-a simple and rapid method to water saturate wood for experimental purposes: Simple and rapid method for prewetting of wood. *Limnology and oceanography, methods*, 5:2007, 07 2007. doi: 10.4319/lom.2007.5.289.

J.A.M. Stuifbergen. Reststroomsnelheidsmetingen. Technical report, Afdeling der Civiele Techniek, Vakgroep Vloeistofmechanica, 11 1981.

M. van den Berg. Overview of wood in rivers. Master's thesis, Delft University of Technology, 12 2018.

van Leeuwen, P., van Olst, L., and van der Scheer, B.H. Bodemberscherming met behulp van boomstammen. *Bachelor Thesis*, 2016.

L.C. van Rijn. *Principles of sediment transport in rivers, estuarines and coastal areas.* Aqua Publications, 1993.

C. Wieselsberger. The air resistance of spheres (german). *Zeitschrift für Flugtechnik und Motorluftschiffahrt*, 5:140–145, 1914.

K.C. Wilson, G.R. Addie, A. Sellgren, and R. Clift. *Review of Fluid and Particle Mechanics*, pages 15–50. Springer US, Boston, MA, 2006. ISBN 978-0-387-23263-8. doi: 10.1007/0-387-23263-X_2. URL `https://doi.org/10.1007/0-387-23263-X_2`.

WL. Storten van grind in stromend water. *Verslag modelonderzoek M598*, 1960.

A

Oude Maas bed level 2013

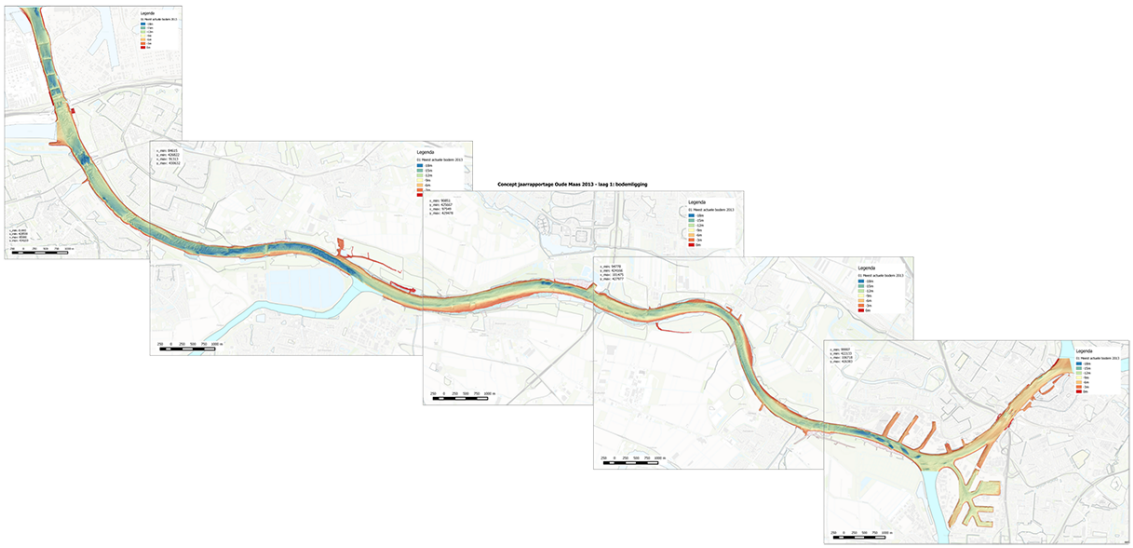

Figure A.1: All sections of Oude Maas stitched together (by hand)

B

Ruimte voor de Rivier Measures

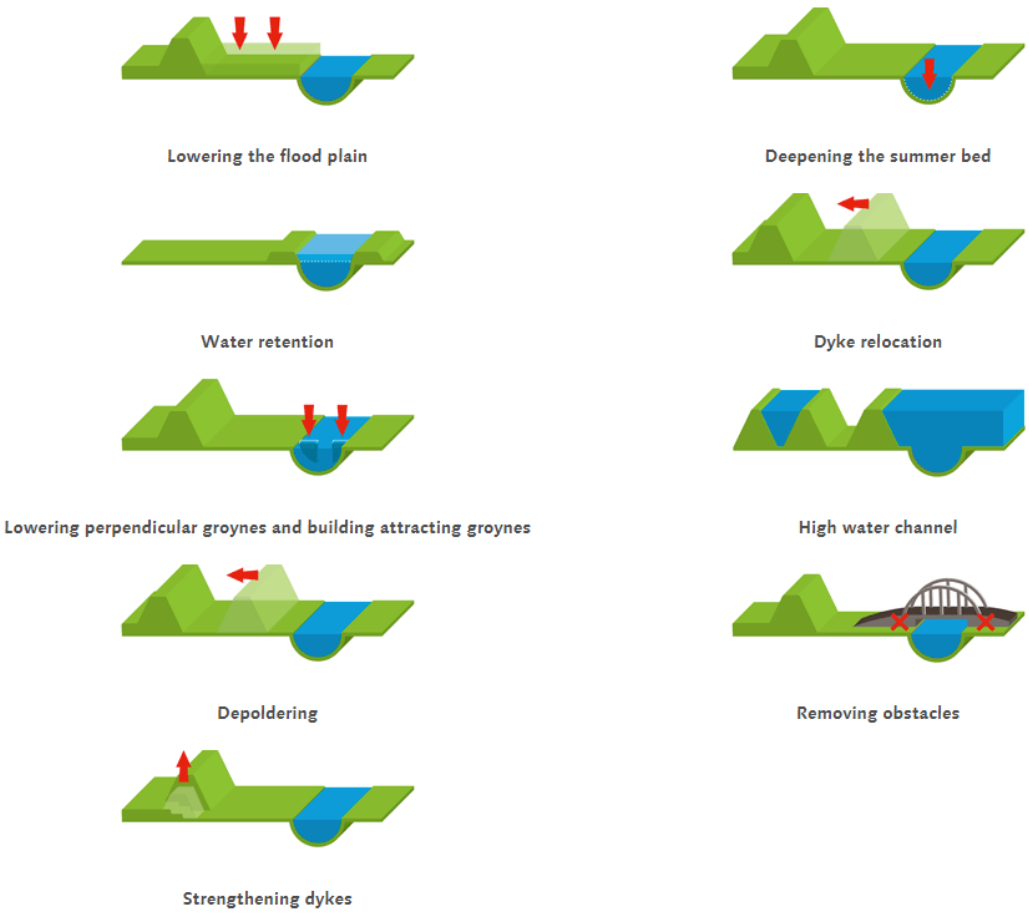

Figure B.1: Measurements to increase space for rivers

C

Stability of submerged logs

The first phase *What are the hydro-mechanical material properties?* is investigated by two groups of CEG graduate Bachelor students. The first group (Çete and Haage, 2016) performed scale experiments in a flume to test the stability of individual and connected submerged logs. The density of the logs was measured and two stability criteria were defined. The second group (van Leeuwen, P. et al., 2016) also performed scale experiment in a flume. More configurations were tested and the previously stability criteria reviewed. In this section their research is summarised and analysed.

C.1. Stability of logs in different configurations

Çete and Haage (2016) tested the effect of multiple layers of individual logs, different cross-sectional shapes and connections. The cross-sections are shown in figure C.1 and a summary of all experiments is given in table C.1. For each experiment, five logs are placed in the centre of the flume without spacing. Dimensions of the logs are 15x15x180mm (Height x Width x Length). The bed material used had an average diameter of 11.3mm. This is very coarse compared to the log diameter.

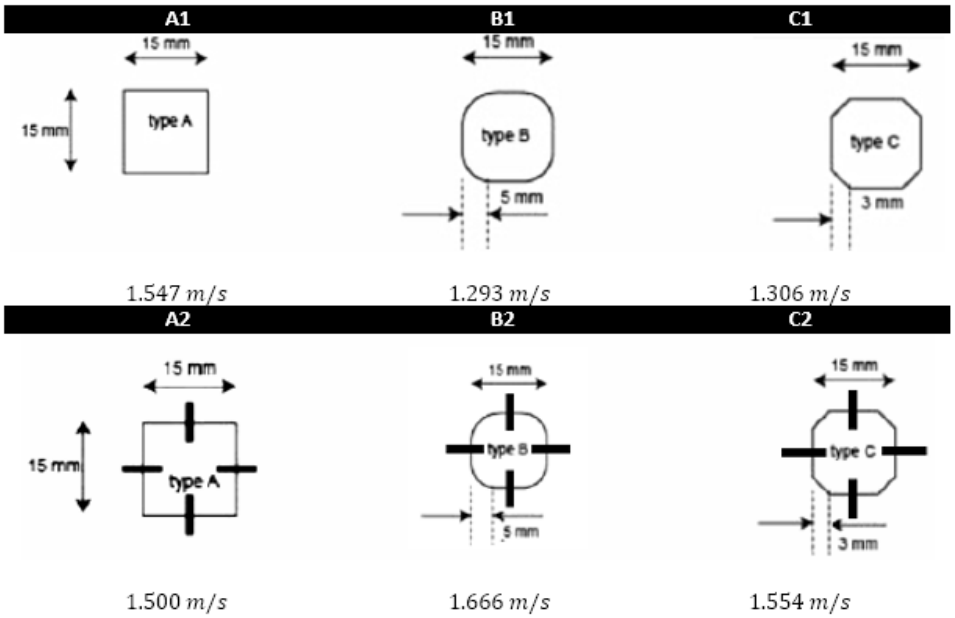

Figure C.1: Cross-sections used by (Çete and Haage, 2016) in their experiments

Test	Cross-section	# of Layers	Angle w.r.t. flow [deg]	Connection	u_c [m/s]	Note
1.1	A1	1	0	-	1.5	-
1.2	A1	2	0	-	1.2	-
1.3	A1	3	0	-	1.0	-
1.4	A1	4	0	-	0.4	Tested once
2.1	A1	1	0	-	1.5	This is test 1.1
2.2	A1	1	90	-	0.8	-
3.1	A1	1	0	None	1.5	This is test 1.1
3.2	A1	1	0	Tyrib	1.6	-
3.3	A1	1	0	Rope	1.6	-
4.1 - 4.6	A1 - C2	1	0	-	1.3 - 1.7	Test 4.1 is test 1.1. Crit. flow vel. are shown in figure C.1.
5.1	A1	1	0	Rope	1.6	This is test 3.3
5.2	B2	1	0	-	1.7	This is test 4.5
5.3	B2	1	0	Rope	1.2	Tested once

Table C.1: Table of experiments done by (Çete and Haage, 2016)

From these experiments the following conclusions could be made:

- Configurations with unconnected logs act as individual logs
- Multiple layers of individual logs do not increase stability
- Addition of branches and connections (generally) increases stability
- A combination of branches and connections does not further increase stability

From table C.1, test series 1, it is clear that the critical flow velocity (u_c) decreases with each added layer. This can be expected since flow velocities high up in the water column are larger than near the bottom. Also unconnected logs do not benefit from the presence of other logs and thus act as an individual log. Consequentially logs on the top layer experience higher local flow velocities and are thus less stable.

The orientation of a log has a large influence on the stability. Test series 2 show that u_c for logs placed perpendicular (test 2.2) to the flow is 50% smaller than for logs placed parallel to the flow (test 2.1). This is caused by an increase of exposed surface area to the flow. Moreover the rotation point is significantly decreased (from half a log length to half a log diameter).

The addition of branches and connections (tyrib or rope) increases u_c. However for connections this effect is minimal (1-3%). For branches the effect is larger. Contradictory is the addition of branches for type A where u_c slightly decreases (-3%). For types B and C the effect is positive, 29% and 19% respectively. For Type B2 the combination of branches and rope was tested (test 5.3). This test was run only once and showed a decrease in stability of 25%.

C.2. Stability of logs with varying log length and diameter

van Leeuwen, P. et al. (2016) continued with testing submerged logs. From the conclusions of the research by (Çete and Haage, 2016) they designed six variants, given in figure C.2. They only used type B1, B2, C1 and C2 for their experiments, as they resemble prototype logs more closely. Variant A tests the effect of spacing between logs. Variant B tests a different method of stacking logs for two and three layers (only the configuration for two layers is shown in figure C.2). The logs are connected using fishing wire. Variant C tests a complex construction, called an Impermeable Deflector Jam (DFJ). This is a type of Engineered Log Jam (ELJ). An ELJ acts as a soft alternative to hard bank protection methods. This is the only variant where roots are also tested (4x4cm gauze), as well as burying part of the construction in the bed. Variant D represents a (potential) more realistic configuration. Variant E is the reference configuration, used by Çete and Haage (2016). This is the only variant that uses type A1 logs and no spacing. Variant F is the only variant where the diameter and length of the logs are variable. This is done to test the effect of diameter and length on stability and verify the stability criteria by (Çete and Haage, 2016). Also the bed material is varied for all variants, except variant E. Variant E is the only variant where the rock bed material is used (1.13cm). All other variants are tested with coarse or fine sand, 448 μm and 193 μm respectively. The results are given in table C.2.

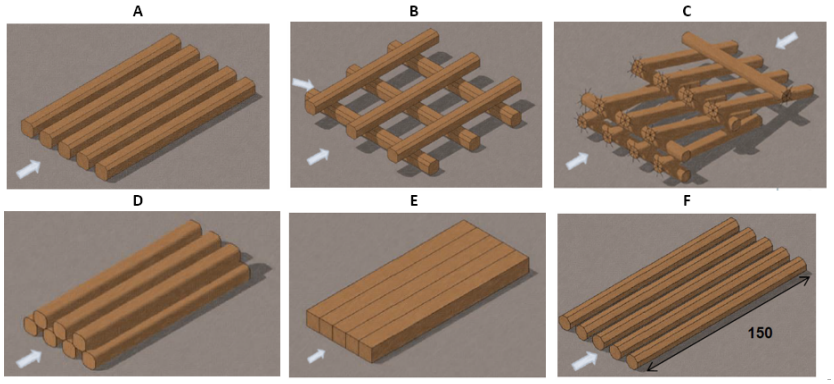

Figure C.2: Variants used by (van Leeuwen, P. et al., 2016) in their experiments

From table C.2 the following conclusions could be made:

- (Variant A & D) It is confirmed that the stability of C1>B1 and C2<B2
- (Variant B) Connected layers and branches increase stability (3>2) except for C2 with 3 layers
- Variant C is the least stable, likely due to lack of connections
- (Variant C) Roots and burying only work for flow in "head on" direction
- (Variant E) Bed material with a lower roughness reduce stability, while it is opposite for variant A
- (Variant F) Logs with a smaller diameter are less stable
- (Variant F) Shorter logs are not necessarily less stable

As can be seen in figure C.1 the critical flow velocities for C1>B1 (1%) and C2<B2 (−7%). The results by van Leeuwen, P. et al. (2016) confirm this with variant A, 3% and -4% respectively. Variant C is tested without connections. Due to the geometry of the configuration the addition of connections will likely increase the stability.

Test	Cross-section	# of layers	Angle w.r.t. flow [deg]	Bed material	u_c [m/s]	Note
A.1	B1	1	0	Coarse	1.3	
A.2	B1	1	0	Fine	1.4	
A.3	B2	1	0	Coarse	1.5	
A.4	B2	1	0	Fine	1.5	
A.5	C1	1	0	Coarse	1.4	
A.6	C1	1	0	Fine	1.5	
A.7	C2	1	0	Coarse	1.5	
A.8	C2	1	0	Fine	1.4	
B.1	B1	2	0	Coarse	1.0	
B.2	B1	3	0	Coarse	1.2	
B.3	B2	2	0	Coarse	1.3	
B.4	B2	3	0	Coarse	1.4	
B.5	C1	2	0	Coarse	1.0	
B.6	C1	3	0	Coarse	1.2	
B.7	C2	2	0	Coarse	1.2	
B.8	C2	3	0	Coarse	1.1	
C.1	B1	NA	0	Coarse	1.0	Flow from bottom left figure C.2
C.2	B1	NA	180	Coarse	1.2	Flow from top right figure C.2
C.3	B1	NA	0	Coarse	1.1	Incl. roots
C.4	B1	NA	180	Coarse	1.0	Incl. roots
C.5	B1	NA	0	Coarse	1.1	Incl. roots and buried
C.6	B1	NA	180	Coarse	1.0	Buried
D.1	B1	2	0	Coarse	1.2	
D.2	B2	2	0	Coarse	1.3	
D.3	C1	2	0	Coarse	1.2	
D.4	C2	2	0	Coarse	1.4	
E.1	A1	1	0	Coarse	1.3	
E.2	A1	1	0	Fine	1.4	
E.3	A1	1	0	Rock	1.6	(Çete and Haage, 2016) measured 1.5m/s
F.1	C1	1	0	Coarse	1.4	15x15x150mm (HxWxL)
F.2	C1	1	0	Coarse	1.3	10x10x150mm (HxWxL)
F.3	C1	1	0	Coarse	1.4	15x15x180mm (HxWxL)
F.4	C1	1	0	Coarse	1.3	10x10x180mm (HxWxL)

Table C.2: Table of tests done by (van Leeuwen, P. et al., 2016)

C.3. Analysis of stability

First we will discuss the different cross-sectional shapes without branches. It appears that the reduction in cross-sectional area for types B1 and C1 have the most significant impact on the stability, see table C.3. A reduction in cross-sectional area results in a smaller volumes. A smaller volume reduces the force by weight against lifting.

The effect of volume reduction can be quantified by introducing a representative diameter (d_{rep}), see equation C.1. The change in u_c is then proportional to $\sqrt{V}$, see table C.4.

$$u_{c,rep} = 1.2\sqrt{2\Delta g d_{rep}} = 1.2\sqrt{2\Delta g \frac{V}{dL}} \tag{C.1}$$

Type	A [mm^2]	V [mm^3 (%)]	u_c [m/s (%)]
A1	225	40500 (100)	1.547 (100)
B1	204	36637 (90.5)	1.293 (83.6)
C1	207	37260 (92.0)	1.306 (84.4)

Table C.3: Reduction in volume and critical velocity

Type	u_c [%]	$u_{c,rep}$ [%]	Difference [%]
A1	100	100	0
B1	83.6	95.1	11.6
C1	84.4	95.9	11.5

Table C.4: Reduction in stability from Izbash equation

Approximately 11.5% remains after correcting for volume reduction. What aspects are responsible for more reduction in critical flow velocity is unclear. Several aspects can be responsible for this. Firstly the bed roughness effects the flow around the log. A coarser bed allows more flow underneath the log, potentially increasing the lift force. Secondly the smooth(er) edges of types B1 and C1 reduces the contact surface of the log with the bed, reducing the resistance to shear forces. Moreover the smooth(er) edges reduce the resistance against rolling (sideways). Although this does not always reduce stability it can move a log in a less favourable position. Moreover rolling logs can interact with other logs, potentially starting a chain reactions.

The addition of branches has a negligible effect on the volume reduction. A clear cause to why type A is reduced in stability while type B and C increased has not been found. Nonetheless the increase in stability is most likely related to the change of interlocking behaviour. Branches can penetrate the bed, increasing the resistance against shear forces. However this does not explain why type A is less stable. To explain this a secondary effect from the branches has to be found. A potential cause is the effect of the branches on the position of the centre of mass and area for underflow. This can be directly related that nearer to the bed, lower velocities occur. This increases the stability of the log. Underflow area can have a positive and negative effect. A smaller area can potentially increase local flow velocities, reducing pressures underneath the log. This can generate downforce, increasing stability. However the presence of an underflow area can also generate local turbulence that can lift the log of the bed. Which effect was present during these experiments could not be determined.

From figure C.3 and table C.5 it is clear that the centre of mass distance and underflow area are largest for type A, then type C and then type B. This could mean that reducing underflow area is beneficial for the stability of the logs. Nonetheless it is advised to research this effect more thoroughly to confirm these results.

Type	Centre of mass [mm]	Underflow area [mm^2]
A2	9.75	11.25
B2	8.53	±6.00
C2	8.75	6.75

Table C.5: Geometry of types A2, B2 and C2

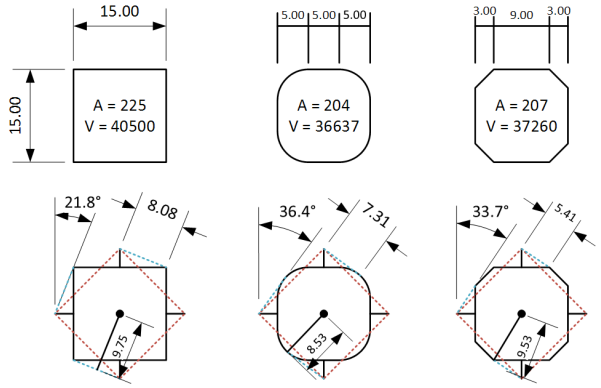

Figure C.3: Geometry of all different cross sections. All dimensions in mm. Area (A) is in mm^2. Volume (V) is in mm^3.

Both reports also presented the results expressed in the Izbash and Shields equations (equation C.2, more on these equation in 2.3). For Izbash the parameter α was determined, for Shields the equation was solved for ψ_c. β is a parameter related to the configuration (layers, angle to flow, connections and combinations). Note that for (van Leeuwen, P. et al., 2016) the value of β=1.0. More details about these equations can be found in 2.4 and the original report by van Leeuwen, P. et al. (2016). The results are given in table C.6.

$$u_c = \alpha\sqrt{2\Delta g d} \qquad and \qquad \psi_c = \beta\frac{u_*^2}{\Delta g d} \tag{C.2}$$

(Çete and Haage, 2016)				(van Leeuwen, P. et al., 2016)					
Test	α	β	ψ_c	Test	α	ψ_c	Test	α	ψ_c
1.1	1.9	1.40	0.035	A.1	1.5	0.012	C.1	1.1	0.006
1.2	1.5	0.90	0.010	A.2	1.6	0.011	C.2	1.3	0.009
1.3	1.2	0.73	0.007	A.3	1.8	0.016	C.3	1.3	0.009
1.4	0.5	0.65	0.001	A.4	1.7	0.013	C.4	1.2	0.007
2.1	1.9	1.41	0.035	A.5	1.6	0.013	C.5	1.3	0.009
2.2	1.0	1.41	0.009	A.6	1.7	0.013	C.6	1.2	0.008
3.1	1.9	1.40	0.035	A.7	1.8	0.016	D.1	1.2	0.007
3.2	1.9	1.40	0.036	A.8	1.6	0.012	D.2	1.4	0.010
3.3	2.0	1.40	0.038	B.1	1.2	0.007	D.3	1.5	0.011
4.1	1.9	1.40	0.035	B.2	1.4	0.010	D.4	1.5	0.009
4.2	1.8	1.40	0.032	B.3	1.5	0.011	E.1	1.5	0.012
4.3	1.6	1.40	0.025	B.4	1.3	0.009	E.2	1.6	0.011
4.4	2.1	1.40	0.041	B.5	1.1	0.006	E.3	1.9	0.054
4.5	1.6	1.40	0.025	B.6	1.4	0.010	F.1	1.8	0.017
4.6	1.9	1.40	0.033	B.7	1.4	0.010	F.2	1.8	0.018
5.1	2.0	1.40	0.038	B.8	1.3	0.009	F.3	1.7	0.016
5.2	2.1	1.40	0.041				F.4	1.9	0.019
5.3	1.5	1.40	0.023						

Table C.6: Bachelor results expressed in Izbash and Shields equations

From the gathered results it becomes clear that multiple layers of individual logs reduces stability. Also connections and branches have a positive impact on the stability. Bed material appears to have a significant influence on the stability, however some remarks regarding bed material have to be made. The first experiments were done on a rock bed with an average diameter close to the log diameter. In the second experiment the bed material was significantly reduced but only one layer, glued to a false bed, was present. Because the bed roughness can have quite an impact on the flow (and thus stability) . The β parameter used by Çete and Haage (2016) ranges from 0.65 to 1.41, while van Leeuwen, P. et al. (2016) used 1.0 for all experiments. Due to this, a reliable comparison between results based on ψ_c could not be obtained.

D

Stabilising scour holes

The second phase *How to stabilise scour holes?* is investigated by two CEG graduate Master students. The first research (Beulink, 2018) were scale experiments in a flume to analyse the erosion process around one log or one layer of logs. The second research (Bouman, 2018) were also scale experiments in a flume. However this research analysed the influence of layer thickness on the erosion. In this section their research is summarised and analysed.

D.1. Scour process with a log bed protection

Beulink (2018) measured the influence of a log bed protection on the scour process of the bed material. First scour holes caused by the erosion of the sand bed in a contracted zone of the flume was tested. Top view and side view are shown in figure D.1. Secondly the scour around a single log (referred to as burial scour), parallel to the flow, in the contracted zone was tested. These tests were done to obtain the morphological response of the bed caused by the presence of a log. The last tests were done with a single layer log bed protection (in the contracted zone) where the log elements were placed parallel or perpendicular to the flow. A summary of all tests is given in table D.1 and results in figure D.2. For Burial tests no scour volume or depth was measured, only a qualitative analysis was done.

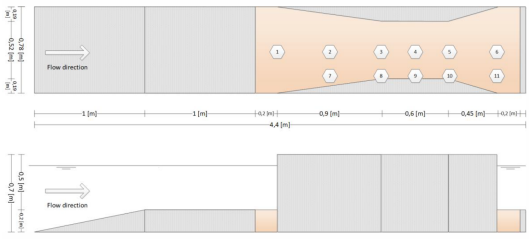

Figure D.1: Top and side view of part of the flume

Test	Max. u [m/s]	Run time [h]	Note
Basic 1	0.200	96	-
Basic 2	0.200	96	-
Basic 3	0.200	96	-
Burial 1	0.200	24	Stopped preemptively as scour was negligible.
Burial 2	0.225	144	Prolonged to further monitor scour process. Rotation observed.
Burial 3	0.250	72	Eroded below initial bed level.
Burial 4	0.275	72	Rotated 90 degrees within 6:15 hours and negligible development of scour after 48 hours.
Burial 5	0.300	96	Rotated 90 degrees within 5:00 hours and prolonged to compare with Basic tests.
Protected A	0.200	96	Parallel to flow
Protected A	0.200	96	Parallel to flow
Protected A	0.200	96	Parallel to flow
Protected B	0.200	96	Perpendicular to flow
Protected B	0.200	96	Perpendicular to flow
Protected B	0.200	96	Perpendicular to flow

Table D.1: Summary of tests performed by (Beulink, 2018)

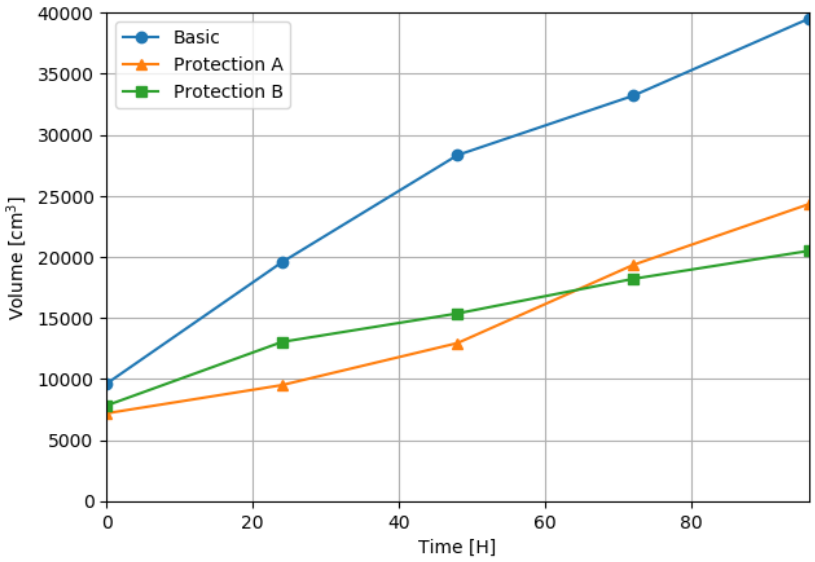

Figure D.2: Averaged total scour volume and maximum scour depth measured by (Beulink, 2018)

The basic scour tests showed similarities between the total scour volume for all tests (but mostly tests two and three), see figure D.2. The general scour pattern is initial erosion in the contracted zone, moving upstream in time and deposition in the expansion zone. However the initial shape of the bed seems to have a significant impact on the scour pattern. The burial scour tests was a qualitative analysis of the scour process around a single log, parallel to the flow direction. The initial scour pattern around the head of a log is horseshoe shaped (pier scour). The magnitude of the shape increases until a threshold is reached. After this threshold the horseshoe shape disappears and the log tilts in the direction of the scour hole. If erosion continues the log will eventually be positioned perpendicular to the flow direction. The erosion pattern now resembles pipeline scour instead of pier scour. Due to this tendency of the log to position itself perpendicular to the flow direction both mechanisms are tested. Protection A and B are parallel (cantilever) and perpendicular (staircase) to the flow direction, respectively (figure D.3). Both mechanisms reduce the scour volume and maximum scour depth by a similar percentage, approximately 50% and 8% respectively for only one layer of logs. However the staircase mechanism is beneficial in tidal regions due to bi-directional flow directions. The

cantilever mechanisms would induce two sided erosion, while the staircase mechanism does not, see figure D.4. Logs perpendicular to the flow direction is therefore recommended.

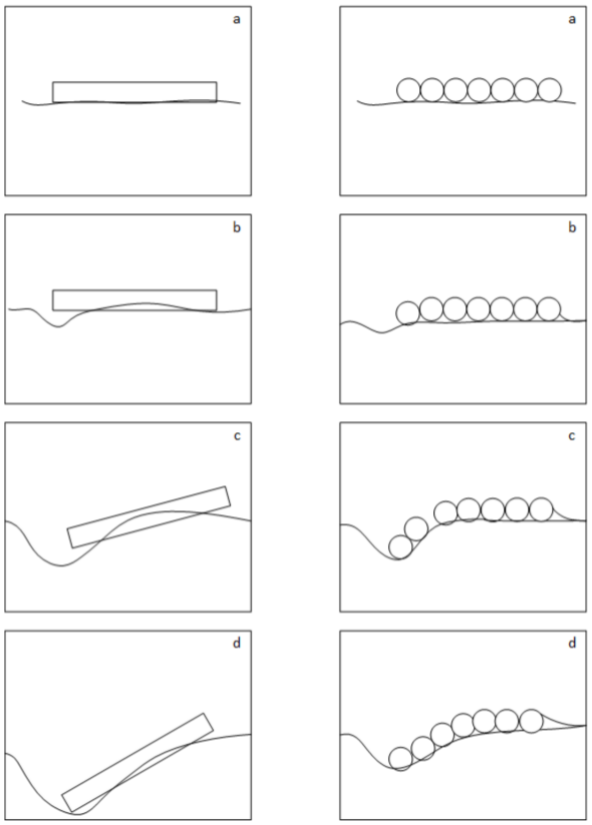

Figure D.3: Scour mechanisms (left) cantilever and (right) staircase

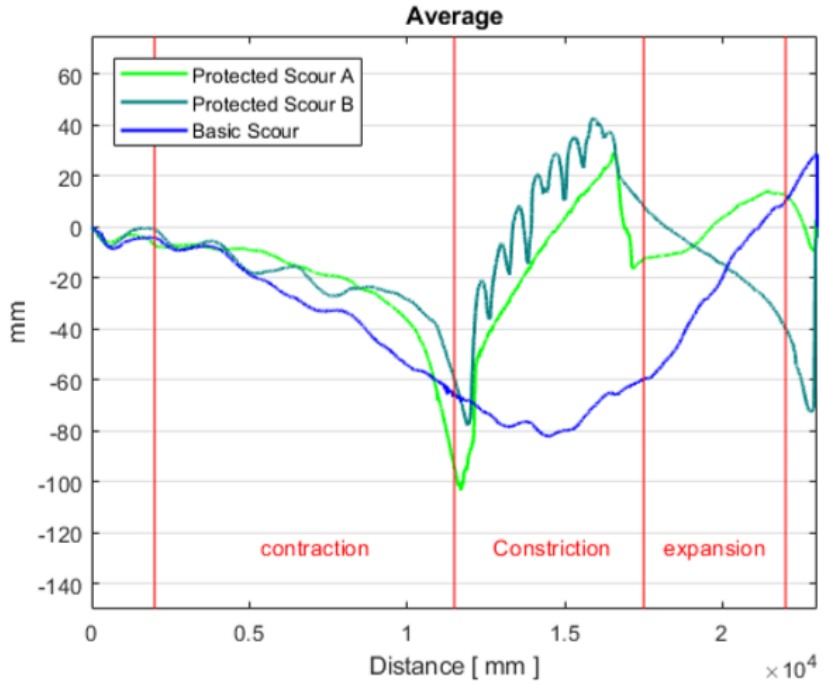

Figure D.4: Transects of averages

D.2. Hydraulic load reduction

Bouman (2018) continued with research on the scour process. The focus was to measure the hydraulic load reduction of a log bed protection (log filter) on the bed material. The hydraulic load is for example, a combination of shear stress and turbulence acting on a particle. Tests measured the velocity profiles above the log filter, velocity (fluctuations) inside the log filter and erosion volume, figure D.5a. A total of nine tests were done for locations 3 and 6. The region of each test is shown in figure D.5b, summarised in table D.2.

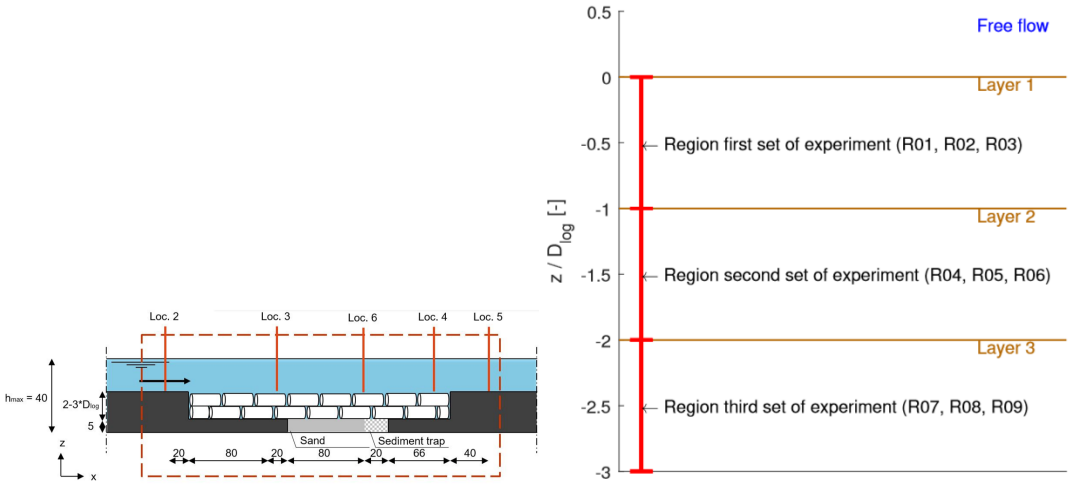

(a) (b)

Figure D.5: Flume section and regions

Test	Filter layer	Time steps	u_{loc3} [m/s]	u_{loc6} [m/s]	Note
R01	1	7	0.68	0.69	
R02	1	5	0.69	0.69	
R03	1	7	0.69	0.70	
R04	2	5	0.60	0.61	
R05	2	6	0.66	0.68	
R06	2	6	0.70	0.71	
R07	3	5	0.77	0.80	
R08	3	5	0.75	0.77	
R09	3	6	0.80	0.83	
R10	0	-	-	-	Velocity profile over filter length measured, Q=50m/s.

Table D.2: Average flow velocities (time and space) above the log filter measured in different filter layers. Each time step is ≈ 1.5 hours.

The scour process (Bouman, 2018) focused on was the process of winnowing and bed transport. Winnowing is the transport of bed material up the filter layers by turbulence. Bed transport is generated by shear stresses. This combination can cause the winnowed bed material to be transported downstream, causing scour. Mapping pore velocity and turbulent kinetic energy and comparing it with theory of open rock filters provided insight in the functionality of a log filter. In figure D.6a and D.6b respectively, a graph of the pore velocity and turbulent kinetic energy distribution are shown. Note that these distributions are for open rock filters.

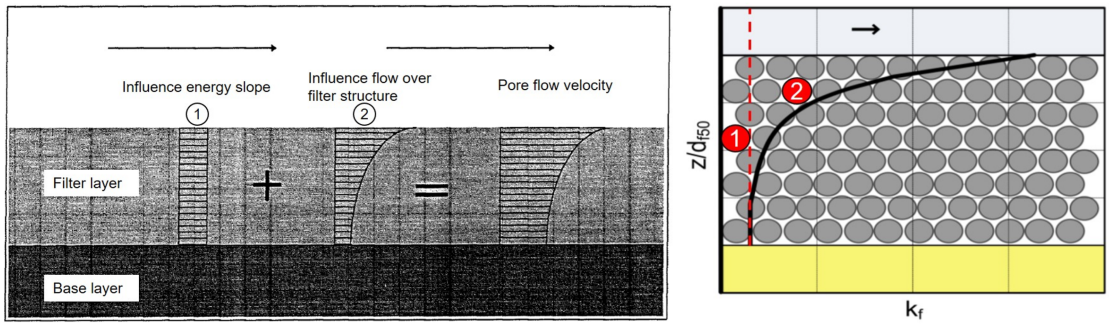

(a) Filter pore velocity

(b) Turbulent kinetic energy

Figure D.6: Filter pore velocity and turbulent kinetic energy for rock filters. Zone 1 in (b) is the constant k_r by the energy slope, zone 2 is k_r induced by the flow over the filter.

Two clear zones can be distinguished. The first zone only consists of influences by the energy slope. The energy slope is a constant, because it is related to the transport of momentum by a constant slope. For physical models this is the water level slope, for rivers this is the bed slope (the water level slope is generally equal to the bed slope when considering uniform river flow). The second zone is the influence of the filter. The difference in flow velocity between free flow and bed pore flow is present over the filter layers. This theory is similar for turbulent kinetic energy. For open rock filters the pore velocity can be described by equation D.1 ((Hoffmans, 2012)). The turbulent kinetic energy by equation D.2 ((Hoffmans, 2012) and (CUR, 2010)).

$$\overline{u_p}^2(z) = \overline{u_{p,S}}^2 + \left(\overline{u_p}^2(0) - \overline{u_{p,S}}^2\right)\exp\left(\frac{z}{L_d}\right) \quad \text{with} \quad \overline{u_{p,S}} = \sqrt{2gd_{f15}S_e/C_D} \tag{D.1}$$

$$k_f(z) = k_{f,S} + \left(k_f(0) - k_{f,S}\right)\exp\left(\frac{z}{L_d}\right) \quad \text{with} \quad k_{f,S} = \frac{2gr_f^2 S_e d_{f15}}{C_D} \tag{D.2}$$

X_S : Influence of energy slope

$A\exp\frac{z}{L_d}$: Influence of turbulent kinetic energy

d_{f15} : Diameter of the filter material of which 15% is finer [m]

S_e : Mean energy slope, here equal to water slope [-]

L_d : Damping length [m]

α_d : Damping coefficient [-]

The local relative turbulence intensity in the filter layer (r_f) is defined as:

$$r_f = \frac{\sqrt{k(z)}}{\overline{u_p}} \tag{D.3}$$

The damping coefficient for Reynolds numbers between 10^3 and 10^5 is defined as:

$$\alpha_d = \frac{2r_f^2}{C_D\chi_k} \tag{D.4}$$

Where χ_k is the turbulence parameter. For a rough bed χ_k=3.3. Hoffmans proposed α_d=1.5. The damping length is defined as:

$$L_d = \sqrt{\frac{c_v T_p}{\pi}} \tag{D.5}$$

From experiments R08 and R09 this theory could be validated. The measured pore velocities at the deepest point in the filter ($\overline{u_{p,dm}}$) are compared with the mean energy slope pore velocity ($\overline{u_{p,S}}$) from equation D.1. The same is done for the turbulent kinetic energy at the deepest point in the filter ($\overline{k_{f,dm}}$ and $\overline{k_{f,S}}$) from

equation D.2. Dividing the values by the mean flow velocity the pore velocities are made dimensionless. The results are given in table D.3. From this it is concluded that at least two (effective) layers of logs are required to reduce the hydraulic load to a minimum. However the theory of rock filters could not be applied directly to a log filter. From figure D.7 this becomes apparent. The black line is the schematic distribution for a log filter, the dashed red line the theoretical exponential function from equations D.1 and D.2. The red line with bullets is the schematic distribution averaged over the first, second and third filter layers.

Other conclusions from the experiments were:

- Flow around a log is very an-isotropic. Flow stagnates in front of a log, generating a downwards jet. Behind the log eddies are present.
- The shape of the pores in a log filter are different than in rock filters, causing relative turbulence to not be uniform in all directions (0.5 in z-direction compared to horizontal directions).
- Turbulent kinetic energy is constant below the second log layer, while for rock this is the fifth layer.
- The relative turbulence parameter for log filters is 0.36, while that of rock filters is 1.0.
- A larger porosity reduces the critical flow velocity for initiation of erosion, vice versa.

	R08					R09				
t	i	$\frac{\overline{u_{p,S}}}{\overline{u}}$	$\frac{\overline{u_{p,dm}}}{\overline{u}}$	$\overline{k_{f,S}}$	$\overline{k_{f,dm}}$	i	$\frac{\overline{u_{p,S}}}{\overline{u}}$	$\frac{\overline{u_{p,dm}}}{\overline{u}}$	$\overline{k_{f,S}}$	$\overline{k_{f,dm}}$
[-]	[‰]	[-]	[-]	$[m^2/s^2]$	$[m^2/s^2]$	[‰]	[-]	[-]	$[m^2/s^2]$	$[m^2/s^2]$
1	3.0	0.10	0.12	$3.39{\cdot}10^{-4}$	$2.61{\cdot}10^{-4}$	3.0	0.10	0.14	$3.35{\cdot}10^{-4}$	$3.66{\cdot}10^{-4}$
2	4.2	0.11	0.11	$4.75{\cdot}10^{-4}$	$3.05{\cdot}10^{-4}$	3.8	0.10	0.14	$4.24{\cdot}10^{-4}$	$4.45{\cdot}10^{-4}$
3	5.6	0.11	0.12	$6.32{\cdot}10^{-4}$	$3.61{\cdot}10^{-4}$	5.6	0.11	0.14	$6.35{\cdot}10^{-4}$	$5.23{\cdot}10^{-4}$
4	5.0	0.10	0.12	$5.60{\cdot}10^{-4}$	$4.72{\cdot}10^{-4}$	6.0	0.11	0.14	$6.78{\cdot}10^{-4}$	$6.48{\cdot}10^{-4}$
5	5.9	0.09	0.12	$6.66{\cdot}10^{-4}$	$5.54{\cdot}10^{-4}$	6.8	0.11	0.14	$7.72{\cdot}10^{-4}$	$6.97{\cdot}10^{-4}$
6	-	-	-	-	-	8.2	0.11	0.14	$9.24{\cdot}10^{-4}$	$8.00{\cdot}10^{-4}$

Table D.3: Ratio of measured and calculated pore velocities over mean flow velocity for multiple gradient at the deepest point of measurement in the filter.

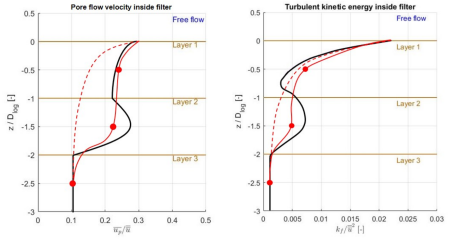

(a) Pore flow velocity (b) Turbulent kinetic energy

Figure D.7: Schematically distribution of pore velocity and turbulent kinetic energy in the filter layers.

E

Derivation of settling velocities

E.1. Spherical particles

E.1.1. Stokes' settling velocity

In 1851, George Gabriel Stokes derived an equation for the settling velocity of small particles in laminar flow. This is known as Stokes' Law (Stokes' settling velocity). At terminal settling velocity the drag force equals the gravitational force (F_d=F_g). Using spherical particles (sand-density: d<50μm) and laminar conditions (Re_s<0.1) the settling velocity the derivation is as follows:

$$F_d = F_g \qquad AC_D\frac{1}{2}\rho_w w_s^2 = Vg(\rho_s - \rho_w)$$

For a sphere in the laminar regime holds that C_D=24/Re_s and $Re_s = \frac{w_s d}{\nu}$, such that the equation is now:

$$A = \frac{\pi}{4}d^2 \quad \text{and} \quad V = \frac{\pi}{6}d^3$$

$$\frac{\pi}{4}d^2 C_D\frac{1}{2}\rho_w w_s^2 = \frac{\pi}{6}d^3 g(\rho_s - \rho_w) \tag{E.1}$$

$$\frac{24\nu}{d\,w_s}\rho_w w_s^2 = \frac{4}{3}d\,g(\rho_s - \rho_w) \tag{E.2}$$

$$\mu w_s = \frac{1}{18}d^2 g(\rho_s - \rho_w) \tag{E.3}$$

$$w_s = \frac{(\rho_s - \rho_w)gd^2}{18\mu} \tag{E.4}$$

E.1.2. Grace's settling velocity

In the transitional flow regime (0.1<Re_s<500) the drag coefficient has to be found by iteration. To eliminate iterations, R. Clift (1978) developed a method using dimensionless parameters. Co-author J.R. Grace later suggested using d^* and w_s^* as dimensionless parameters (Grace, 1986). These dimensionless parameters are given in equations E.5 and E.6. Their relations are shown in figure E.1 and their analytic expressions in E.1.

$$d^* = d\sqrt[3]{\frac{\rho_w(\rho_s - \rho_w)g}{\mu_w^2}} \tag{E.5}$$

$$w_s^* = w_s\sqrt[3]{\frac{\rho_w^2}{\mu_w(\rho_s - \rho_w)g}} \tag{E.6}$$

Range	Correlation
$d^* \leq 3.8$	$w_s^* = (d^*)^2/18 - 3.1234E-4(d^*)^5 + 1.6415E-6(d^*)^8$
$3.8 < d^* \leq 7.58$	$\log(w_s^*) = -1.5446 + 2.9162(\log(d^*)) - 1.0432(\log(d^*))^2$
$7.58 < d^* \leq 227$	$\log(w_s^*) = -1.64758 + 2.94786(\log(d^*)) - 1.0907(\log(d^*))^2 + 0.17129(\log(d^*))^3$
$227 < d^* \leq 3500$	$\log(w_s^*) = +5.1837 - 4.51034(\log(d^*)) + 1.687(\log(d^*))^2 - 0.189135(\log(d^*))^3$

Table E.1: Analytic expressions for the correlation for w_s^* as a function of d^*, after Grace (1986)

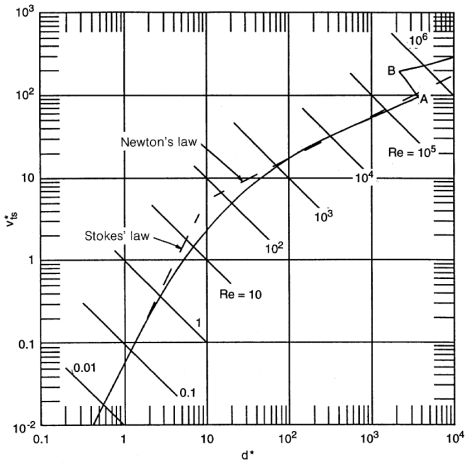

Figure E.1: Dimensionless settling velocity w_s^* as a function of the dimensionless particle diameter d^* for spheres, after Grace (1986)

E.1.3. Newton's settling velocity

The logs used in the experiments are much larger than 50μm and are therefor not in the laminar nor the transitional regime, but in the turbulent regime. Stokes' derivation can not be directly applied. In the turbulent regime (Re_s>500) the drag coefficient (C_D) becomes approximately constant. This is known as Newton's Law for settling velocity. Instead of C_D being dependent on Re_s it is considered constant ($C_D \approx 0.445$). Starting from equation E.2 the derivation is as follows:

$$0.445\rho_w w_s^2 = \frac{4}{3} dg(\rho_s - \rho_w) \tag{E.7}$$

$$w_s^2 = 3dg\left(\frac{\rho_s - \rho_w}{\rho_w}\right) \tag{E.8}$$

$$w_s = 1.73\sqrt{\left(\frac{\rho_s - \rho_w}{\rho_w}\right) gd} = 1.73\sqrt{\Delta g d} \quad \text{with} \quad \Delta = \frac{\rho_s - \rho_w}{\rho_w} \tag{E.9}$$

$$w_s = 1.73\sqrt{\frac{\rho_s - \rho_w}{\rho_w} gd} = 1.73\sqrt{\Delta g d} \quad \text{with} \quad \Delta = \frac{\rho_s - \rho_w}{\rho_w} \tag{E.10}$$

E.2. Cylindrical particles

E.2.1. Stokes' settling velocity

Derivation is similar to spherical particles, see E.1 to E.4 but with cylindrical geometry.

$$A = dL \quad \text{and} \quad V = \frac{\pi}{4} d^2 L$$

$$dLC_D\frac{1}{2}\rho_w w_s^2 = \frac{\pi}{2}d^2Lg(\rho_s-\rho_w) \tag{E.11}$$

$$C_D\rho_w w_s^2 = \frac{\pi}{2}dg(\rho_s-\rho_w) \tag{E.12}$$

$$\frac{24\nu}{dw_s}\rho_w w_s^2 = \frac{\pi}{2}dg(\rho_s-\rho_w) \tag{E.13}$$

$$\mu w_s = \frac{\pi}{48}dg(\rho_s-\rho_w) \tag{E.14}$$

$$w_s = \frac{\pi(\rho_s-\rho_w)gd}{48\mu} \tag{E.15}$$

E.2.2. Newton's settling velocity

Derivation is similar to spherical particles, see E.7 to E.9 but with $C_D \approx 0.8$. Starting from E.12 the derivation is:

$$0.77\rho_w w_s^2 = \frac{\pi}{2}dg(\rho_s-\rho_w) \tag{E.16}$$

$$w_s^2 = 2.04dg\left(\frac{\rho_s-\rho_w}{\rho_w}\right) \tag{E.17}$$

$$w_s = 1.43\sqrt{\left(\frac{\rho_s-\rho_w}{\rho_w}\right)gd} = 1.43\sqrt{\Delta g d} \quad \text{with} \quad \Delta = \frac{\rho_s-\rho_w}{\rho_w} \tag{E.18}$$

F

Scale calculations

First the prototype and model Froude and Reynolds numbers are calculated.

Parameter	Prototype	Model	Scale
g [m^2/s]	9.81	9.81	1:1
ν [m^2/s]	10^{-6}	10^{-6}	1:1
h [m]	14.0	0.14	1:100
U [m/s]	2.0	0.2	$1:\sqrt{100}$
d [m]	0.3-0.7	0.01-0.02	≈1:30

Table F.1: Parameter scales for Froude and Reynolds scaling

$$Fr_p = \frac{U_p}{\sqrt{g h_p}} = 0.17 \qquad Fr_m = \frac{U_m}{\sqrt{g h_m}} = 0.17$$

$$Re_p = \frac{U_p h_p}{\nu} = 2.8 \cdot 10^7 \qquad Re_m = \frac{U_m h_m}{\nu} = 2.8 \cdot 10^4$$

The scales for Froude and Reynolds are 1:1 and $1:10^3$, respectively. This means that the hydraulic conditions are correctly scaled for Froude. For Reynolds the scaled conditions are still turbulent, however the drag coefficient for cylinders in the 10^7 and 10^4 regimes are very different. The maximum flow velocity (2 m/s) does not occur frequently in a tidal river section and occurs primarily near the water surface. It is therefor assumed that the most common Reynolds number on prototype scale is more around 10^5-10^6. The drag coefficients are then almost constant and differences are negligible. Also the flow velocity in the model will likely exceed 0.2 m/s because the logs are of a higher scale (1:30). Therefor the Reynolds number in the model is more commonly higher than 10^4. This means that in both the prototype and the model the drag coefficients are similar and thus the hydraulic load on the logs is representative.

G

Release mechanisms

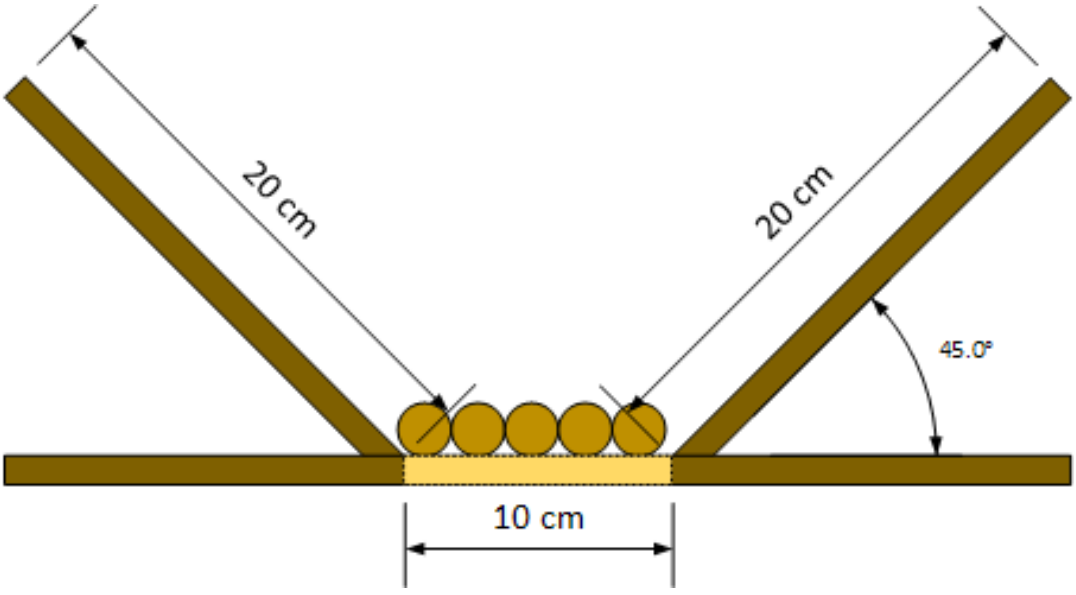

Figure G.1: Funnel mechanism used in the Settling experiment. Circles represent logs with a diameter of 2.0 cm.

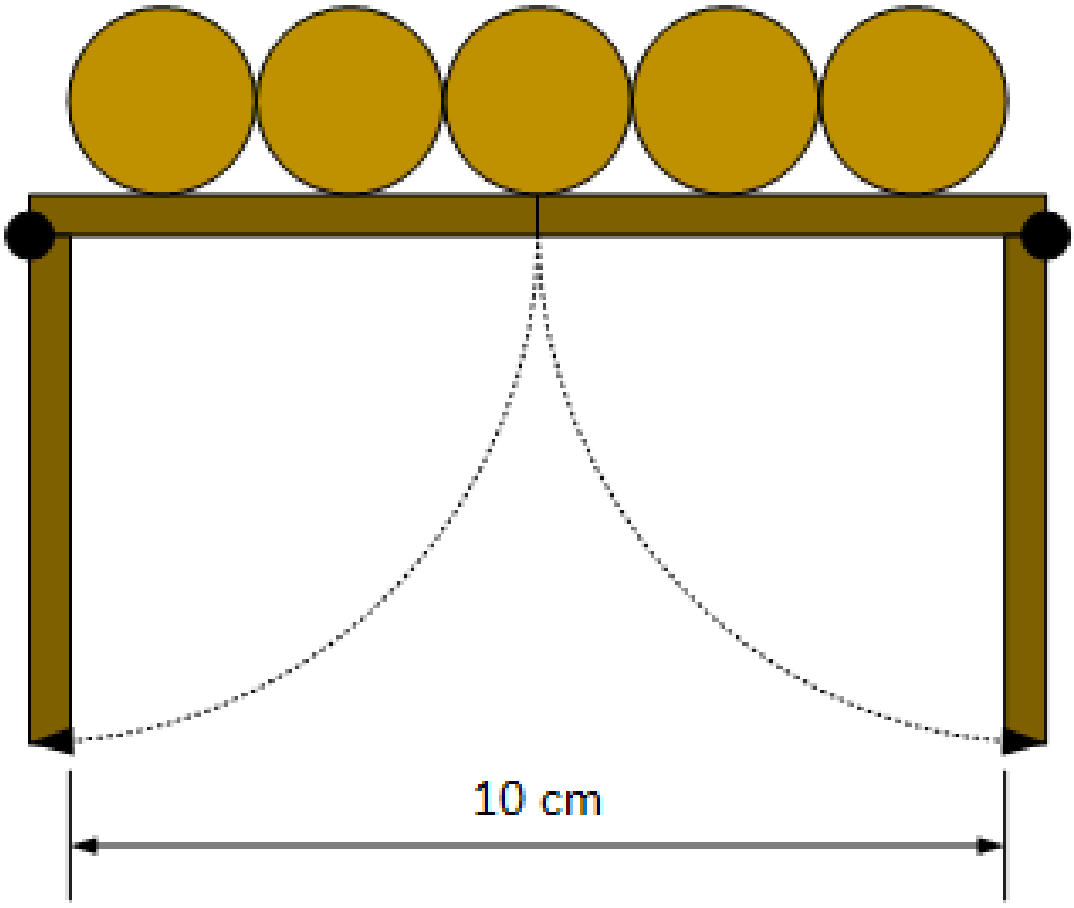

Figure G.2: Hatch mechanism used in the Settling experiment. Circles represent logs with a diameter of 2.0 cm.

H

Cross sections of flume experiments

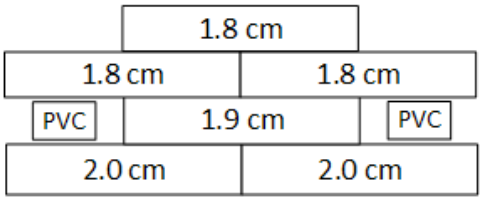

(a) Cross section of experiments RP18

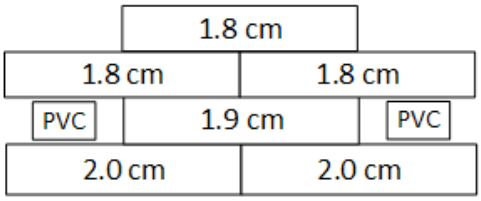

(b) Cross section of experiments SP18

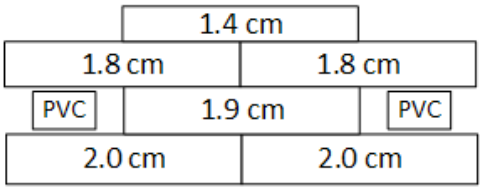

(c) Cross section of experiments SP16

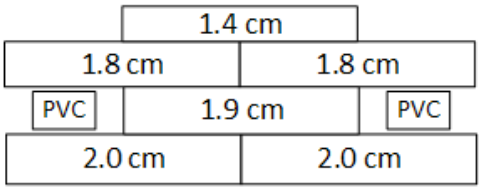

(d) Cross section of experiments SP14

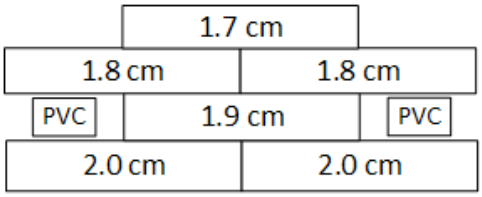

(e) Cross section of experiments SP17

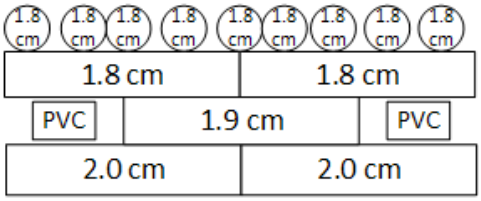

(f) Cross section of experiments SR18

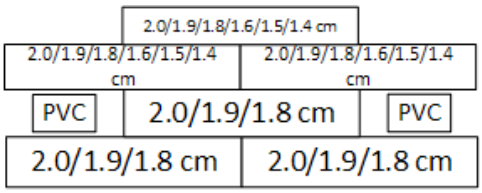

(g) Cross section of experiments CP15

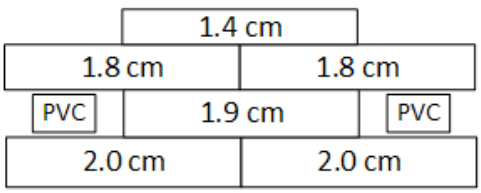

(h) Cross section of experiments BA14

Calibration figures

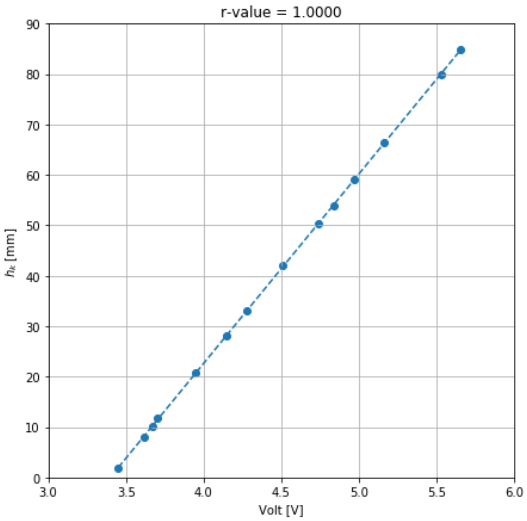

(a) Calibration of the submerged laser

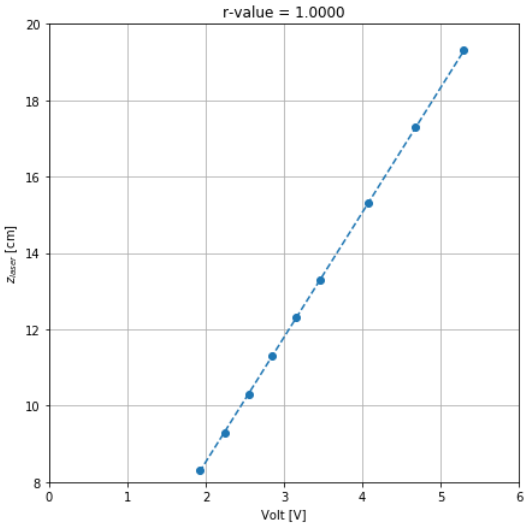

(b) Calibration of the Rehbock weir

J

Nails used to increase weight

J.1. First batch

d [cm]	1.0-1.2	1.2-1.4	1.4-1.6	1.6-1.8	1.8-2.0	2.0-2.2
ρ_{log} [kg/m^3]	0.85	0.85	0.80	0.80	0.80	0.80

Table J.1: Log density before nails, first batch

d [cm]	$m_{nail,min}$ [g]	$m_{nail,max}$ [g]	Nail [WxL]	m_{nail} [g]
1.0	2.000	2.750	2.7x50	2.374
1.1	2.375	3.875	2.7x55	2.547
1.2	2.750	4.000	2.7x60	2.772
1.3	3.125	4.625	2.8x60	3.186
1.4	3.875	5.375	3.0x65	3.897
1.5	5.250	7.125	3.5x80	5.655
1.6	6.000	8.000	-	-
1.7	6.750	9.125	4.0x80*	8.171*
1.8	7.625	10.250	4.0x90	9.097
1.9	8.500	11.375	4.0x90	9.097
2.0	9.500	12.625	4.0x100	10.257

Table J.2: Required additional mass for target density 1100-1200 kg/m^3, used nail and respective mass, first batch. (*) Nail shortened to 4.0x80.

J.2. Second batch

d	$\rho_{log,target}$	$\rho_{log,1}$ / $\rho_{log,2}$	Nail_1 / Nail_2	$M_{nail,1}$ / $M_{nail,2}$
[cm]	[kg/m^3]	[kg/m^3]	[WxL]	[g]
1.0	-	-	-	-
1.1	-	-	-	-
1.2	1298	1081	2.7x50	2.335
1.3	1284	939 / 1015	3.0x70 / 3.0x60	4.008 / 3.296
1.4	1276	918 / 1012	3.0x80 / 3.0x70	4.4386 / 4.008
1.5	1314	975	3.5x80	5.655
1.6	-	1000	3.5x80	5.655
1.7	1276	938	-	-
1.8	1295	914	4.0x90	9.097
1.9	1300	939 / 1004	4.0x90 / 4.0x90	9.097 / 9.097
2.0	1308	807 / 961	5.0x100 / 4.0x100	10.257 / 15.732

Table J.3: Required additional mass for target density of first batch on 27-02-2019, used nail(s) and respective mass(es), second batch.

K

Settling velocity measurements

For some experiments not all seven measurements could be done or an experiment had to be excluded from the calculations due to large deviations from the mean. The latter happened only once, for log diameter 1.2 cm, sample 3. For which samples and no measurement could be done are shown in table K.1.

d	NaN	Excluded
1.0		
1.1	7 at x=0 8 at x=0 9 at x=0	
1.2	10 at x=0	Sample 3
1.3	9 at x=0 10 at x=0	
1.4	10 at x=0	
1.5	8 at x=0 9 at x=0 10 at x=0	
1.6	N.A.	N.A.
1.7	5 at x=0 9 at x=0 10 at x=0	
1.8	4 to 10 at x=0	
1.9	2 to 5 at x=0 7 to 9 at x=0	Sample 10*
2.0	3 at x=0 4 at x=0 6 to 10 at x=0 9 at x=5	

Table K.1: No measurement (NaN, defined as "Sample at x=..") and excluded samples. (*) Only nine logs were dropped for log diameter 1.9 cm.

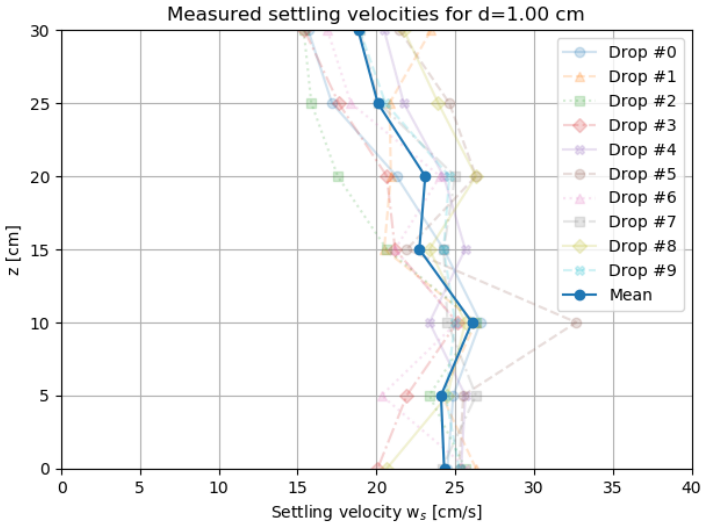
Measured settling velocities for d=1.00 cm
Drop #0
Drop #1
Drop #2
Drop #3
Drop #4
Drop #5
Drop #6
Drop #7
Drop #8
Drop #9
Mean
z [cm]
Settling velocity w_s [cm/s]

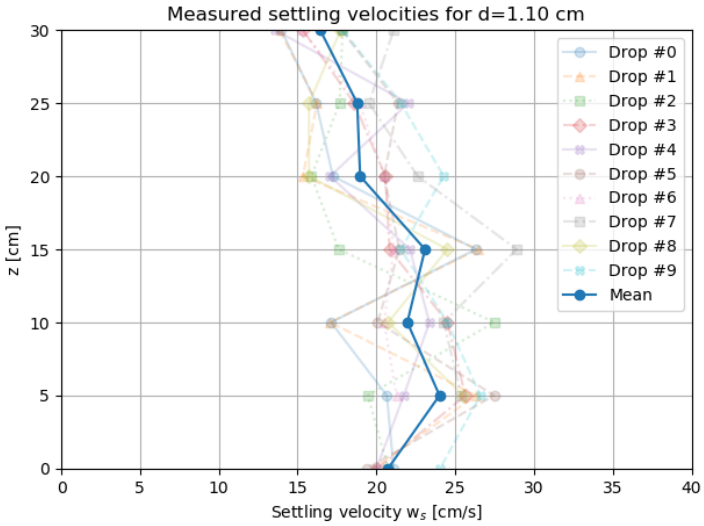
Measured settling velocities for d=1.10 cm
Drop #0
Drop #1
Drop #2
Drop #3
Drop #4
Drop #5
Drop #6
Drop #7
Drop #8
Drop #9
Mean
z [cm]
Settling velocity w_s [cm/s]

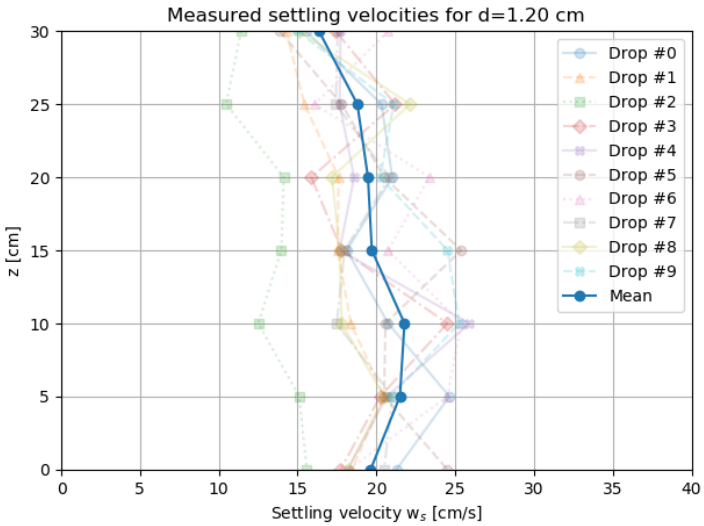
Measured settling velocities for d=1.20 cm
Drop #0
Drop #1
Drop #2
Drop #3
Drop #4
Drop #5
Drop #6
Drop #7
Drop #8
Drop #9
Mean
z [cm]
Settling velocity w_s [cm/s]

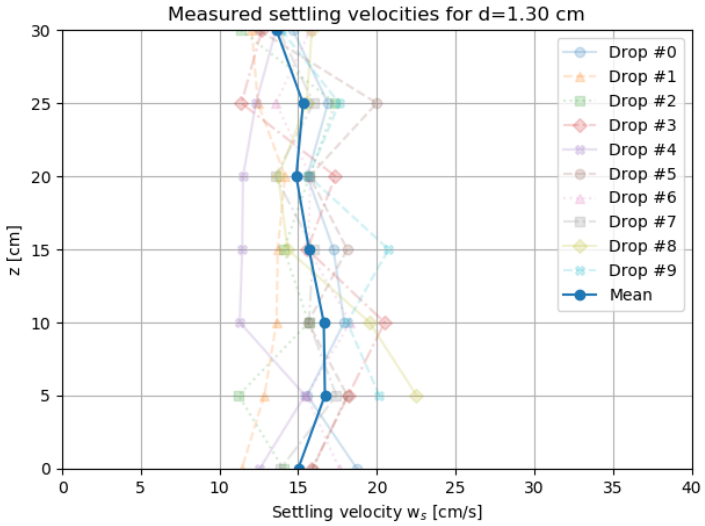
Measured settling velocities for d=1.30 cm
z [cm]
Settling velocity w_s [cm/s]
Drop #0
Drop #1
Drop #2
Drop #3
Drop #4
Drop #5
Drop #6
Drop #7
Drop #8
Drop #9
Mean

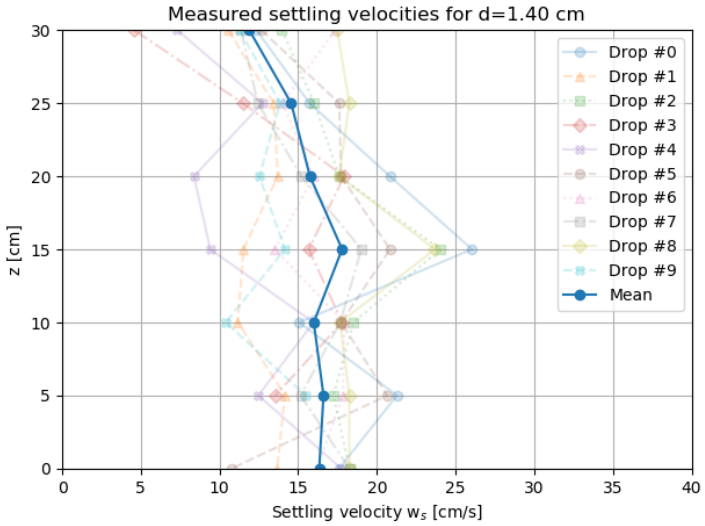
Measured settling velocities for d=1.40 cm
z [cm]
Settling velocity w_s [cm/s]
Drop #0
Drop #1
Drop #2
Drop #3
Drop #4
Drop #5
Drop #6
Drop #7
Drop #8
Drop #9
Mean

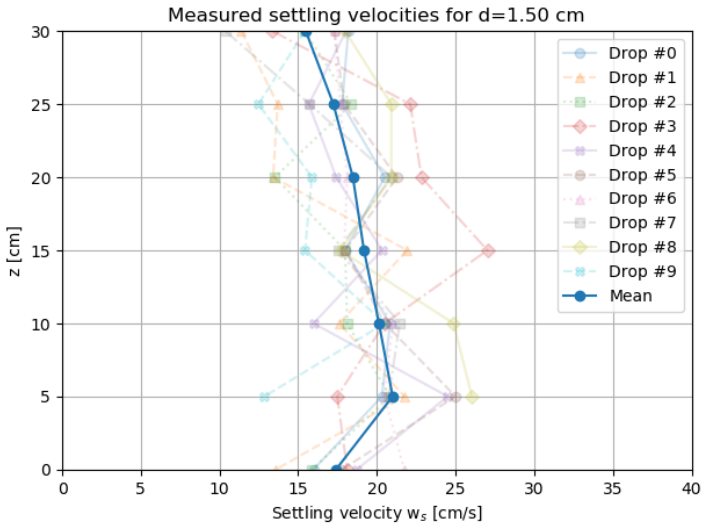
Measured settling velocities for d=1.50 cm
z [cm]
Settling velocity w_s [cm/s]
Drop #0
Drop #1
Drop #2
Drop #3
Drop #4
Drop #5
Drop #6
Drop #7
Drop #8
Drop #9
Mean

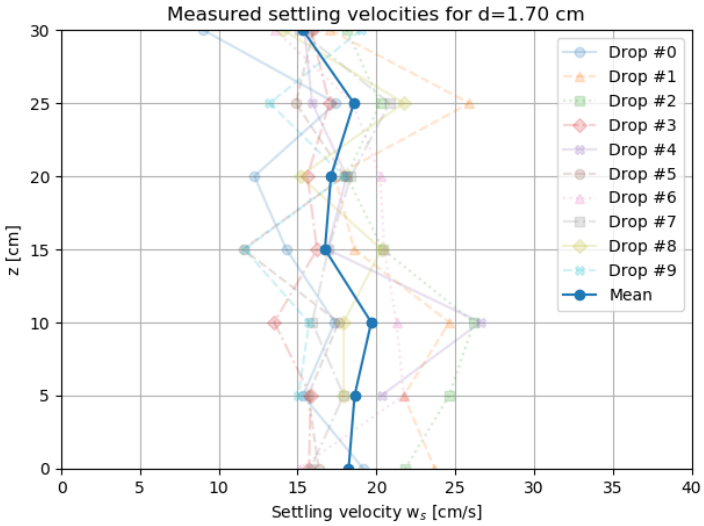
Measured settling velocities for d=1.70 cm
Drop #0
Drop #1
Drop #2
Drop #3
Drop #4
Drop #5
Drop #6
Drop #7
Drop #8
Drop #9
Mean
z [cm]
Settling velocity w_s [cm/s]

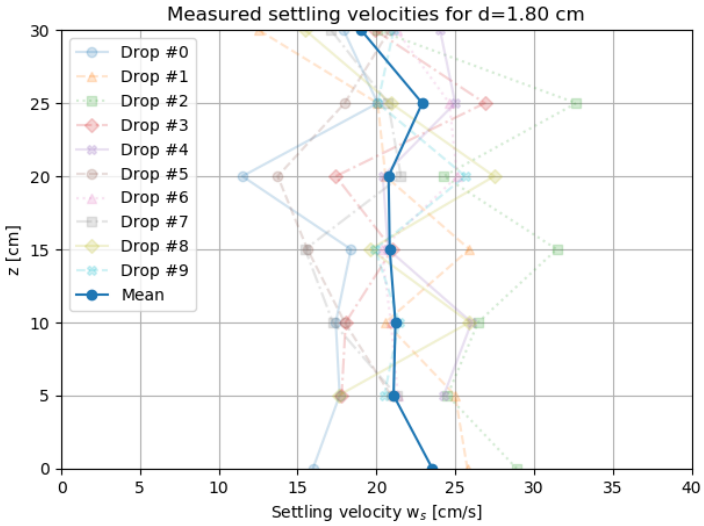
Measured settling velocities for d=1.80 cm
Drop #0
Drop #1
Drop #2
Drop #3
Drop #4
Drop #5
Drop #6
Drop #7
Drop #8
Drop #9
Mean
z [cm]
Settling velocity w_s [cm/s]

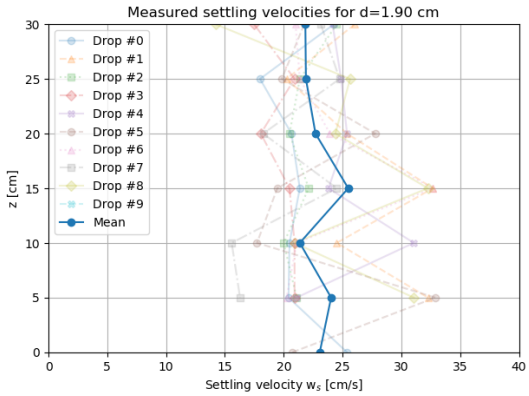
Measured settling velocities for d=1.90 cm
Drop #0
Drop #1
Drop #2
Drop #3
Drop #4
Drop #5
Drop #6
Drop #7
Drop #8
Drop #9
Mean
z [cm]
Settling velocity w_s [cm/s]

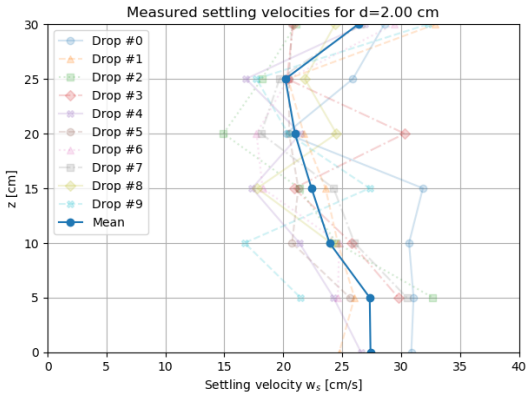
Measured settling velocities for d=2.00 cm
Drop #0
Drop #1
Drop #2
Drop #3
Drop #4
Drop #5
Drop #6
Drop #7
Drop #8
Drop #9
Mean
z [cm]
Settling velocity w_s [cm/s]

L

Settling velocity calculations

L.1. Determining settling regime

The settling Reynolds number for a settling log can be calculated as follows:

$$Re_s = \frac{w_s d_{log}}{\nu} \tag{L.1}$$

Calculating the particle Reynolds number for the logs in experiment HMV shows that the logs settle in the turbulent regime (Re_s>1000), see table L.1.

d [cm]	1.0	1.1	1.2	1.3	1.4	1.5	1.6	1.7	1.8	1.9	2.0
Re_s [-]	2430	2469	2479	2080	2335	2914	-	3114	3901	4462	5053

Table L.1: Particle Reynolds number for settling logs

The fact that the logs settle in the turbulent regime becomes more apparent when we calculate the Stokes', Grace's and Newton's settling velocities for both spherical and cylindrical particles. First the calculations for Grace's method are given.

For spherical particles we first determine the dimensionless diameter (d^*) using equation E.5. Using d^* we use table E.1 to find the corresponding equation to be used to calculate the dimensionless settling velocity, w_s^*. Using equation E.6 we can calculate Grace's settling velocity w_s.

For cylindrical particles we apply the shape factor parameter $\xi = w_{ns}/w_s$. In order to calculate the value for ξ we first calculate the volumetric form factor, equation 2.25. The presented area is calculated using 2.27, where we assume that $\theta = \pi/2$. Using equation 2.29 we can calculate ξ. Grace's settling velocities for spherical and cylindrical particles are given in table L.2.

	Spherical			Cylindrical			
d	d^*	w_s^*	w_s	A_p	K	ξ	w_{ns}
[cm]	[-]	[-]	[m/s]	[m^2]	[-]	[-]	[m/s]
1.0	142.51	25.78	1.809	0.0020	0.12	0.31	0.562
1.1	145.72	26.17	1.975	0.0022	0.13	0.32	0.633
1.2	145.58	26.15	2.155	0.0024	0.13	0.33	0.712
1.3	135.33	24.92	2.394	0.0026	0.14	0.34	0.814
1.4	156.36	27.41	2.455	0.0028	0.14	0.35	0.850
1.5	178.23	29.91	2.517	0.0030	0.15	0.35	0.887
1.6	-	-	-	-	-	-	-
1.7	205.48	32.91	2.723	0.0034	0.16	0.37	0.994
1.8	227.94	35.33	2.790	0.0036	0.17	0.37	1.035
1.9	232.17	35.78	2.928	0.0038	0.17	0.38	1.104
2.0	246.99	28.78	2.330	0.0040	0.17	0.38	0.892

Table L.2: Computed dimensionless diameter and settling velocity for spherical and cylindrical particle using log dimensions and density.

The theoretical settling velocities for all three methods are summarised in table L.3.

		Spherical			Cylindrical		
d	Density	Stokes'	Grace's	Newton's	Stokes'	Grace's	Newton's
[cm]	[kg/m^3]	[m/s]	[m/s]	[m/s]	[m/s]	[m/s]	[m/s]
1.0	1295	16.08	1.81	0.294	6.03	0.562	0.243
1.1	1237	15.63	1.98	0.277	5.86	0.633	0.228
1.2	1182	14.28	2.16	0.253	5.36	0.712	0.209
1.3	1115	10.59	2.39	0.210	3.97	0.814	0.173
1.4	1142	15.17	2.46	0.242	5.69	0.850	0.199
1.5	1171	20.97	2.52	0.275	7.86	0.887	0.227
1.6	-	-	-	-	-	-	-
1.7	1180	28.35	2.72	0.300	10.63	0.994	0.247
1.8	1207	36.55	2.79	0.331	13.71	1.036	0.273
1.9	1186	36.60	2.93	0.322	13.72	1.104	0.266
2.0	1192	41.86	2.30	0.336	15.70	0.892	0.277

Table L.3: Computed settling velocities for spherical and cylindrical particles

It is clear that Stokes' and Grace's methods are not suited for logs. Stokes' method is only valid in the laminar regime and very small particle. Grace's method for cylindrical particles was a lot more accurate than for spherical particles. This can indicate that for the transitional regime Grace's method could be used for logs. For the logs in this thesis however the method is not suitable. Newton's method is the most accurate as was already noticed from calculating the particle Reynolds number.

L.2. Calculating the wall effect

A correction for the wall effect can be done to the measurements. Using equations 2.32 and 2.33 we calculate θ and $w_s/w_{s,\infty}$. Diameter (D) is related to cylindrical tanks. In this thesis a rectangular tank is used. For diameter D we calculate the equivalent diameter, i.e. the diameter of a cylindrical tank with the same surface area as the rectangular tank. This means that instead of using D=600 mm we use D=677 mm. The remaining calculates are done and summarised in table L.4.

d [cm]	dL [mm^2]	L/d [-]	L/D [-]	d/D [-]	θ [rad]	$w_s/w_{s,\infty}$ [-]
1.0	2000	20.00	0.333	0.017	0.664	1.1075
1.1	2200	18.18	0.333	0.018	0.628	1.0918
1.2	2400	16.67	0.333	0.020	0.595	1.0787
1.3	2600	15.38	0.333	0.022	0.566	1.0678
1.4	2800	14.29	0.333	0.023	0.539	1.0584
1.5	3000	13.33	0.333	0.025	0.515	1.0504
1.7	3400	11.76	0.333	0.028	0.473	1.0372
1.8	3600	11.11	0.333	0.030	0.454	1.0317
1.9	3800	10.53	0.333	0.032	0.437	1.0269
2.0	4000	10.00	0.333	0.033	0.421	1.0225

Table L.4: Computed values for θ and $w_s/w_{s,\infty}$ for all log diameters. D = 600 mm, l = 200mm.

M

Manual release figures

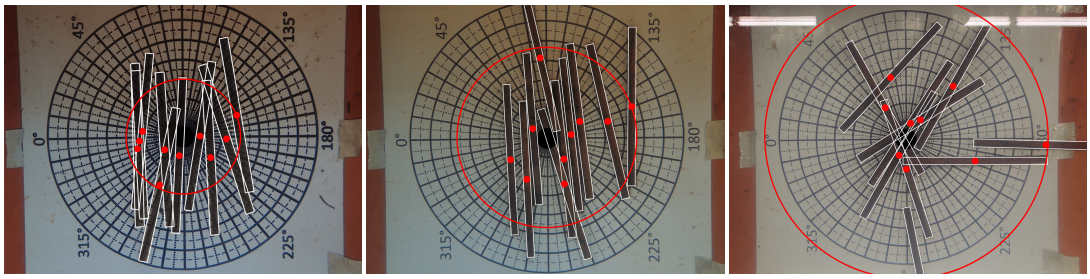

(a) HMS10 (b) HMT10 (c) VMT10

Figure M.1: Results for log diameter experiments HMS10, HMT10 and VMT10

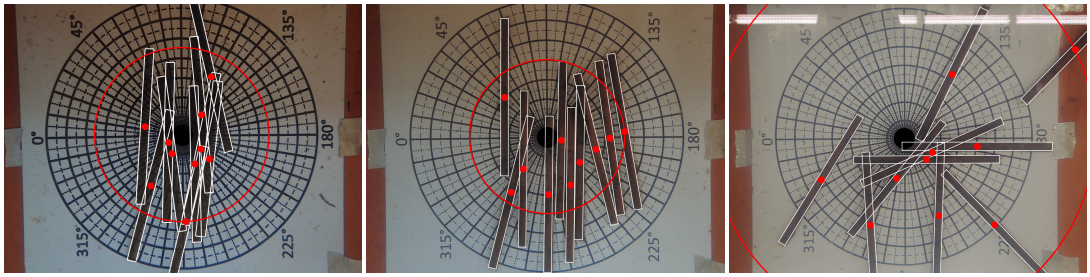

(a) HMS11 (b) HMT11 (c) VMT11

Figure M.2: Results for experiments HMS11, HMT11 and VMT11

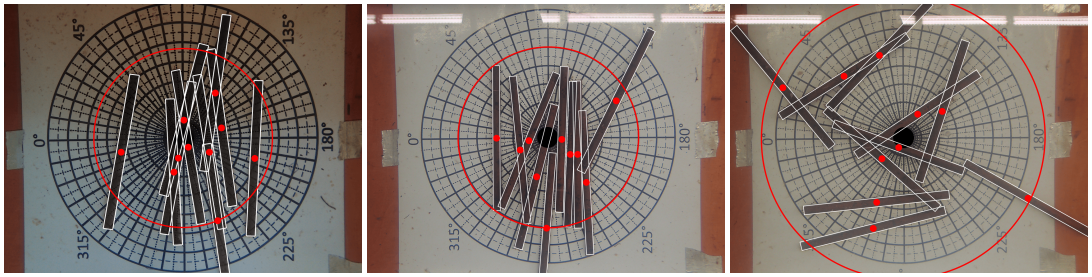

(a) HMS12 (b) HMT12 (c) VMT12

Figure M.3: Results for experiments HMS12, HMT12 and VMT12

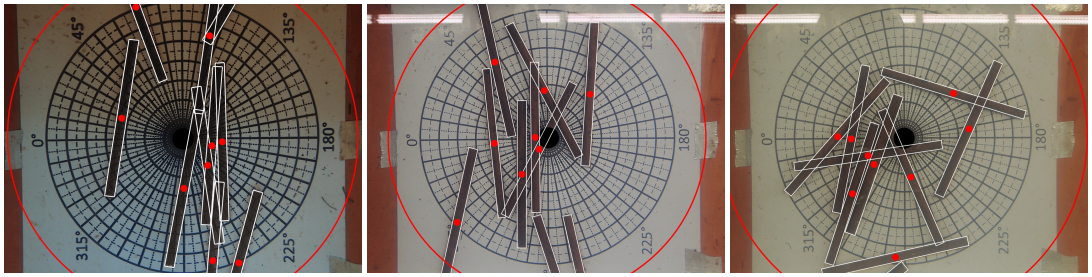

(a) HMS13 (b) HMT13 (c) VMT13

Figure M.4: Results for experiments HMS13, HMT13 and VMT13

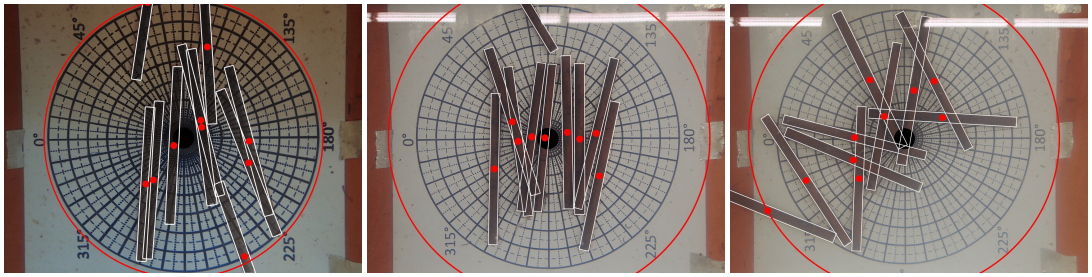

(a) HMS14 (b) HMT14 (c) VMT14

Figure M.5: Results for experiments HMS14, HMT14 and VMT14

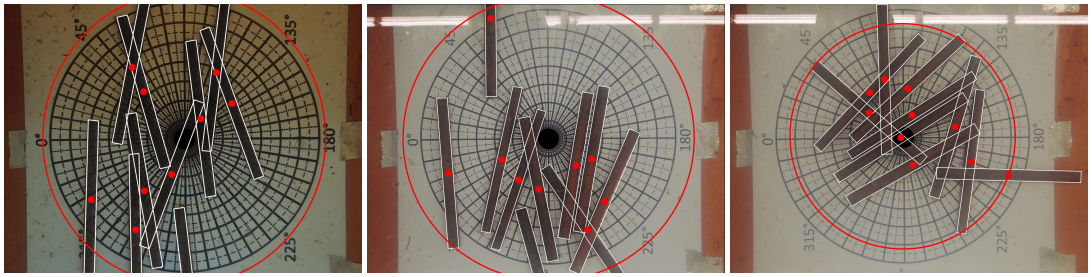

(a) HMS15 (b) HMT15 (c) VMT15

Figure M.6: Results for experiments HMS15, HMT15 and VMT15

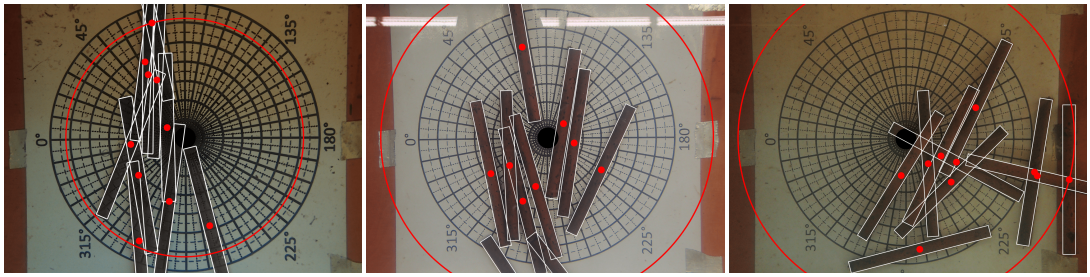

(a) HMS17 (b) HMT17 (c) VMT17

Figure M.7: Results for experiments HMS17, HMT17 and VMT17

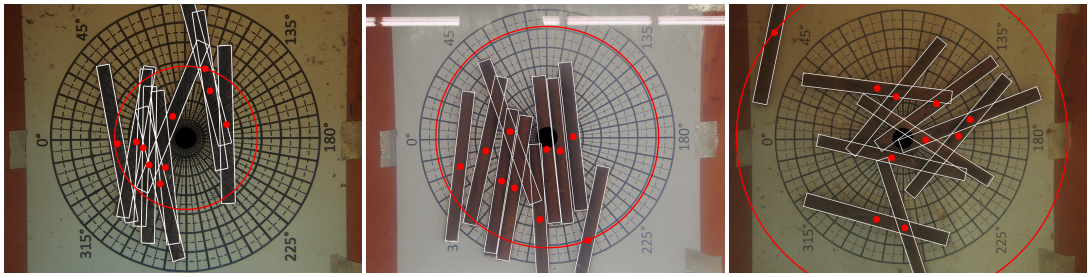

(a) HMS18 (b) HMT18 (c) VMT18

Figure M.8: Results for experiments HMS18, HMT18 and VMT18

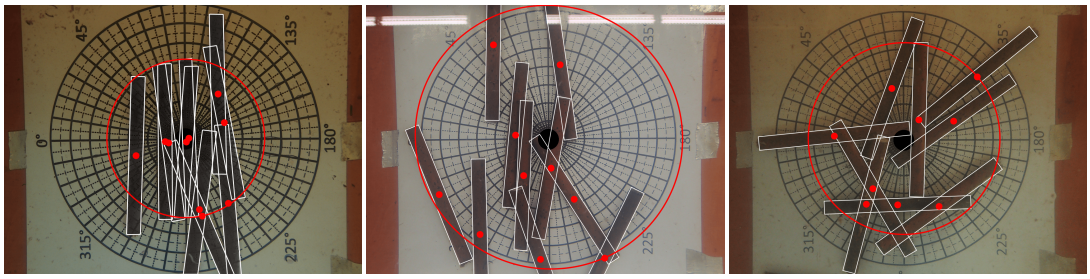

(a) HMS19 (b) HMT19 (c) VMT19

Figure M.9: Results for experiments HMS19, HMT19 and VMT19

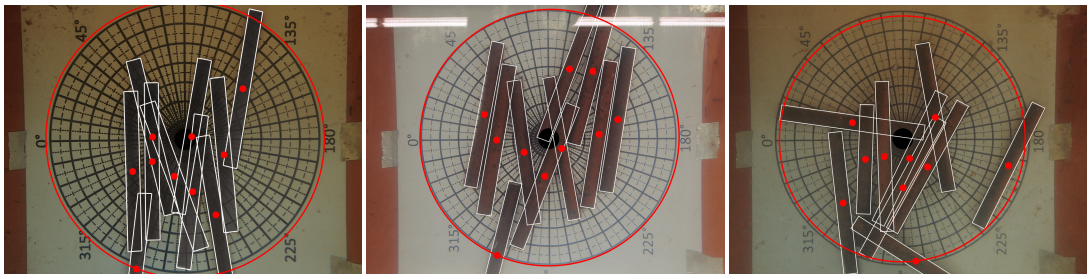

(a) HMS20 (b) HMT20 (c) VMT20

Figure M.10: Results for experiments HMS20, HMT20 and VMT20

N

Hatch mechanism figures

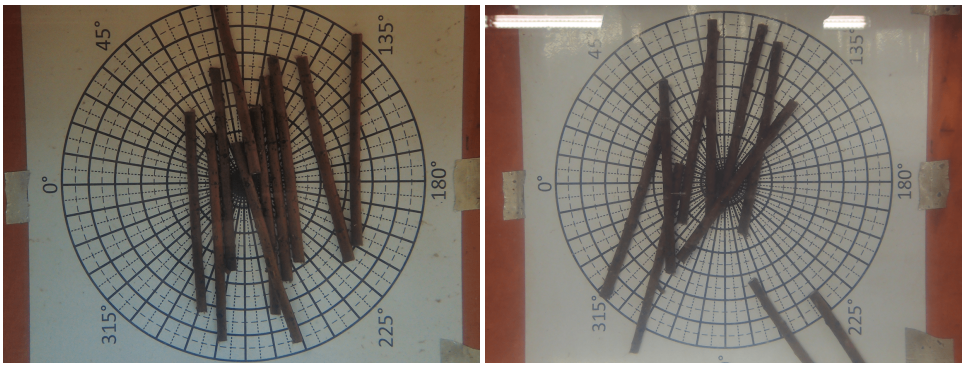

(a) HMT (b) HHB

Figure N.1: Results for experiments HMT10 and HHB10

(a) HMT (b) HHB

Figure N.2: Results for experiments HMT11 and HHB11

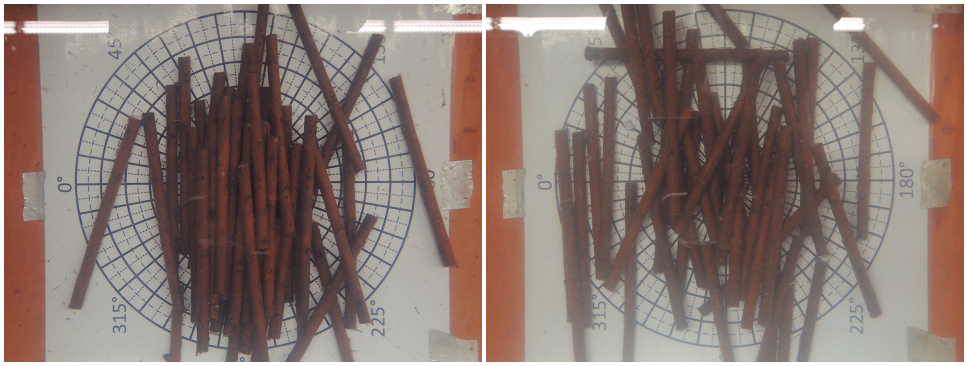

(a) HMT (b) HHB

Figure N.3: Results for experiments HMT12 and HHB12

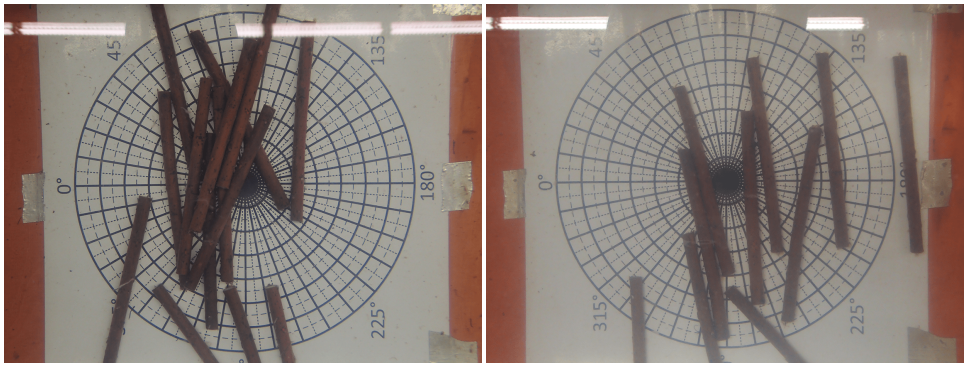

(a) HMT (b) HHB

Figure N.4: Results for experiments HMT13 and HHB13

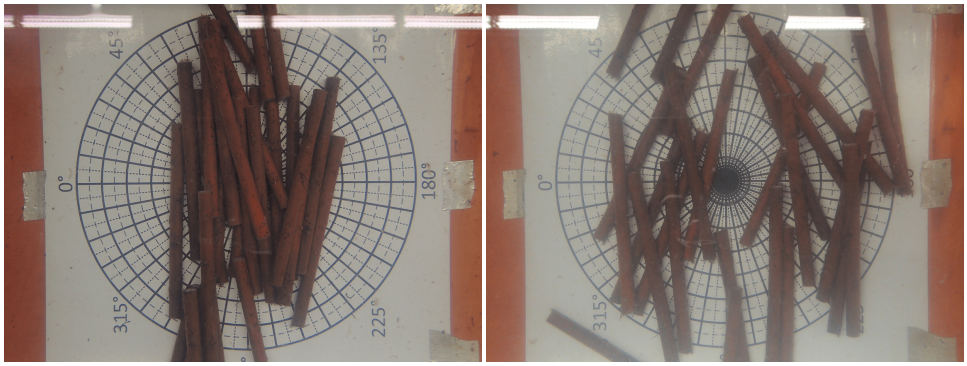

(a) HMT (b) HHB

Figure N.5: Results for experiments HMT14 and HHB14

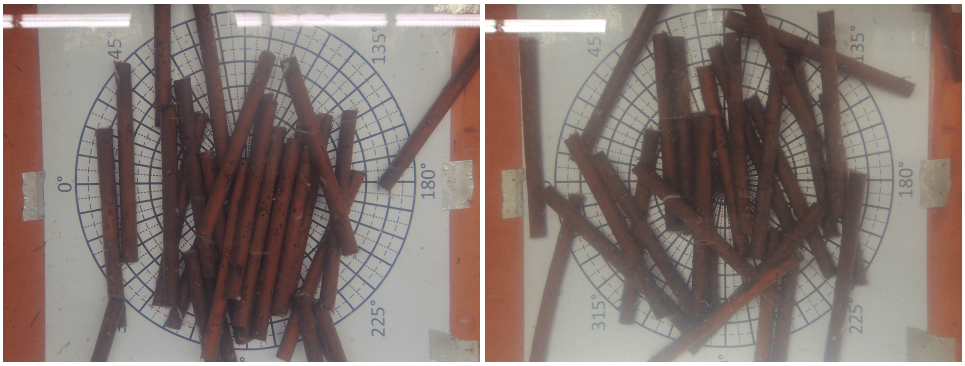

(a) HMT (b) HHB

Figure N.6: Results for experiments HMT15 and HHB15

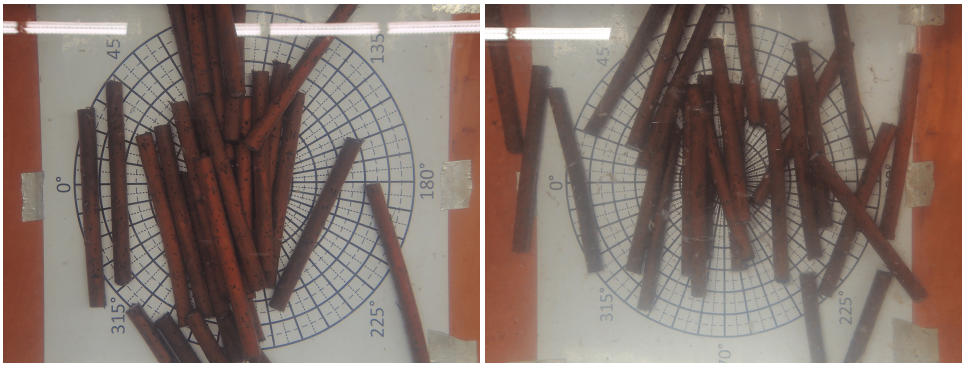

(a) HMT (b) HHB

Figure N.7: Results for experiments HMT17 and HHB17

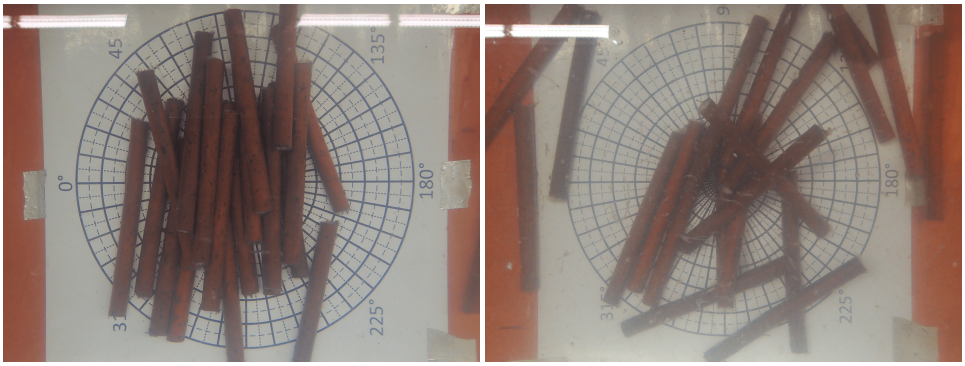

(a) HMT (b) HHB

Figure N.8: Results for experiments HMT18 and HHB18

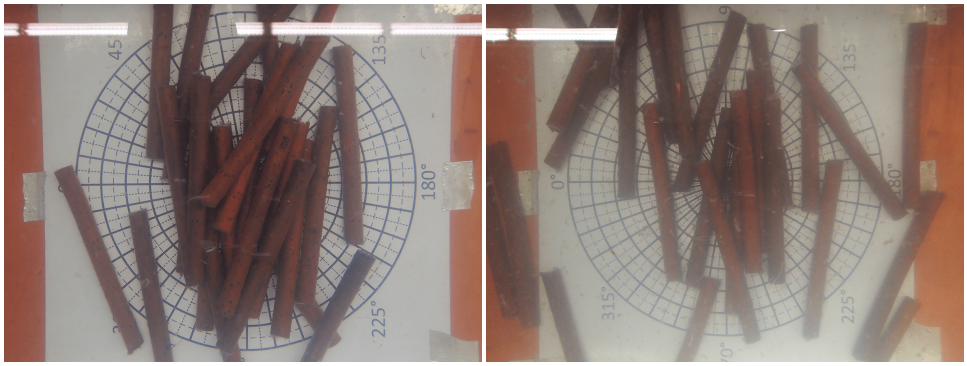

(a) HMT (b) HHB

Figure N.9: Results for experiments HMT19 and HHB19

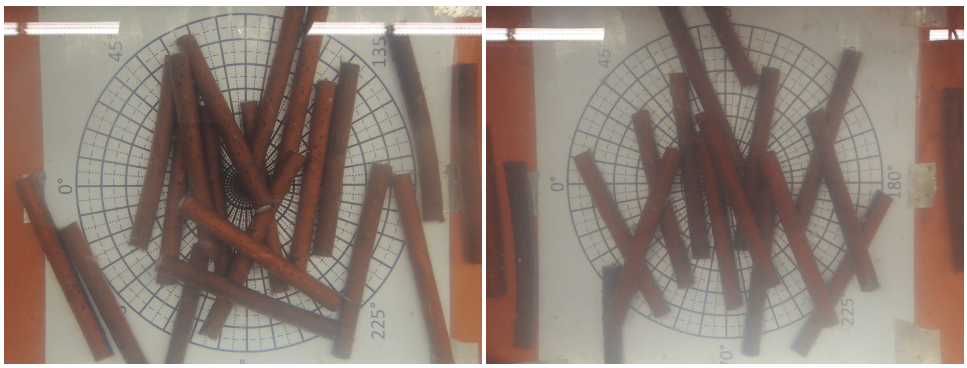

(a) HMT (b) HHB

Figure N.10: Results for experiments HMT20 and HHB20

O

Funnel mechanism figures

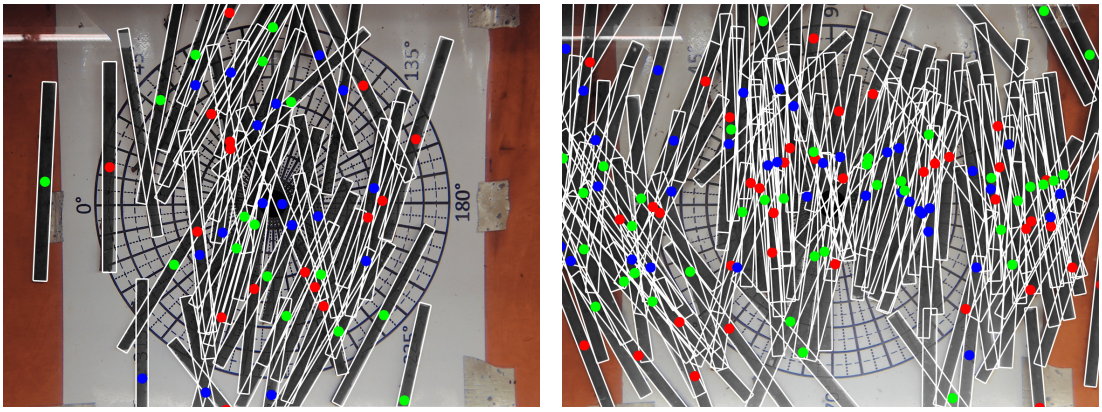

(a) HFB10

(b) HFB11

Figure O.1

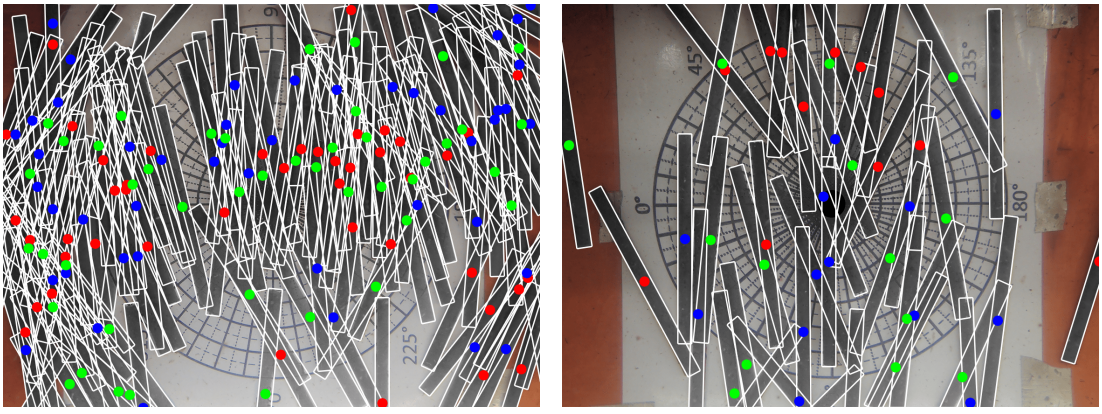

(a) HFB12

(b) HFB13

Figure O.2

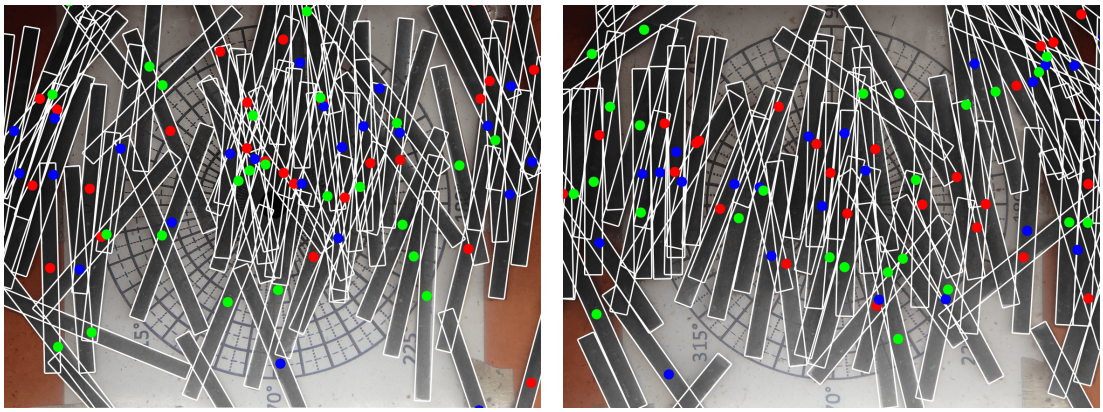

(a) HFB14 (b) HFB15

Figure O.3

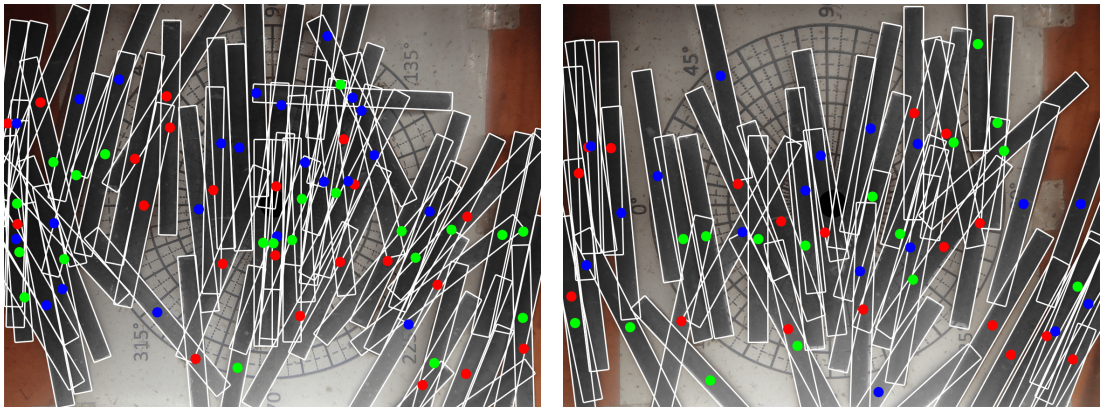

(a) HFB17 (b) HFB18

Figure O.4

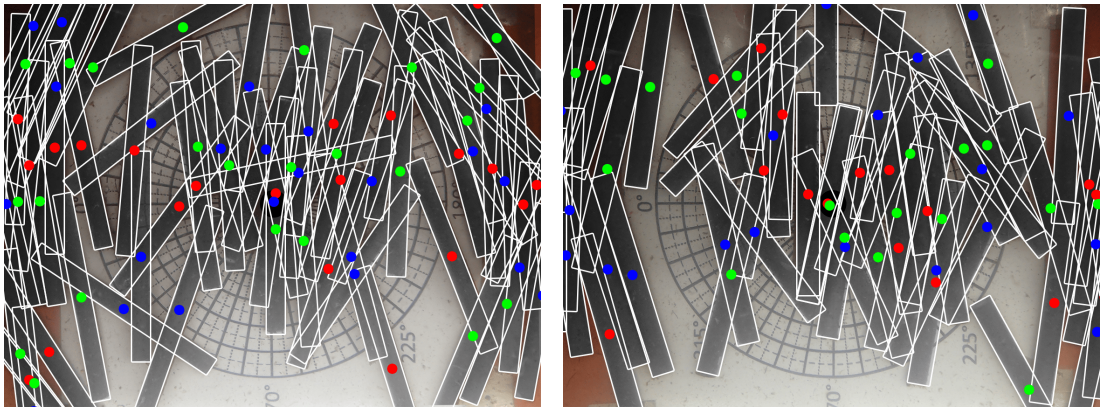

(a) HFB19 (b) HFB20

Figure O.5

P

Funnel mechanism confidence interval

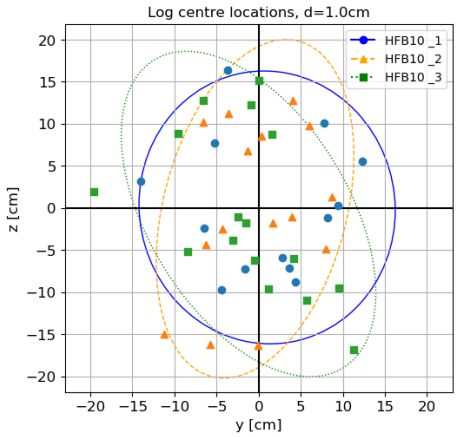

(a) 95% confidence interval ellipses for experiment HFB10

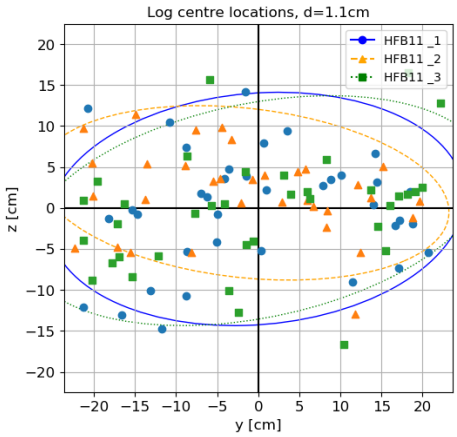

(b) 95% confidence interval ellipses for experiment HFB11

Figure P.1

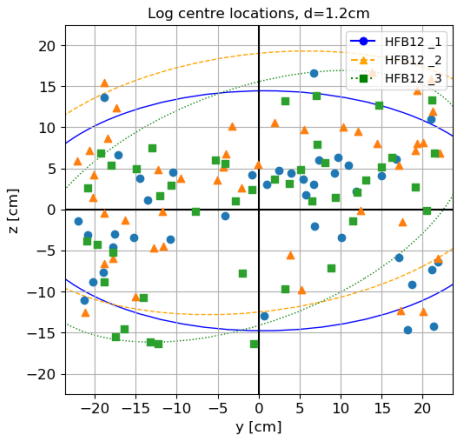

(a) 95% confidence interval ellipses for experiment HFB12

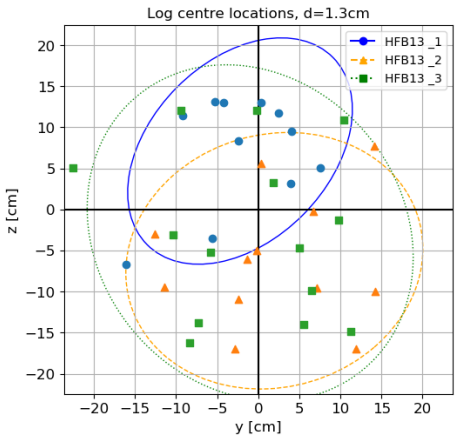

(b) 95% confidence interval ellipses for experiment HFB13

Figure P.2

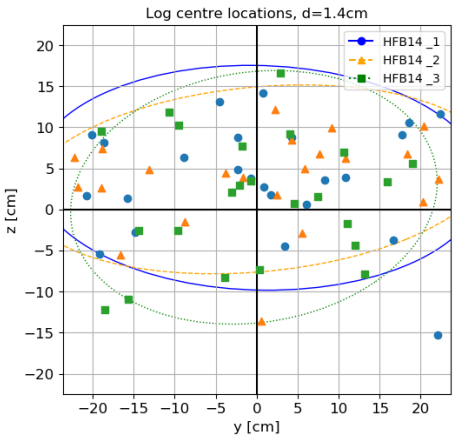

(a) 95% confidence interval ellipses for experiment HFB14

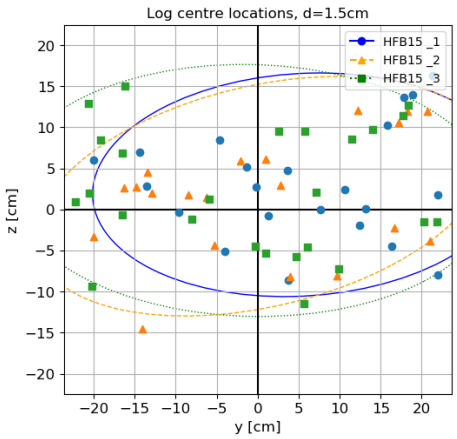

(b) 95% confidence interval ellipses for experiment HFB15

Figure P.3

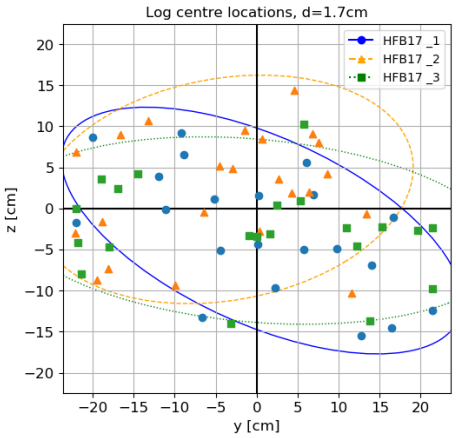

(a) 95% confidence interval ellipses for experiment HFB17

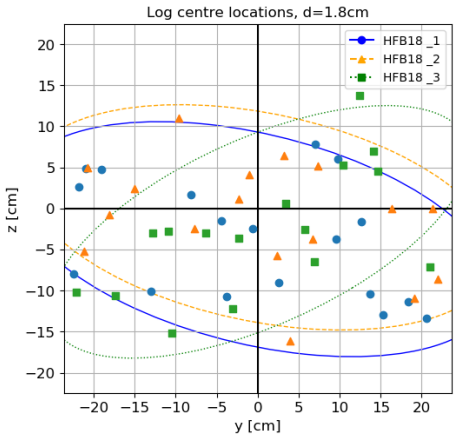

(b) 95% confidence interval ellipses for experiment HFB18

Figure P.4

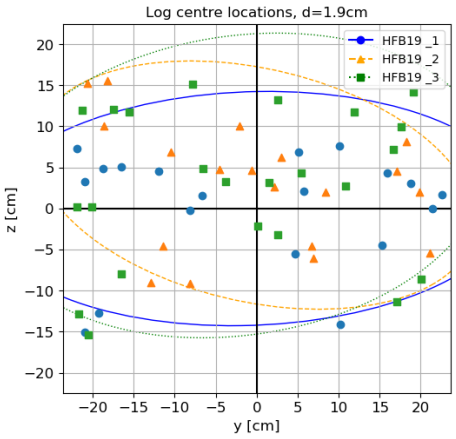

(a) 95% confidence interval ellipses for experiment HFB19

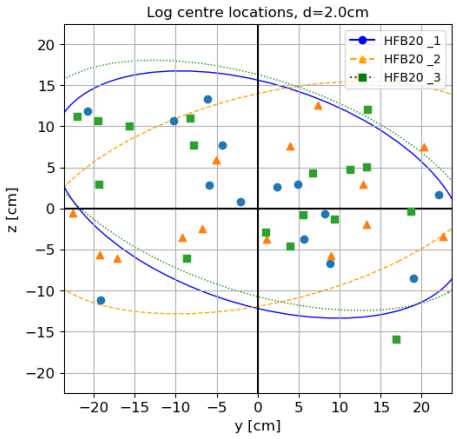

(b) 95% confidence interval ellipses for experiment HFB20

Figure P.5

Q

2D scans of the filter profiles

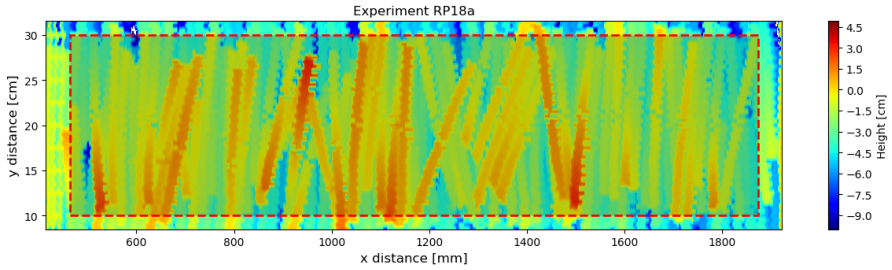

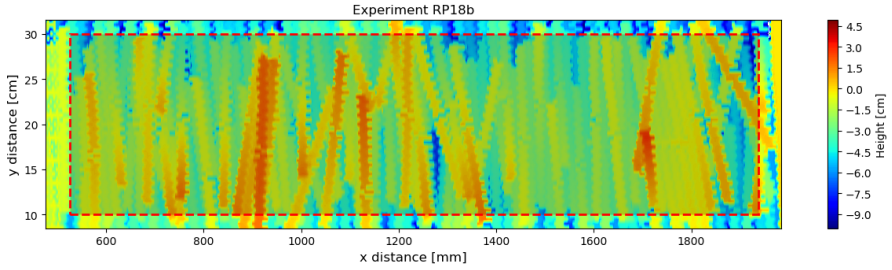

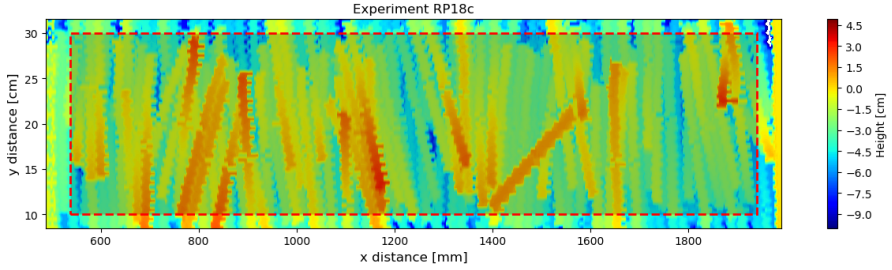

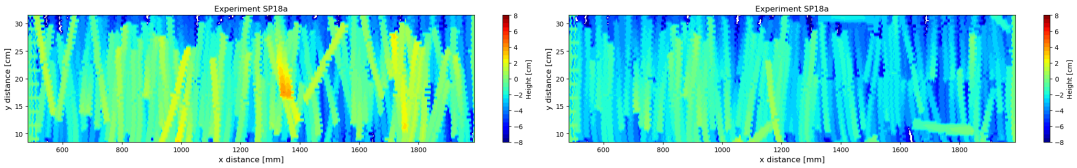

(a) Before the experiment (b) After the experiment

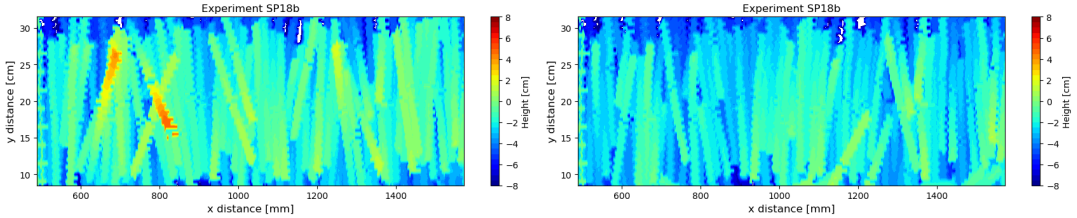

(a) Before the experiment (b) After the experiment

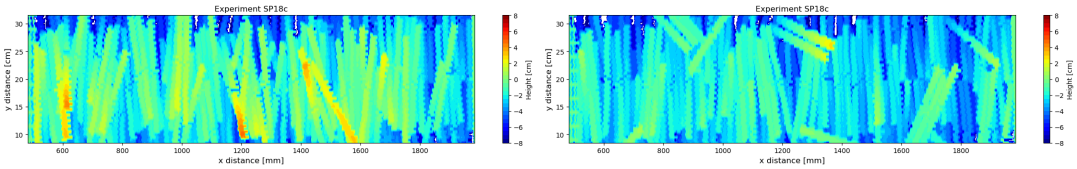

(a) Before the experiment (b) After the experiment

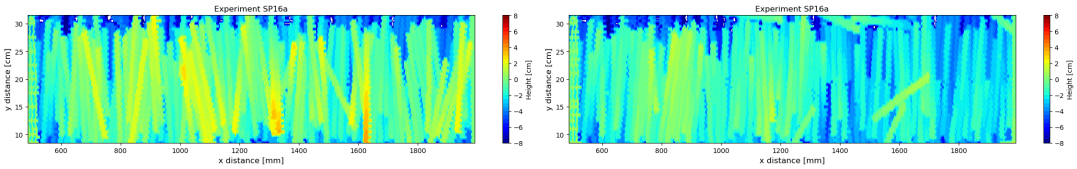

(a) Before the experiment (b) After the experiment

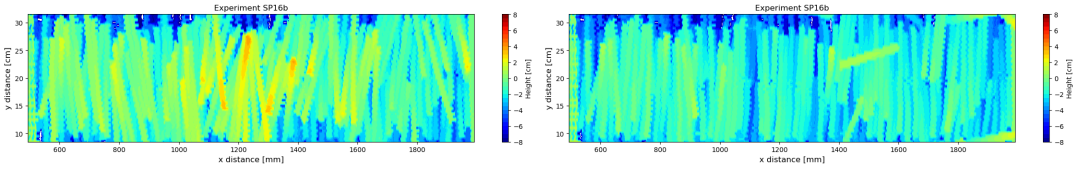

(a) Before the experiment (b) After the experiment

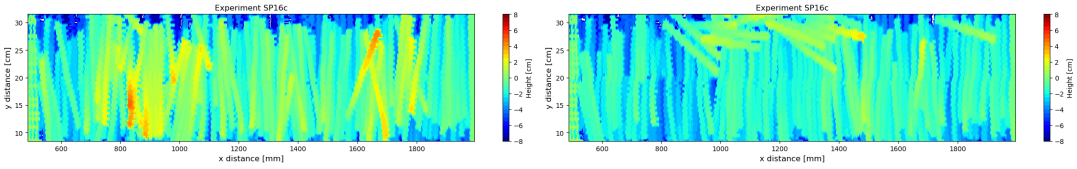

(a) Before the experiment (b) After the experiment

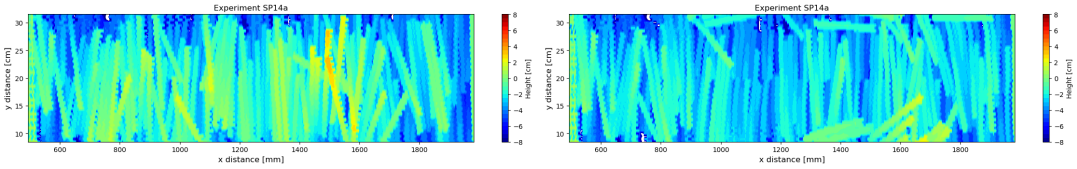

(a) Before the experiment (b) After the experiment

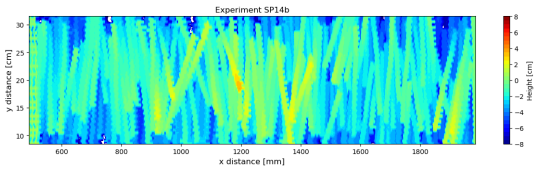

(a) Before the experiment

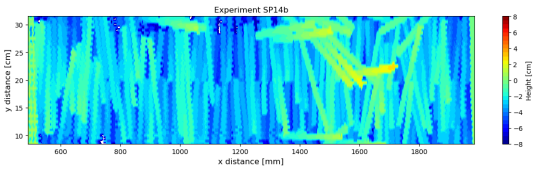

(b) After the experiment

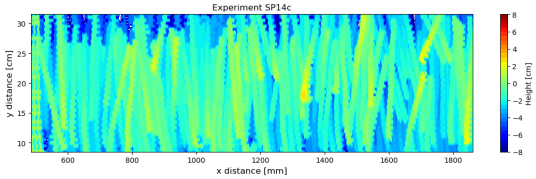

(a) Before the experiment

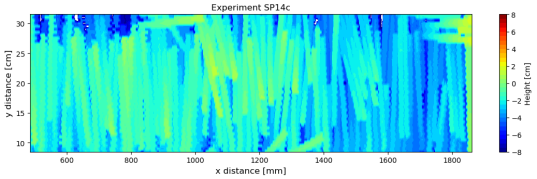

(b) After the experiment

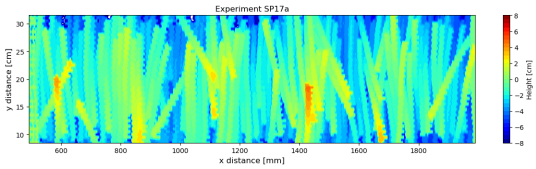

(a) Before the experiment

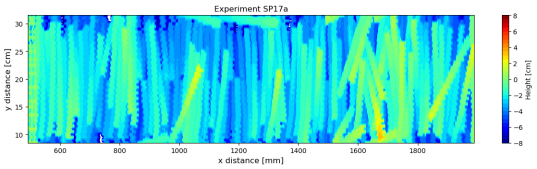

(b) After the experiment

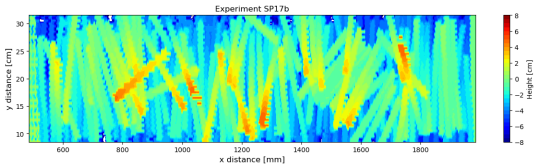

(a) Before the experiment

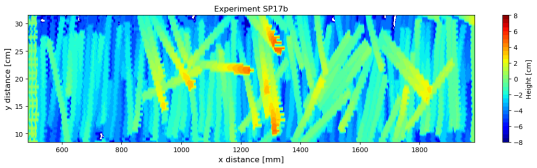

(b) After the experiment

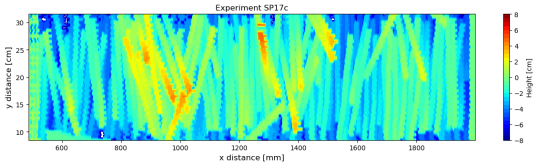

(a) Before the experiment

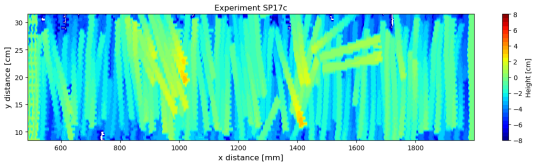

(b) After the experiment

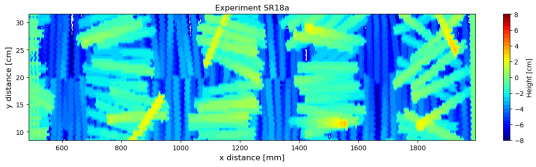

(a) Before the experiment

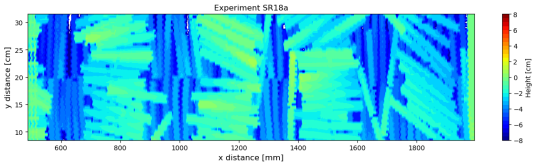

(b) After the experiment

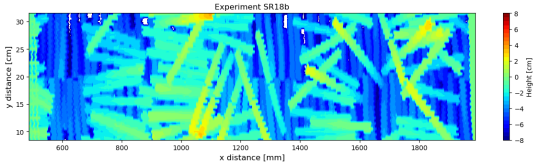

(a) Before the experiment

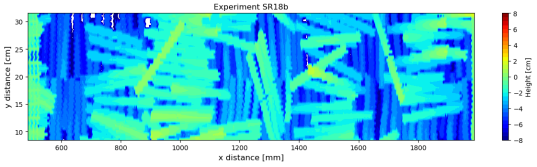

(b) After the experiment

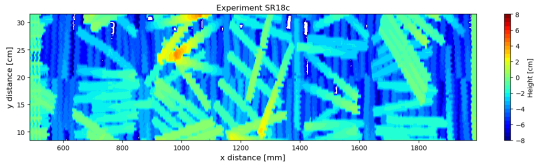

(a) Before the experiment

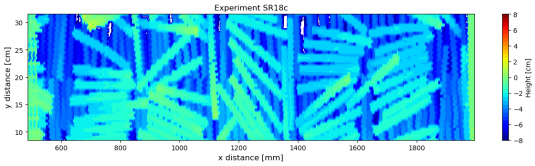

(b) After the experiment

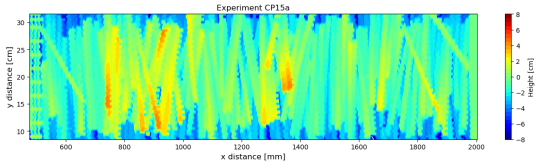

(a) Before the experiment

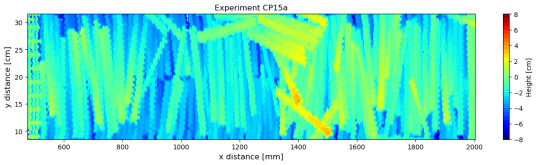

(b) After the experiment

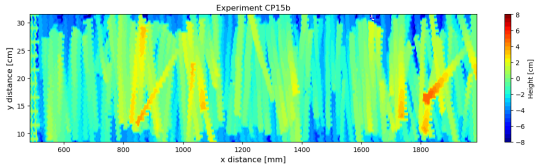

(a) Before the experiment

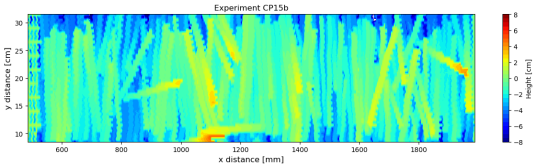

(b) After the experiment

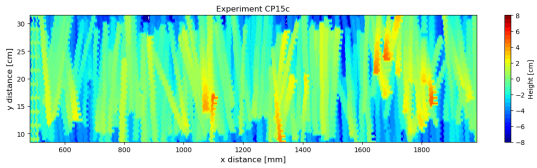

(a) Before the experiment

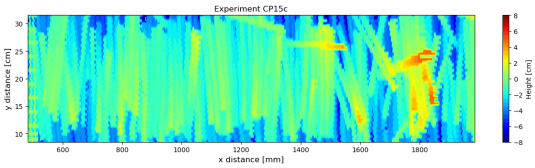

(b) After the experiment

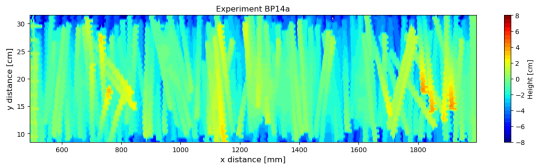

(a) Before the experiment

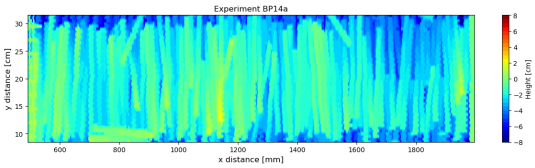

(b) After the experiment

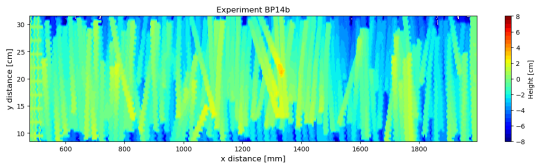

(a) Before the experiment

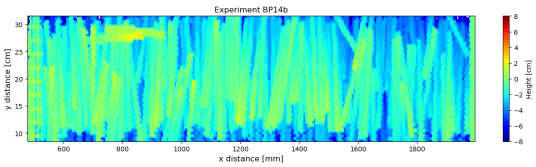

(b) After the experiment

R

Zero velocity level statistics

Statistics for equation 6.1 (reference)

d [cm]	1.4	1.5	1.6	1.7	1.8
Mean z_0 [mm]	2.64	3.36	8.46	9.65	5.71
σ z_0 [mm]	0.29	0.67	0.12	2.85	2.72

Table R.1: Mean and standard deviation of z_0 for d

σ_{filter} [cm]	4.32	4.91	5.43	5.67	5.90	5.95	7.46
Mean $z0$ [mm]	9.65	2.64	3.36	7.68	6.34	0.31	8.46
σ_d z_0 [mm]	0.28	0.03	0.07	0.25	0.12	0.18	0.01

Table R.2: Mean and standard deviation of z_0 for σ_{filter}

Statistics for equation 6.2 (modified)

d [cm]	1.4	1.5	1.6	1.7	1.8
Mean z_0 [mm]	7.12	5.66	12.14	17.59	13.87
σ z_0 [mm]	0.60	0.99	0.17	4.21	5.73

Table R.3: Mean and standard deviation of z_0 for d

σ_{filter} [cm]	4.32	4.91	5.43	5.67	5.90	5.95	7.46
Mean $z0$ [mm]	17.59	7.12	5.66	18.16	15.64	7.80	12.14
σ_d z_0 [mm]	0.42	0.06	0.10	0.45	0.23	0.38	0.02

Table R.4: Mean and standard deviation of z_0 for σ_{filter}

S

Shields parameter of all flume experiments

Experiment	Shear velocity u_* [m/s]			
	1. Initial motion	2. Deformation	3. Transport	4. Failure
SP18a	0.064	0.078	0.090	0.118
SP18b	0.058		0.092	
SP18c	0.052	0.071		0.114
Avg.	0.058	0.075	0.091	0.116
SP16a	0.041	0.067	0.078	0.088
SP16b	0.051	0.057		0.102
SP16c	0.054	0.069	0.088	0.099
Avg.	0.049	0.064	0.083	0.096
SP14a	0.032	0.059	0.077	0.089
SP14b		0.058	0.072	0.100
SP14c	0.042	0.055		0.079
Avg.	0.037	0.057	0.075	0.089
SP17a	0.018	0.021	0.028	0.033
SP17b	0.014	0.018		
SP17c		0.019	0.023	0.029
Avg.	0.016	0.019	0.026	0.031
SR18a	0.051	0.081	0.118	
SR18b	0.063	0.067		
SR18c		0.078	0.103	
Avg.	0.057	0.076	0.111	
CP15a	0.038	0.060		0.095
CP15b		0.056	0.079	
CP15c	0.050	0.059		0.087
Avg.	0.044	0.059	0.079	0.091
BA14a	0.039		0.069	0.086
BA14b	0.039		0.077	
Avg.	0.039		0.069	0.081

Table S.1: Critical shear velocities for each phase for all experiments